Gene Therapy

- Gene therapy is a technique for correcting defective genes responsible for disease development. Researchers may use one of several approaches for correcting faulty genes:
  - **A normal gene may be inserted into a nonspecific location within the genome to replace a nonfunctional gene. This approach is most common.**
  - **An abnormal gene could be swapped for a normal gene through homologous recombination.**
  - **The abnormal gene could be repaired through selective reverse mutation, which returns the gene to its normal function.**
  - **The regulation (the degree to which a gene is turned on or off) of a particular gene could be altered.**

How Gene Therapy Works?

- In most gene therapy studies, a "normal" gene is inserted into the genome to replace an "abnormal," disease-causing gene. A carrier molecule called a vector must be used to deliver the therapeutic gene to the patient's target cells. Currently, the most common vector is a virus that has been genetically altered to carry normal human DNA. Viruses have evolved a way of encapsulating and delivering their genes to human cells in a pathogenic manner. Scientists have tried to take advantage of this capability and manipulate the virus genome to remove disease-causing genes and insert therapeutic genes.
- Target cells such as the patient's liver or lung cells are infected with the viral vector. The vector then unloads its genetic material containing the therapeutic human gene into the target cell. The generation of a functional protein product from the therapeutic gene restores the target cell to a normal state.

Gene Delivery

- Transfection- the delivery of foreign molecules such as DNA and RNA into eukaryotic cells
- Naked DNA is not suitable for in-vivo transport of genetic materials-> degradation by serum nucleases
- Ideal gene delivery system
  - Biocompatible
  - Non-immunogenic
  - Stable in blood stream
  - Protect DNA during transport
  - Small enough to extravagate
  - Cell and tissue specific

Endocytosis

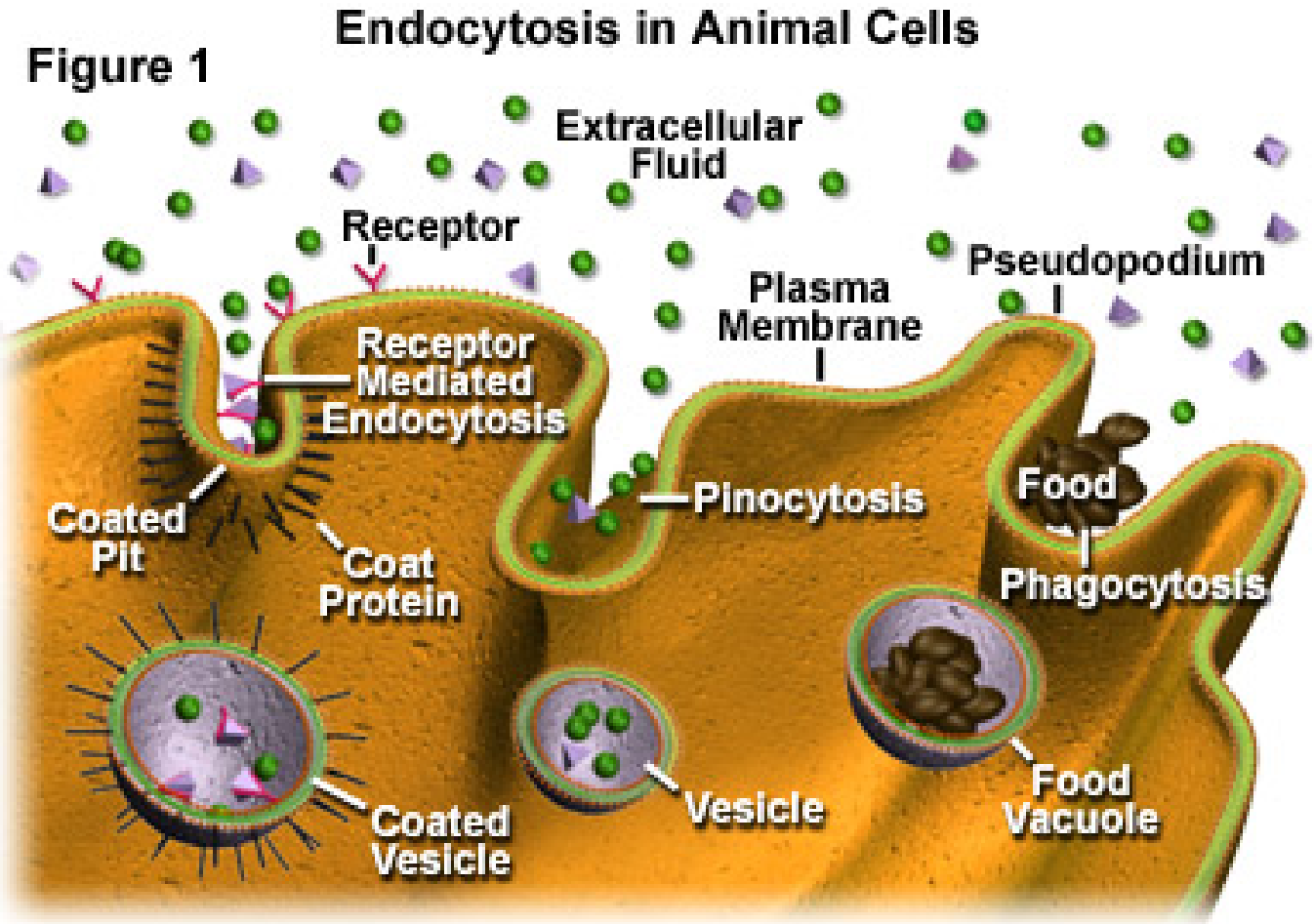

Endocytosis

- Phagocytosis is the process by which cells ingest large objects, such as cells which have undergone apoptosis, bacteria, or viruses. The membrane folds around the object, and the object is sealed off into a large vacuole known as a phagosome.
- Pinocytosis is a synonym for endocytosis. This process is concerned with the uptake of solutes and single molecules such as proteins.
- Receptor-mediated endocytosis is a more specific active event where the cytoplasm membrane folds inward to form coated pits. These inward budding vesicles bud to form cytoplasmic vesicles.

http://highered.mcgraw-hill.com/olc/dl/120068/bio02.swf

Endocytosis pathways

- Macropinocytosis is the invagination of the cell membrane to form a pocket which then pinches off into the cell to form a vesicle filled with extracellular fluid (and molecules within it). The filling of the pocket occurs in a non-specific manner. The vesicle then travels into the cytosol and fuses with other vesicles such as endosomes and lysosomes.
- Clathrin-mediated endocytosis is the specific uptake of large extracellular molecules such as proteins, membrane localized receptors and ion-channels. These receptors are associated with the cytosolic protein clathrin which initiates the formation of a vesicle by forming a crystalline coat on the inner surface of the cell's membrane.
- Caveolae consist of the protein caveolin-1 with a bilayer enriched in cholesterol and glycosphingolipids. Caveolae are flask shaped pits in the membrane that resemble the shape of a cave (hence the name caveolae). Uptake of extracellular molecules are also believed to be specifically mediated via receptors in caveolae.

Endocytic pathway in mammalian cells

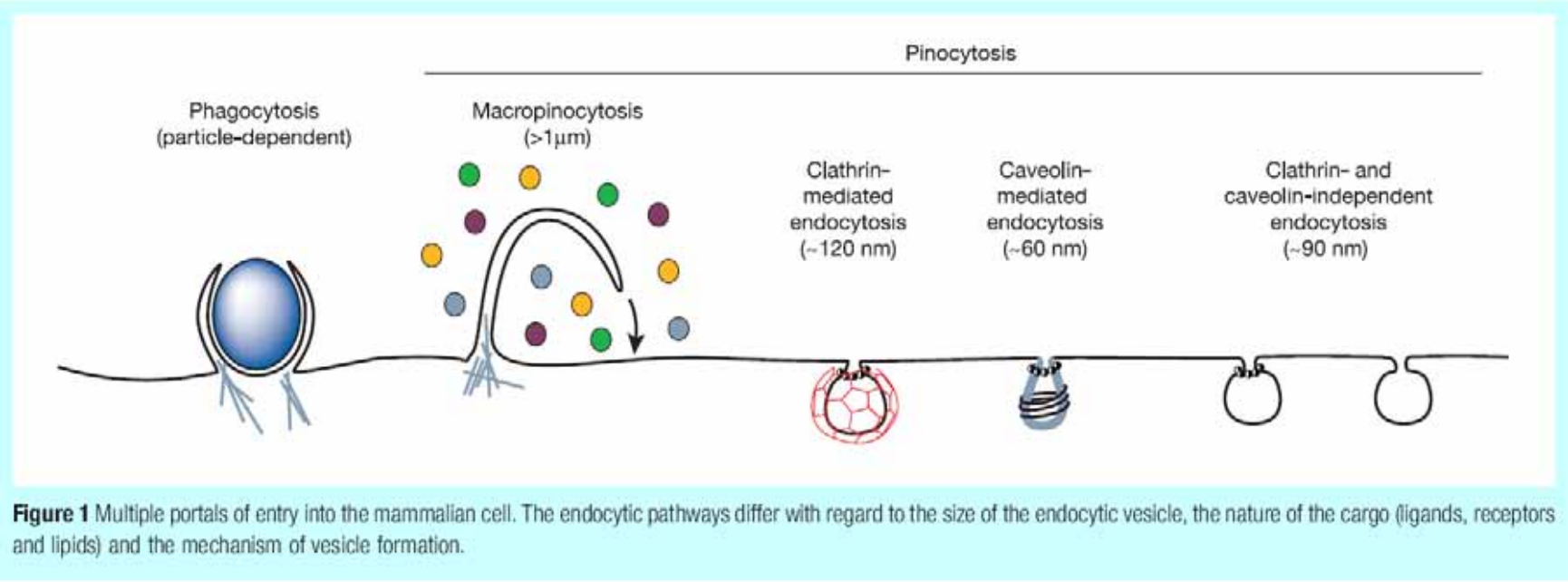

Figure 1 Multiple portals of entry into the mammalian cell. The endocytic pathways differ with regard to the size of the endocytic vesicle, the nature of the cargo (ligands, receptors and lipids) and the mechanism of vesicle formation.

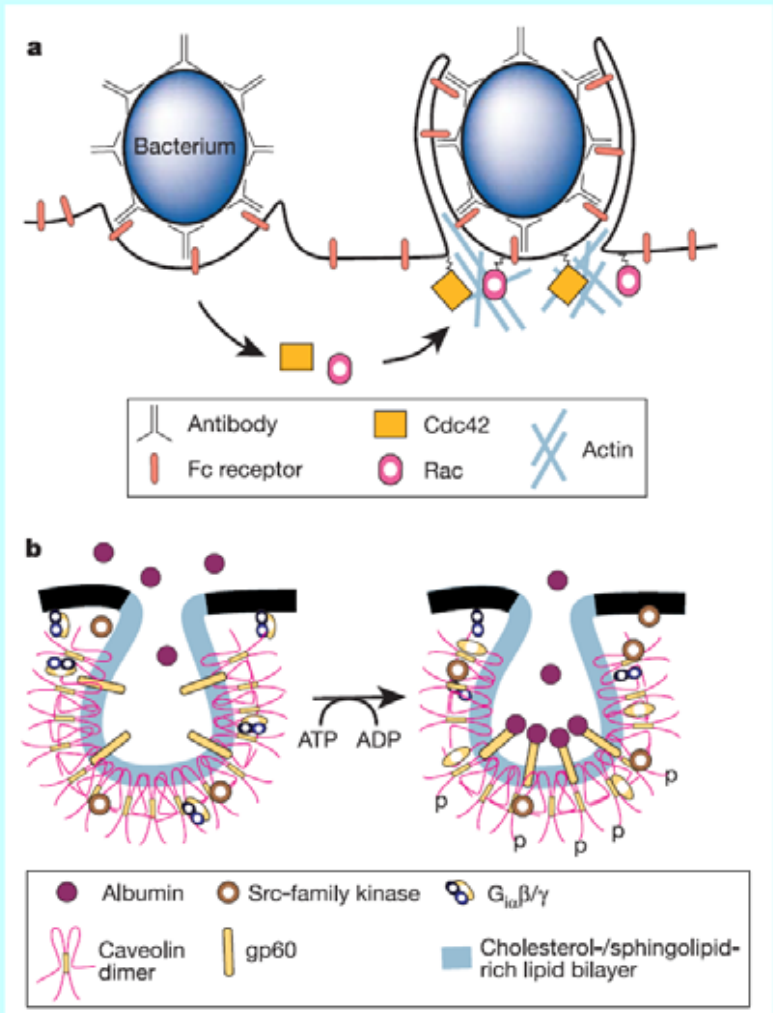

Figure 2 Cargo-stimulated signalling pathways induce uptake by phagocytosis and caveolae. **a**, Fc receptors on the surface of macrophages are activated by immunoglobulin-γ molecules bound to a bacterium. A signalling cascade that involves Rac, Cdc42 and downstream kinases triggers actin rearrangements, protrusion of the membrane around the bacterium, and its engulfment into a phagosome. **b**, Albumin binds to and presumably clusters its receptor, gp60, in caveolae to activate $G_{i\alpha}$ and Src kinases, triggering caveolae endocytosis.

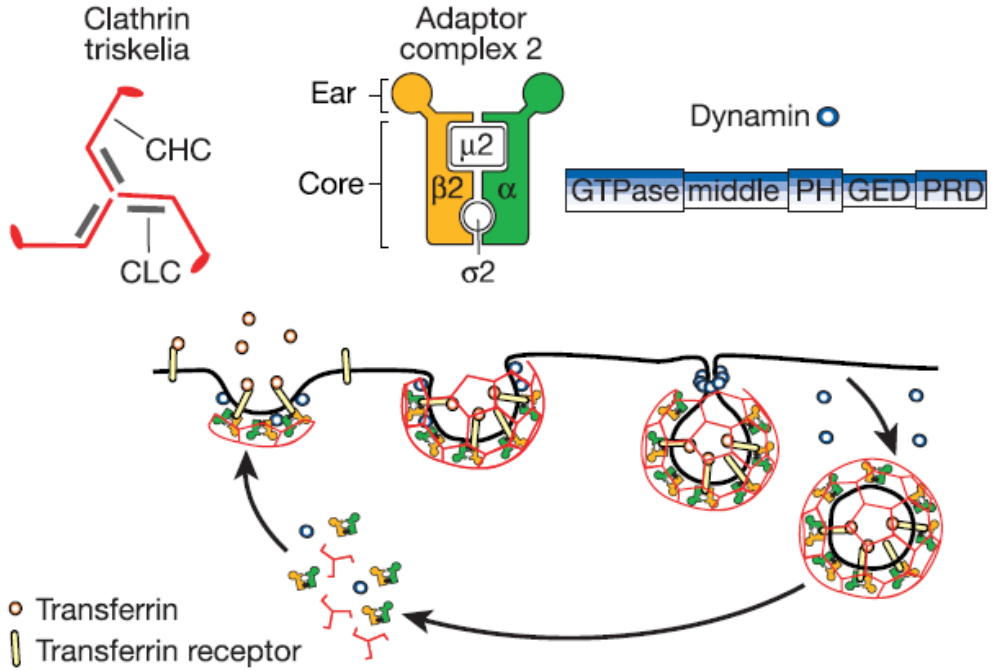

Figure 3 Core components of the machinery driving clathrin-mediated endocytosis. Clathrin triskelions, composed of three clathrin heavy chains (CHC) and three tightly associated light chains (CLC), assemble into a polygonal lattice, which helps to deform the overlying plasma membrane into a coated pit. Heterotetrameric AP2 complexes are targeted to the plasma membrane by the α-adaptin subunits, where they mediate clathrin assembly through the β2-subunit, and interact directly with sorting motifs on cargo molecules through their μ2 subunits. Dynamin is a multidomain GTPase that is recruited to the necks of coated pits, where it can assemble into a spiral or 'collar' to mediate or monitor membrane fission and the release of CCVs (see text for details). A subsequent uncoating reaction recycles the coat constituents for reuse.

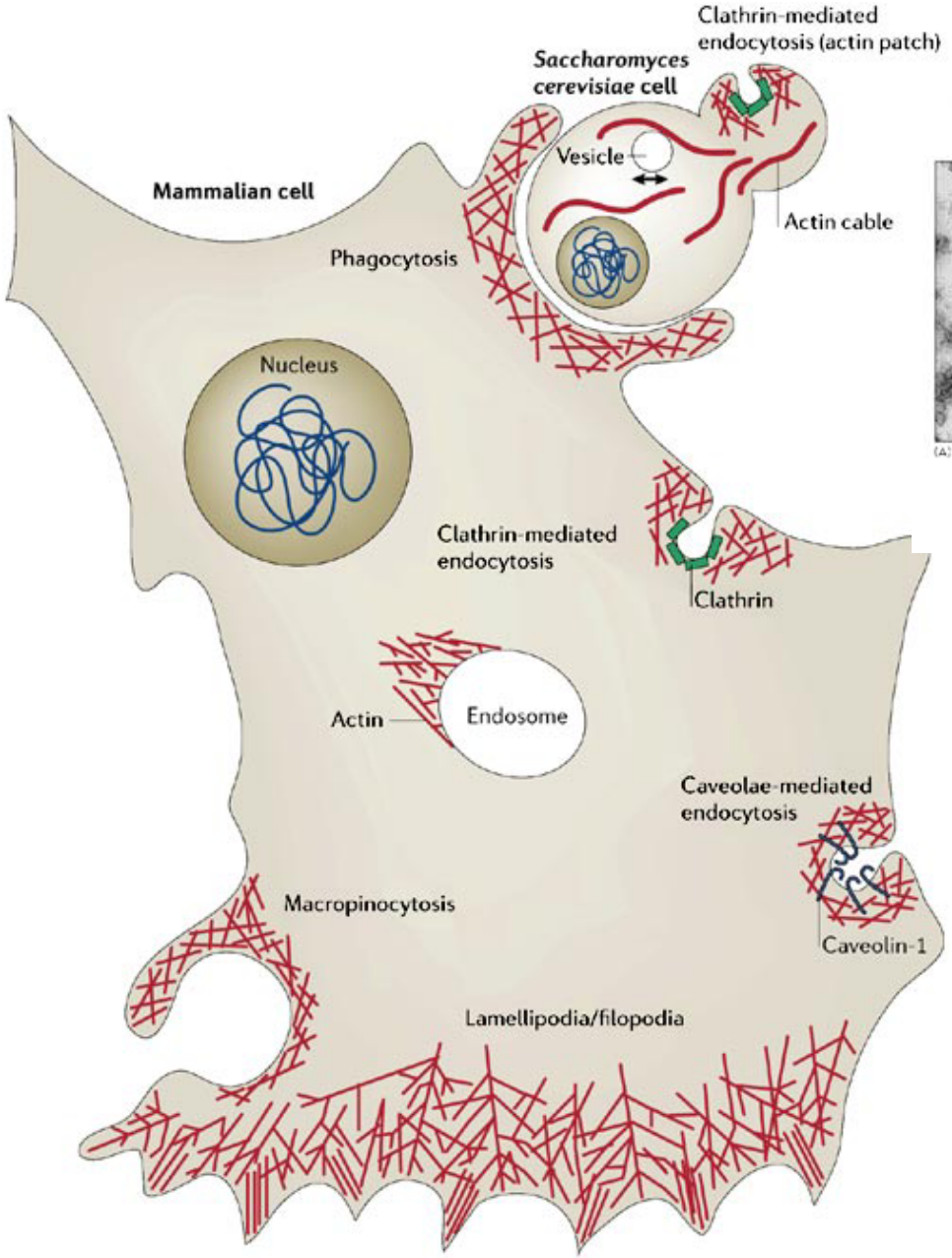

Formation of Clathrin-Coated Vesicles

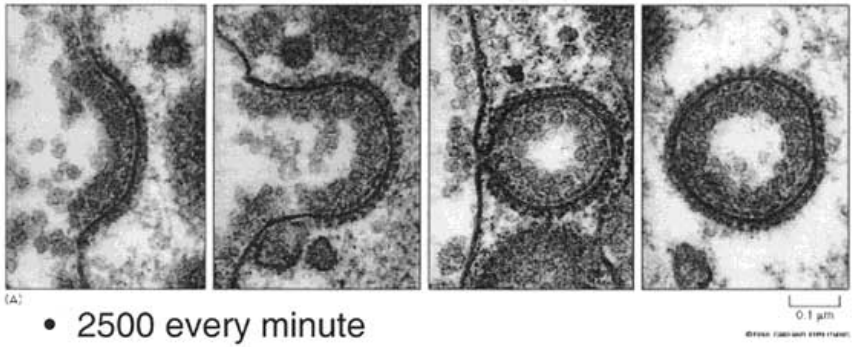

- 2500 every minute
- CCV uncoat within seconds

Clathrin-mediated endocytosis

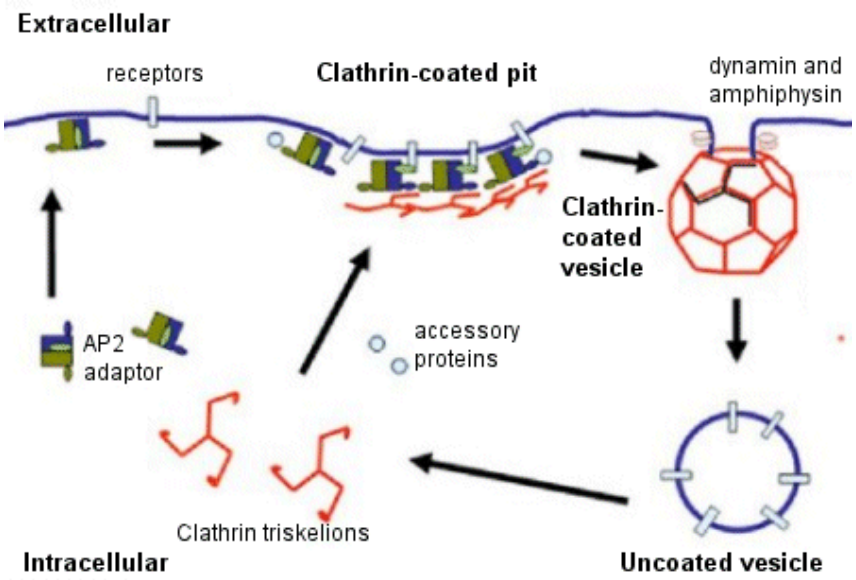

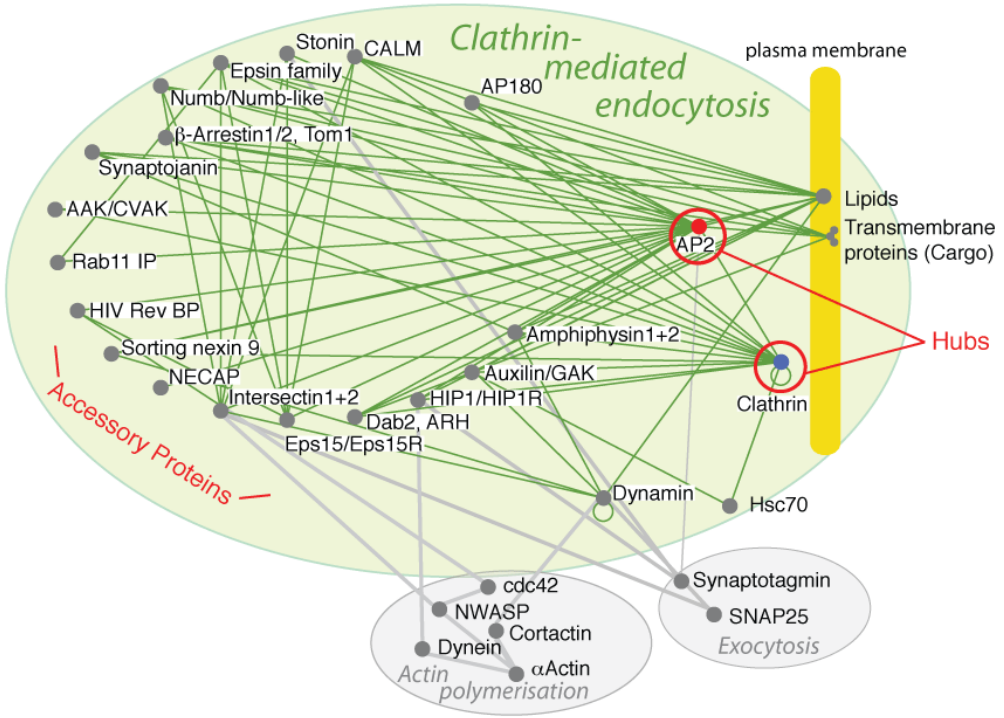

A

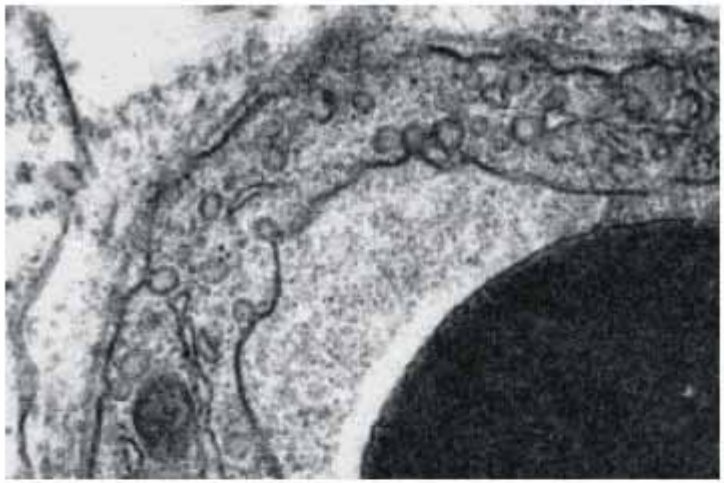

B

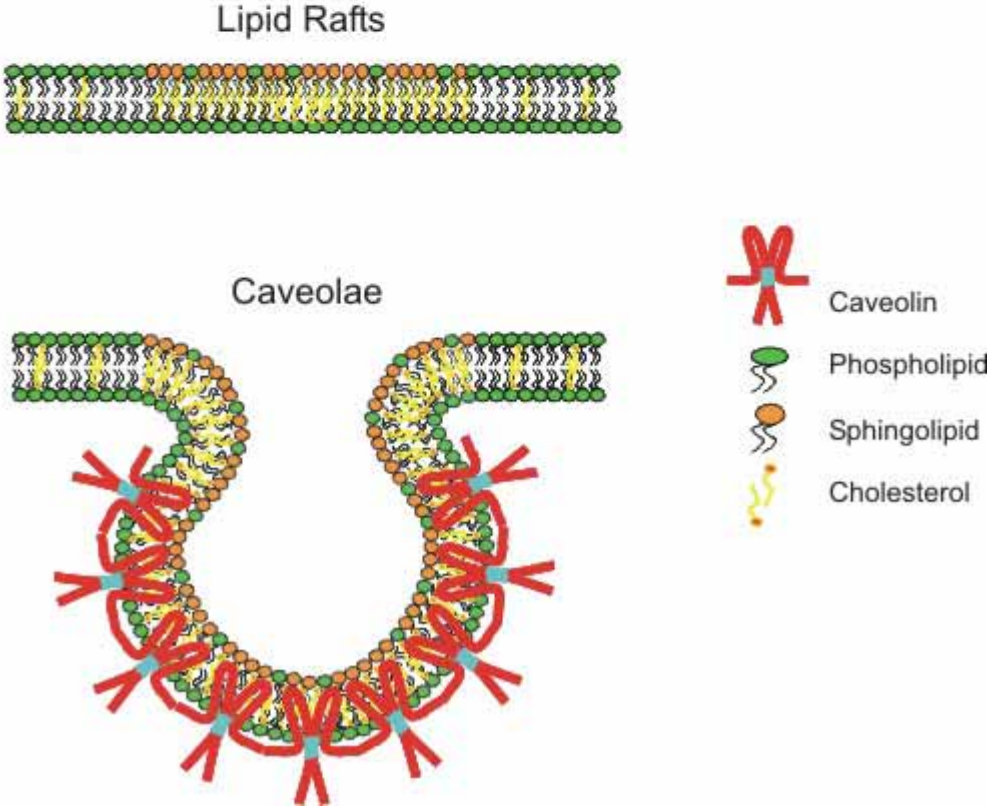
Lipid Rafts
Caveolae
Caveolin
Phospholipid
Sphingolipid
Cholesterol

Barrier to non-viral gene delivery

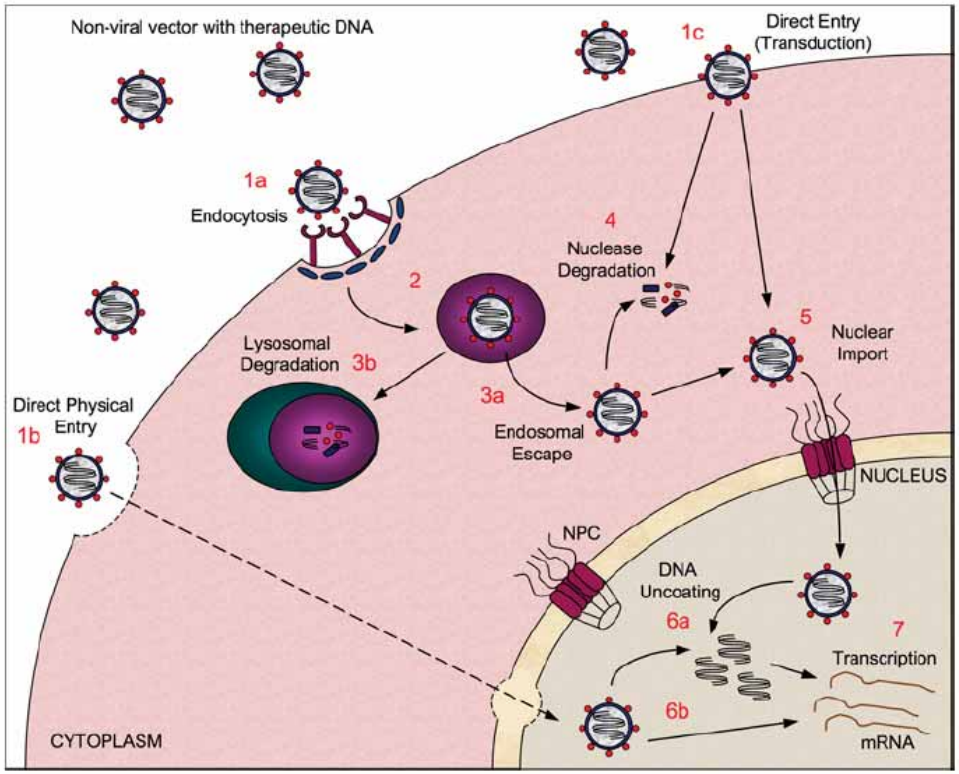

Figure 1 Barriers to non-viral gene delivery

Representation of the route travelled by a non-viral gene-delivery vector carrying therapeutic DNA to the nucleus. A non-viral vector, formed by interaction of the DNA with a carrier compound, must cross the plasma membrane to enter the cell. This can be via several routes, including endocytosis-based entry (1a), direct physical entry routes, such as electroporation or ballistic delivery (1b), or direct entry via protein transduction (1c). Depending on the mode of cellular entry, the vector may become encapsulated in an endosome (2), from which it must escape (3a) or it will become degraded when the endosome fuses with a lysosome (3b). The DNA will at some point be subjected to degradation by cytosolic nucleases (4), as it traverses through the cytoplasm to reach the nucleus. Finally, the vector must undergo nuclear transport (5) through NPCs embedded in the NE in order to gain access to the nucleoplasm. Once in the nucleus, the DNA may (6a) or may not (6b) need to be uncoated, depending upon the vector used, before it can ultimately be transcribed (7).

Biochem. J. (2007) **406**, 185–202 (Printed in Great Britain) doi:10.1042/BJ20070505

NLS-mediated nuclear import

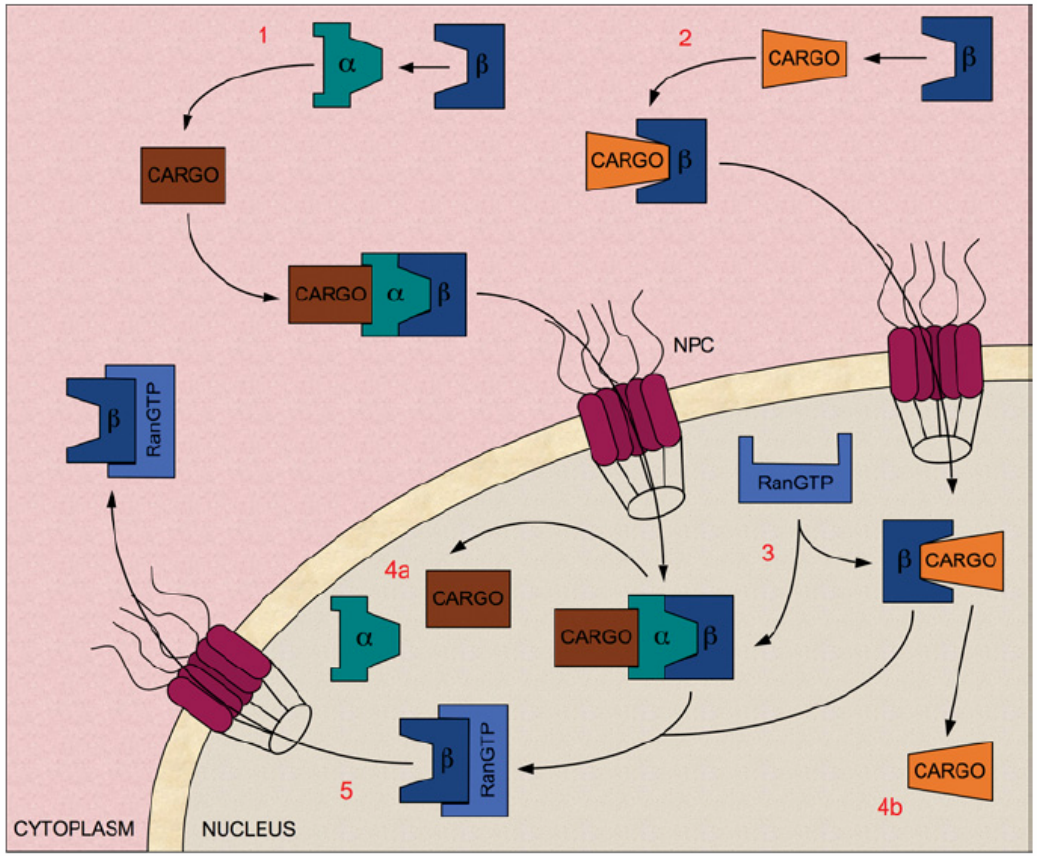

Figure 2 NLS-mediated nuclear import pathways

In classical nuclear import, the NLS found in cargo bound for the nucleus is recognized by the Imp α subunit of the Imp α/β heterodimer (1). However, there are also many examples where Imp β or one of its many homologues can mediate nuclear import or cargo proteins independently of Imp α (2). In both cases, transient interactions between the Imp β and the nucleoporin proteins that line the NE-embedded NPCs mediate translocation into the nucleus. Once inside, RanGTP binds to Imp β (3), releasing Imp α and the cargo into the nucleoplasm (4a and 4b). RanGTP itself is then recycled back to the cytoplasm (5), where it is converted into its RanGDP state (not shown). An animated version of this Figure can be found at http://www.BiochemJ.org/bj/406/0185/bj4060185add.htm

Transfection

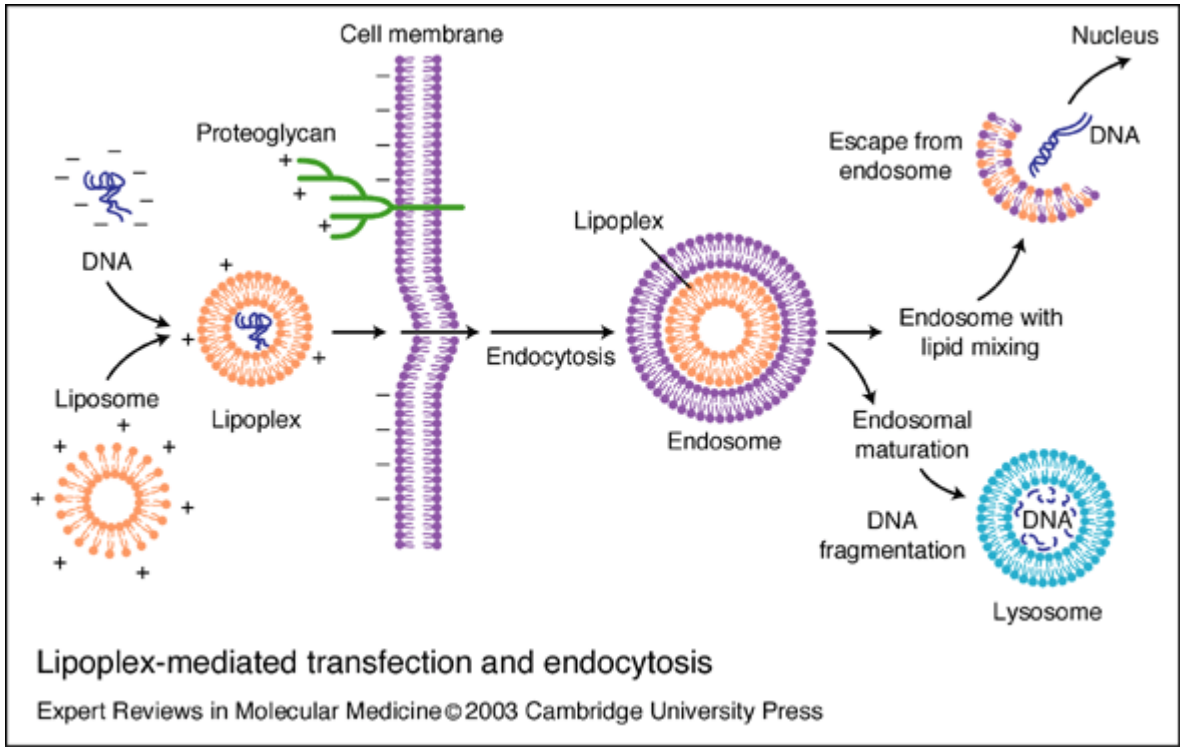

Lipoplex-mediated transfection and endocytosis

Transient and Stable Transfection

- Transient
  - No chromosome integration
  - Expression 24-96 Hr
  - Super-coiled plasmid
- Stable
  - Chromosome integration
  - Linear DNA
  - 1 in 10^4
  - Selection

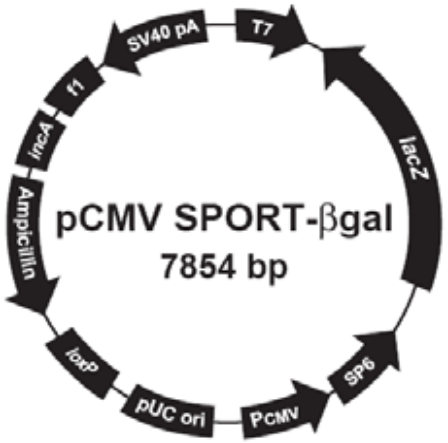

Challenges

- Cell targeting
- Transport through the cell membrane
- Uptake and degradation in endolysome
- Intracellular trafficking of plasmid to nucleus

Transfection Technology

- DEAE dextran
- Calcium phosphate
- Electroporation
- Microinjection
- Ballistic particle
- Nanoparticles
  - Cationic liposome
  - Cationic polyermer
  - Activated dendrimer
  - Gold nanoparticles
  - Chitosan

DEAE-dextran

- Diethylaminoethyl (DEAE)-dextran was introduced in 1965 (5) and is one of the oldest methods for introducing nucleic acids into cultured mammalian cells. The positively charged DEAE-dextran molecule interacts with the negatively charged phosphate backbone of the nucleic acid. The DNA–DEAEdextran complexes appear to adsorb onto the cell surface and be taken up by endocytosis. The advantages of this technique are its relative simplicity and reproducibility of results. Disadvantages include cytotoxic effects and the fact that the amount of serum in the culture medium must be temporarily reduced during the transfection procedure. In addition, the DEAE-dextran method is best suited for transient transfection only.

Dextran is a complex branched polysaccharide made of many glucose molecules joined into chains of varying lengths.

DEAE-Dextran Method*

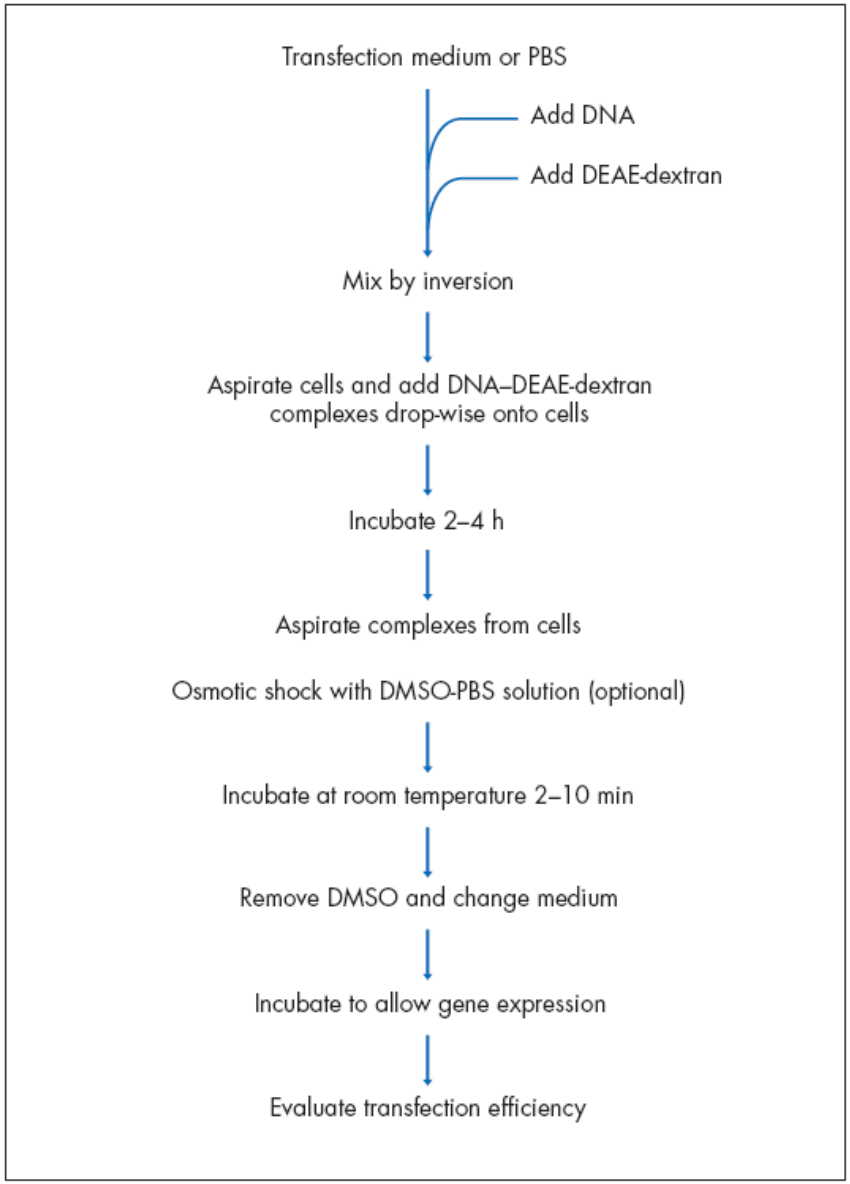

Calcium Phosphate

- The calcium-phosphate method was first used in 1973 to introduce adenovirus DNA into mammalian cells (6). The principle involves mixing DNA in a phosphate buffer with calcium chloride. The resulting calcium-phosphate–DNA complexes adhere to the cell membrane and enter the cytoplasm by endocytosis. Advantages of calcium-phosphate–based transfection are its easy handling and, compared with the DEAE-dextran method, its much higher suitability for stable transfections. However, a common disadvantage is low reproducibility, which is mainly caused by variation in transfection complex size and shape. These variations can be caused by minor changes in the pH of the solutions used for the transfection, as well as the manner in which these solutions are combined. A further drawback of the calcium-phosphate method is that some cell types, including primary cells, may resist this form of DNA transfer.

Calcium-Phosphate Method*

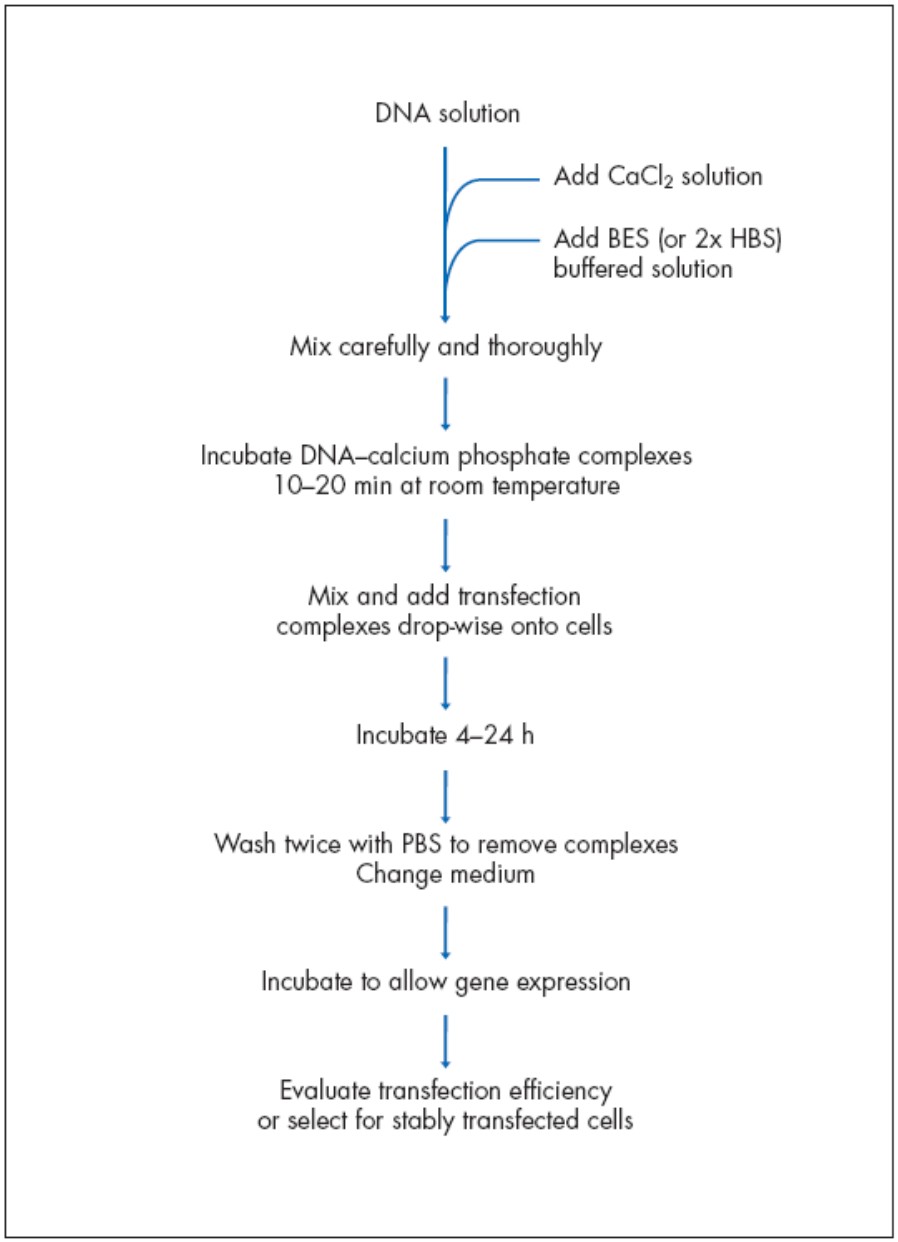

Nanocontainers

- Liposomes
- Dendrimers
- Layer by Layer Deposition
- Block Copolymer
- Shell Cross-Link

Cationic Liposome

Liposomes were first introduced in 1987 by Felgner and coworkers (9). The liposomes currently in use typically contain a mixture of cationic and neutral lipids organized into lipid bilayer structures. Transfection-complex formation is based on the interaction of the positively charged liposome with the negatively charged phosphate groups of the nucleic acid. The uptake of the liposome–DNA complexes may be mediated by endocytosis. Compared to the DEAE-dextran and calciumphosphate methods, liposomes often offer higher transfection efficiency and better reproducibility. However, one drawback of liposome-mediated transfection is that the presence of serum during the transfection procedure often lowers the transfection efficiency. For this reason, serum is often omitted when transfecting with liposomes. In many cases, the absence of serum from the medium increases the cytotoxicity of the liposome. Another drawback of classical liposome-mediated transfection is that results

- Stability

Liposomes

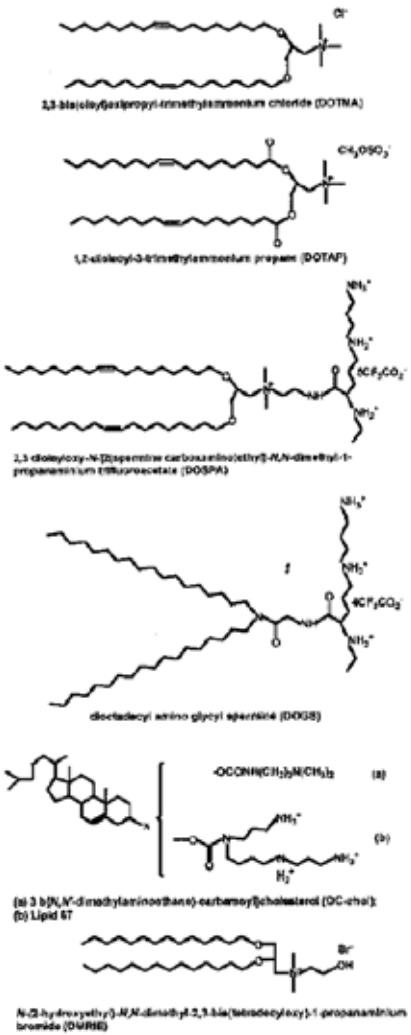

Figure 21.7 Structures of some cationic lipids commonly used in gene therapy.

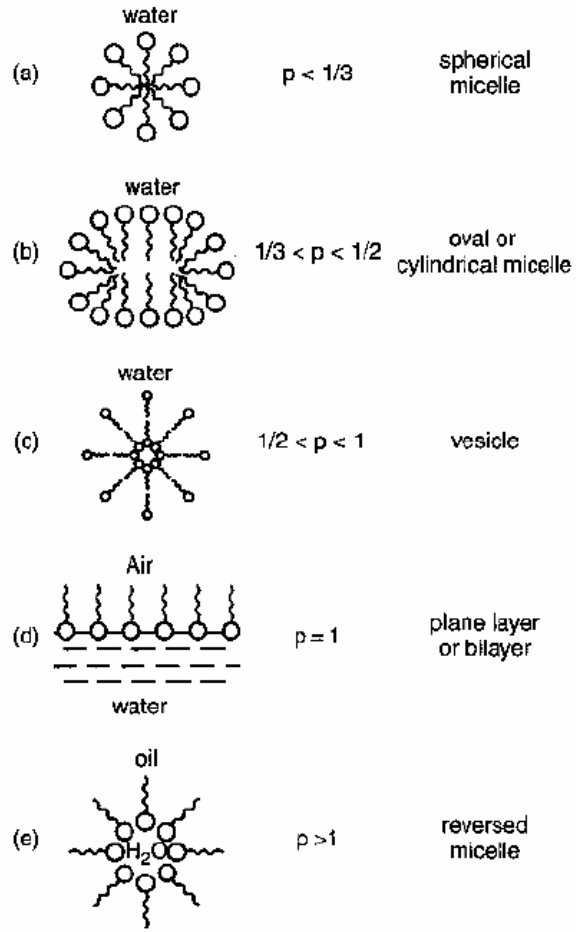

Figure 12.14. Sketch of structures formed by amphiphilic molecules at water–oil or water–air interfaces for various values of the packing parameter *p* of Eq. (12.6). [Adapted from E. Nakache et al., in Nalwa (2000), Vol. 5, Chapter 11, p. 580.]

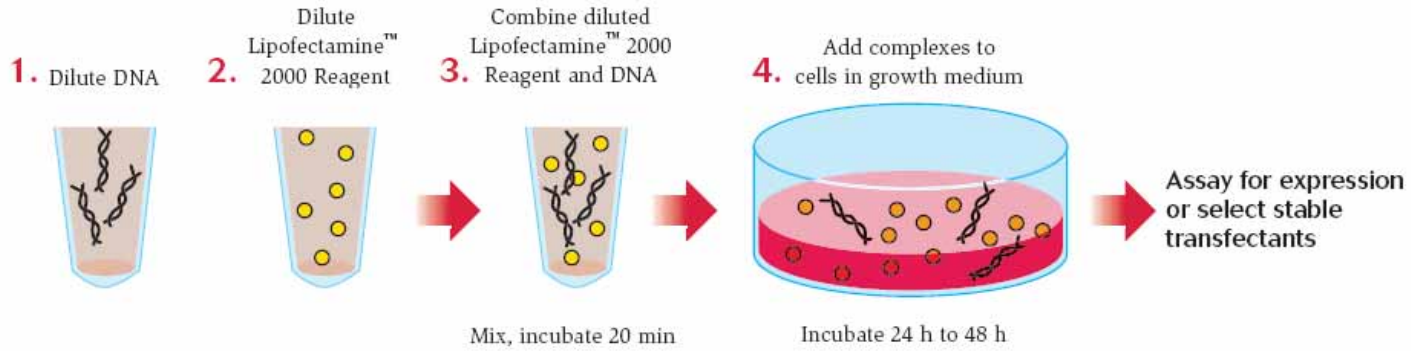

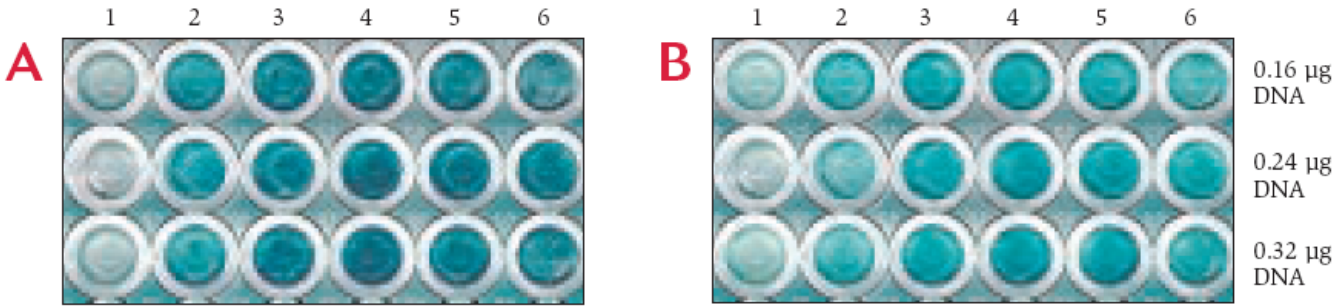

CHO-S cells were transfected with pCMV•SPORT-βgal DNA (0.16 µg to 0.32 µg) and Lipofectamine™ 2000 Reagent (0.2 µl to 1.2 µl, columns 1-6 respectively) in 96-well plates. After 24 hours, cells were stained with X-gal. **Panel A:** Cells (2 x 10^4) were plated the day before transfection in growth medium containing serum. **Panel B:** The day of transfection, cells were trypsinized, counted, and 5 x 10^4 cells were added directly to the wells containing the complexes.

Cell Line	Cell Type	Transfection efficiency (%)
293-F	Human kidney	99
293-H	Human kidney	99
CHO-S	Hamster ovary	96
COS-7L	Monkey kidney	99
BE(2)C	Human neuroblastoma	77
SKBR3	Human breast cancer	49
MDCK	Dog kidney	43
HT1080	Human fibrosarcoma	81
Human fibroblasts	Primary passaged	48
HeLa	Human cervical carcinoma	94
CV-1	Monkey kidney	70
Vero	Monkey kidney	86
PC12	Rat pheochromocytoma	85
Murine ES	Mouse embryonic stem	75
Rat Hepatocytes	Primary liver	50
E18 Cortical Neurons	Rat primary	25
E18 Hippocampal Neurons	Rat primary	30

Block Copolymers

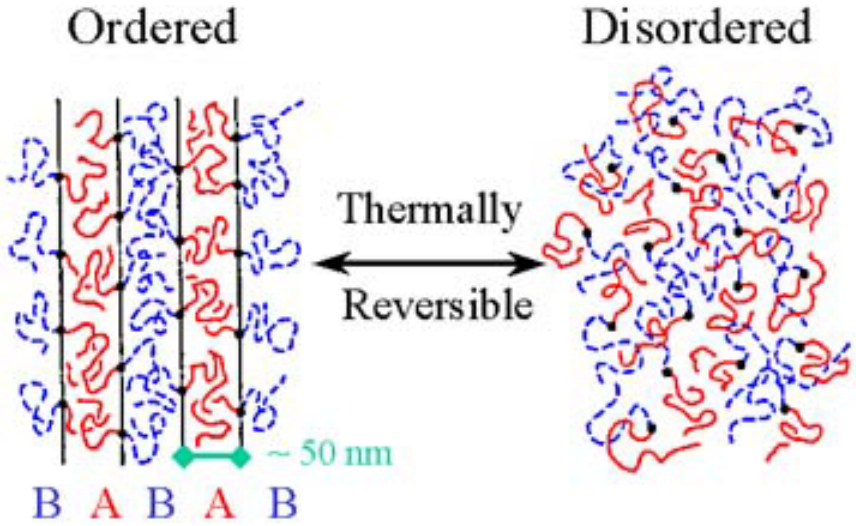

Polymer

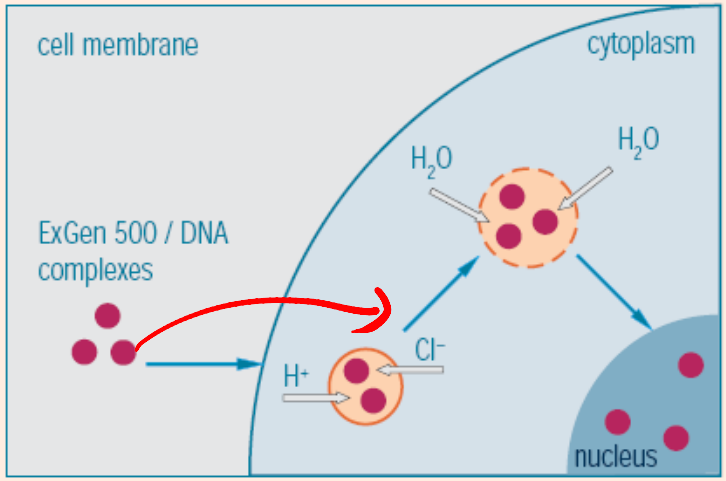

1. ExGen 500 interacts with DNA to form small, stable, highly diffusible complexes which are readily endocytosed.
2. "Proton-sponge" effect of ExGen 500 buffers endosomal pH by provoking massive proton accumulation and passive chloride influx.
3. Rapid osmotic swelling causes endosomal rupture, allowing translocation of DNA to the nucleus without DNA degradation.

Synthesis of Poly-ethylenimine

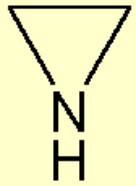

Ethylene imine

Catalyst

PEI

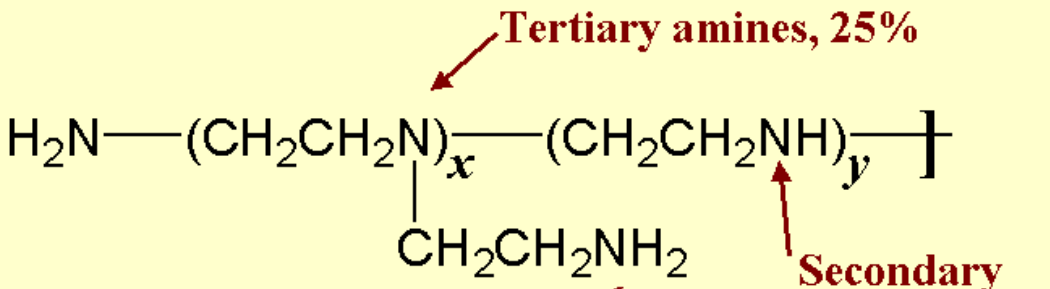

M. Hubbe

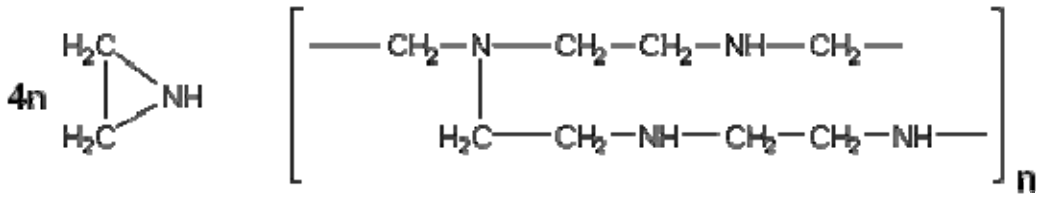

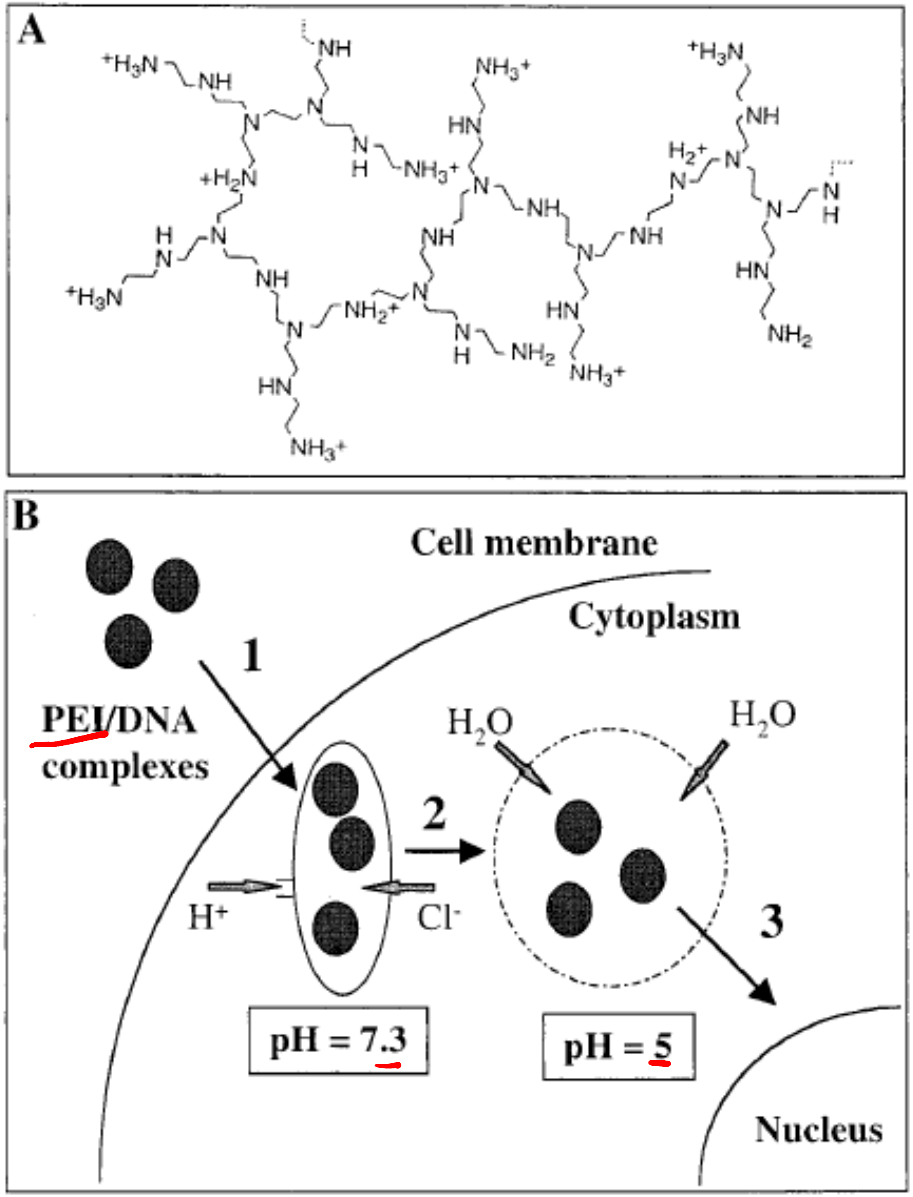

Figure 1. (A) Structure of PEI with a random topology. (B) The 'proton sponge effect': after endocytosis of the cationic complexes (1), acidic endosome buffering (2) leads to increased osmotic pressure and finally to lysis (3)

ExGen 500 performs when other transfection reagents fail

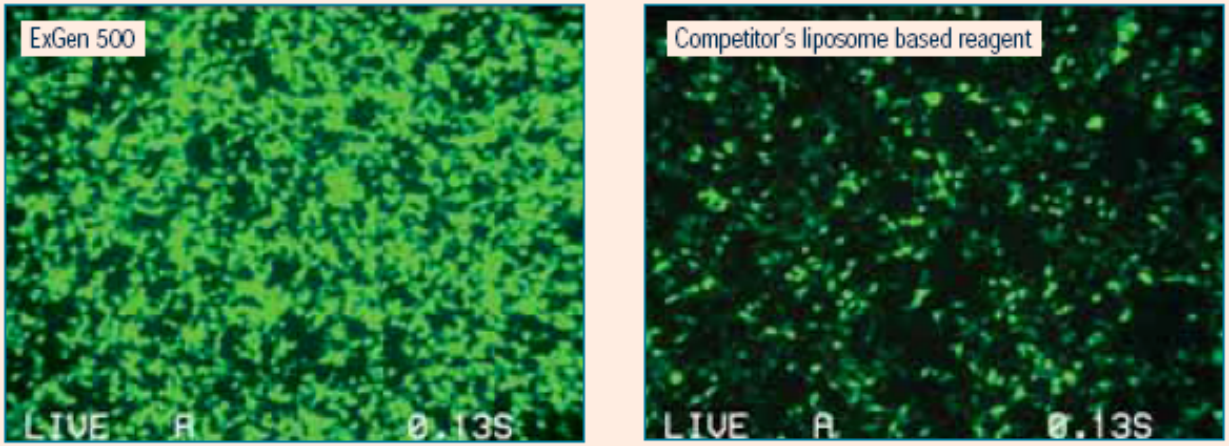

Expression of Green Fluorescent Protein (GFP) in 293 cells.
Cells were transfected with a vector containing the GFP coding sequence using ExGen 500 and competitor's liposome based reagent.

ExGen 500 transfects a wide variety of cell types

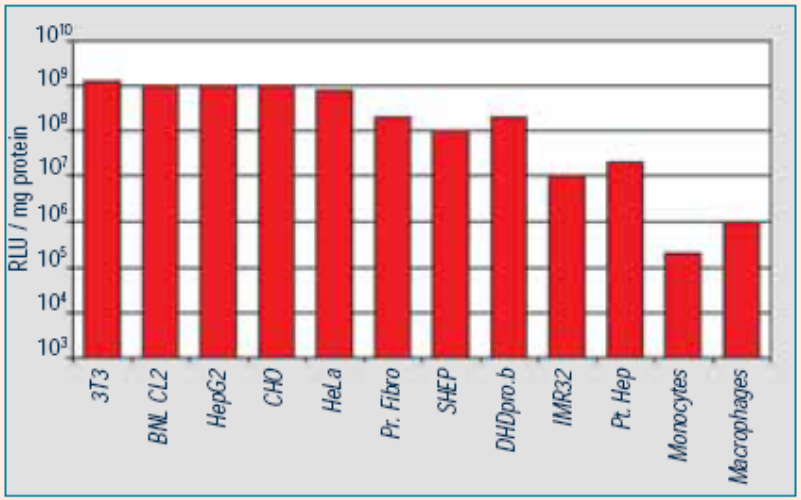

Dendrimers

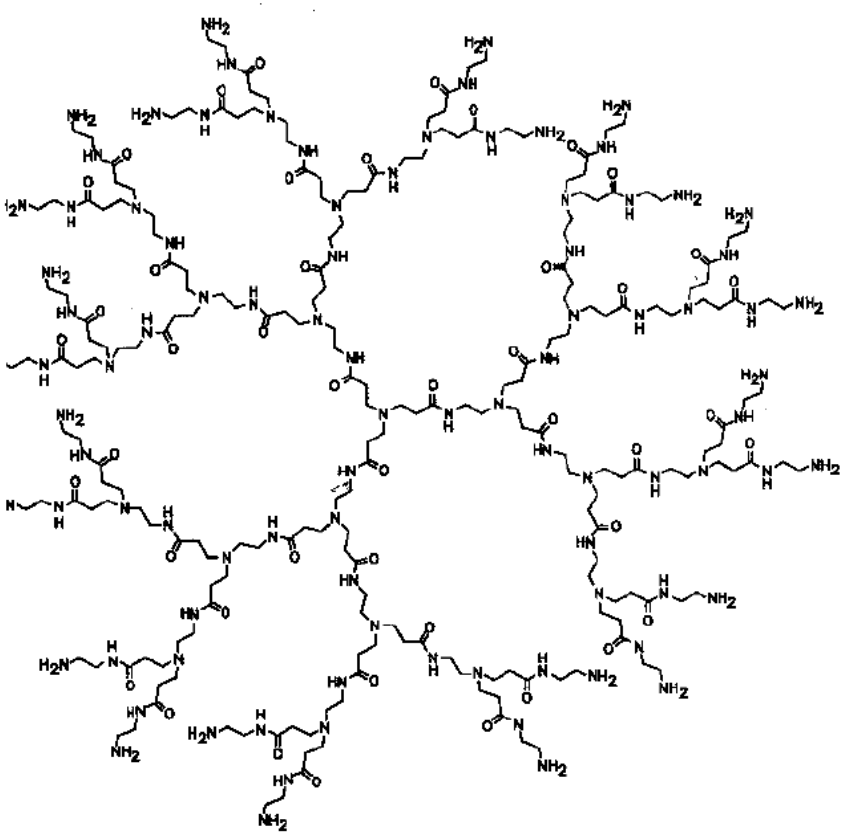

Figure 11.16. Fifth-generation polyaminoamine (PAMAM) dendrimer. [Prepared by D. A. Tomalia, H. Baker, J. R. Dewald, M. Hall, G. Kallos, S. Martin, J. Roeck, J. Ryder, and P. Smith, *Polym. J.* **17**, 117 (1985).]

Dendrimer

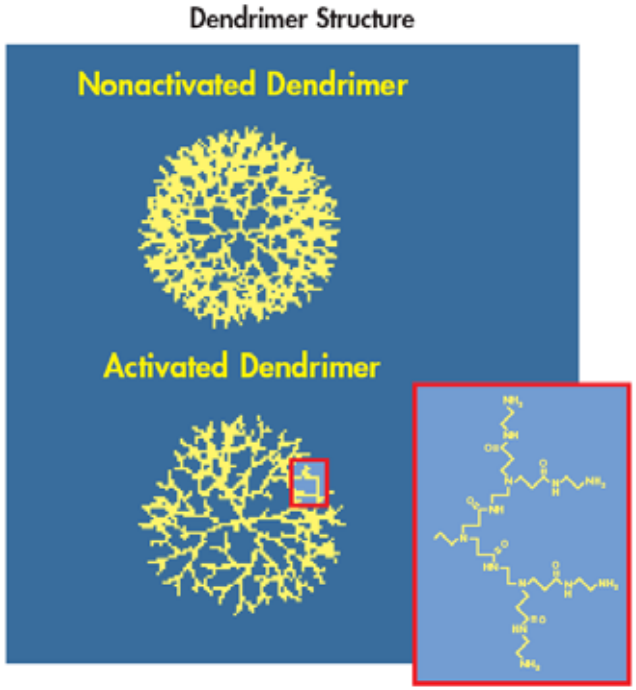

Figure 1. Schematic diagram of an activated and non-activated dendrimer. A portion of the activated dendrimer molecule is enlarged to show the chemical structure of the molecular branches.

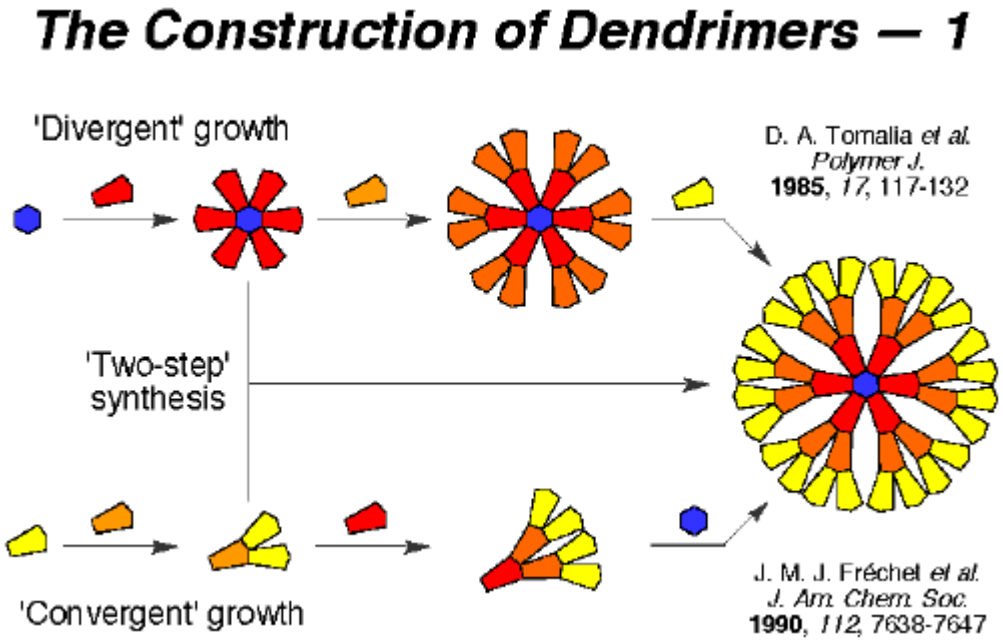

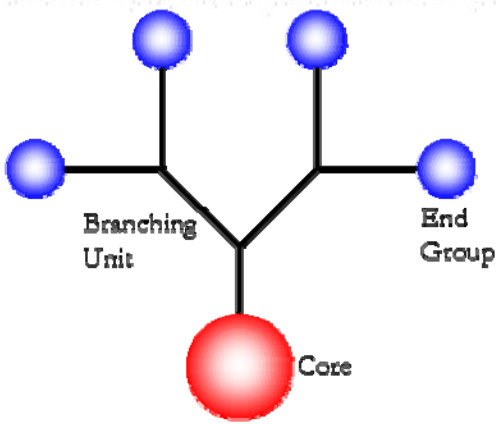

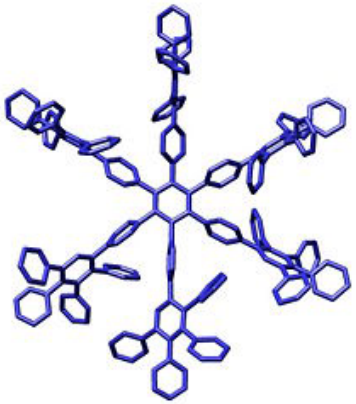

Activated-Dendrimer–DNA Interaction

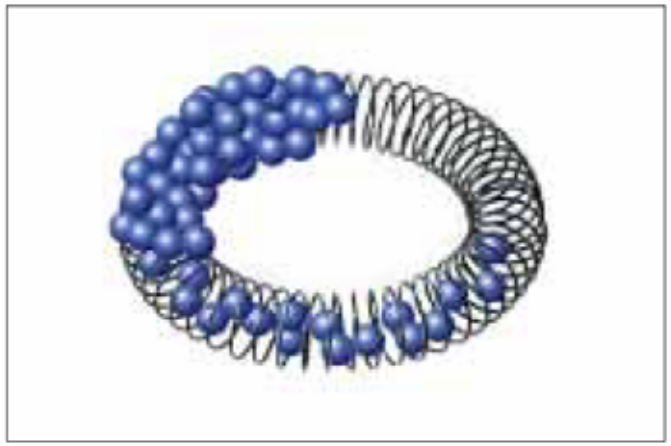

Figure 2. *Model of the activated-dendrimer–DNA complex. Activated dendrimers (purple spheres) interact with DNA (black) to form a ring-like (toroid-like) structure. The upper right section of the illustration shows naked DNA, the lower section shows the interaction between dendrimers and DNA inside the complex, and the upper left section shows the final complete coverage of DNA within the complex.*

PolyFect Reagent with HeLa Cells

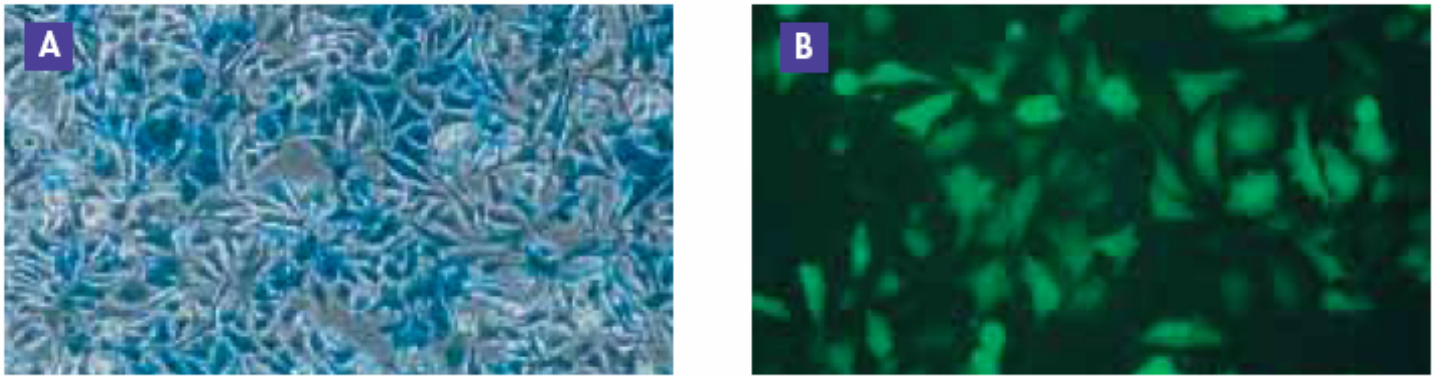

Figure 8. *Expression of* **A** *β-galactosidase and* **B** *green fluorescent protein (GFP) in HeLa cells. Cells were cotransfected in 6-well plates with β-galactosidase and GFP reporter plasmids using PolyFect Transfection Reagent and the HeLa cell protocol. Expression was visualized by X-gal staining or fluorescence microscopy 2 days post-transfection.*

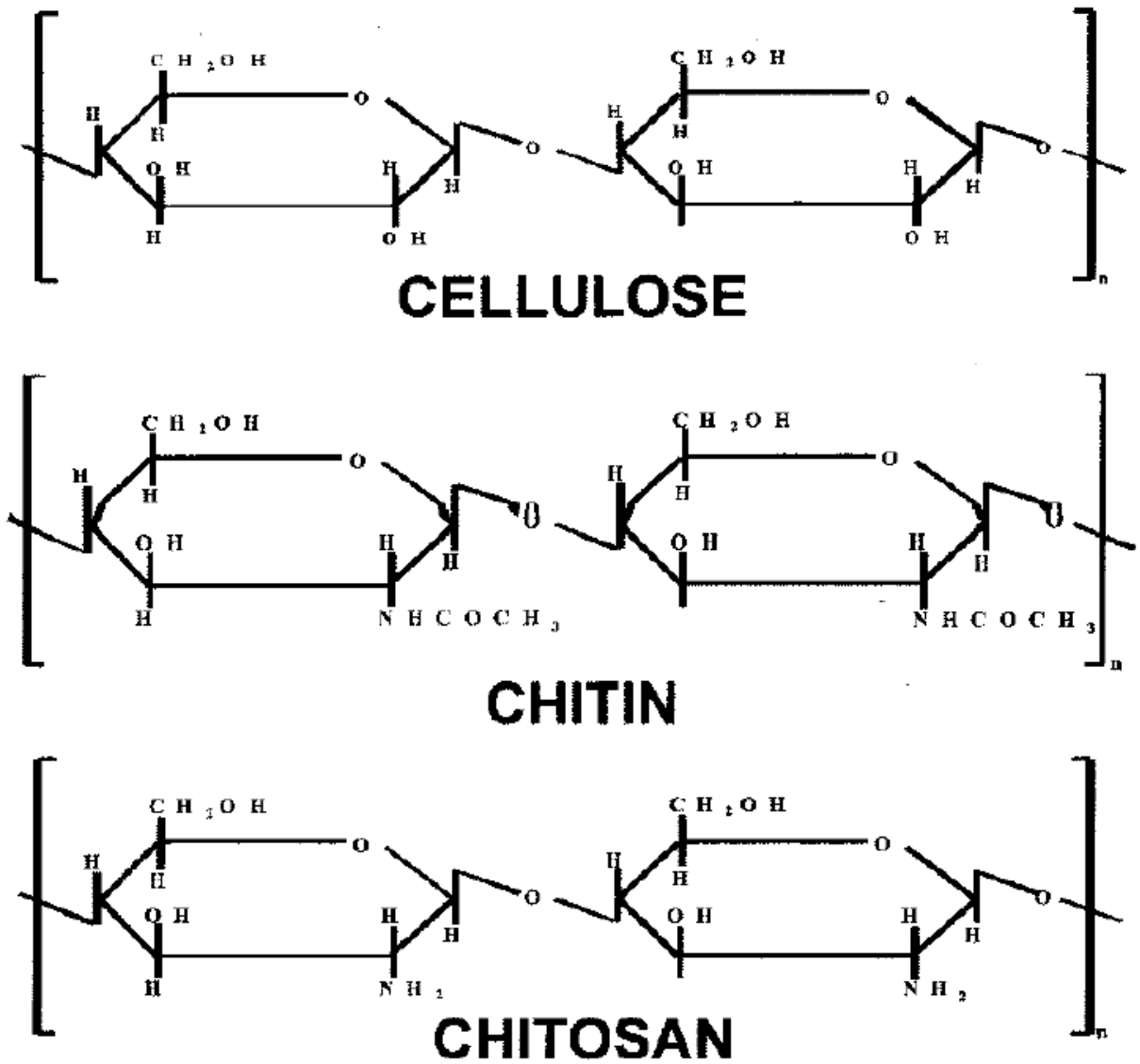

Figure 21.3 Structural similarities between cellulose, chitin, and chitosan.

Green Fluorescent Protein (GFP)

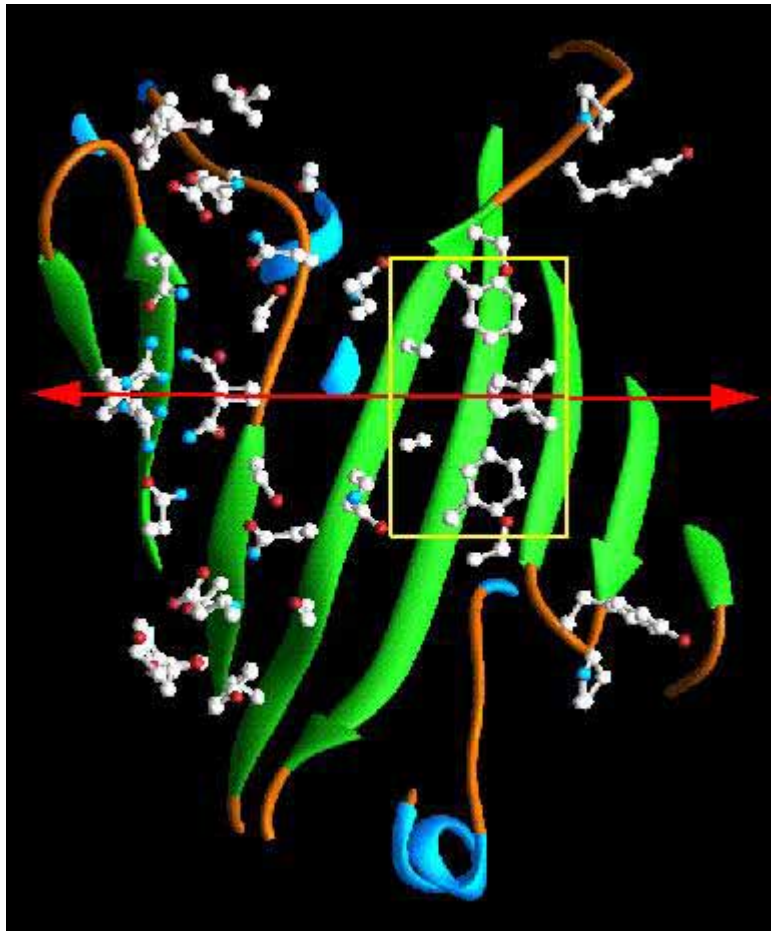

The **green fluorescent protein** (**GFP**) is a protein from the jellyfish *Aequorea victoria* that fluoresces green when exposed to blue light.

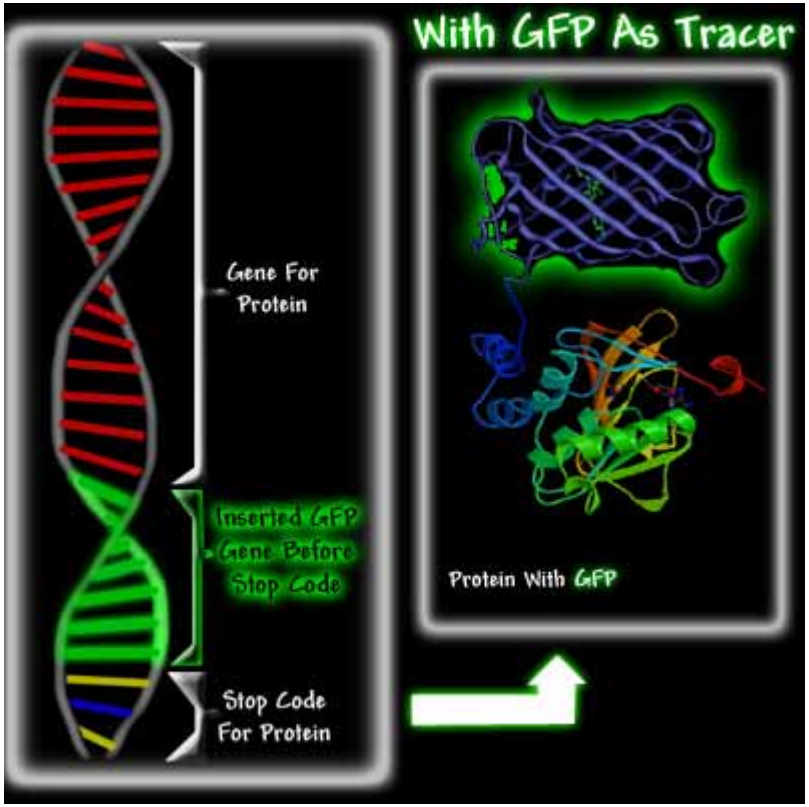

GFP Rats

Gold Nanoparticles

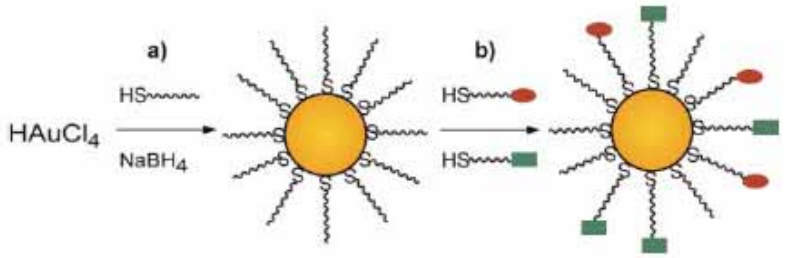

Fig. 2 Synthesis of gold MPCs using (a) the Brust–Schiffrin reaction and MMPCs *via* (b) the Murray place-exchange method.

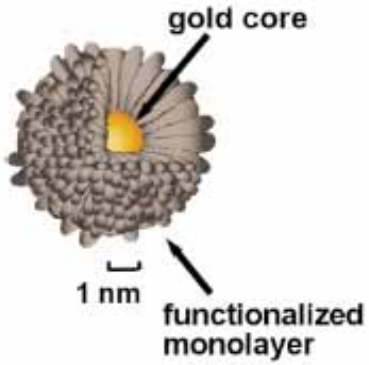

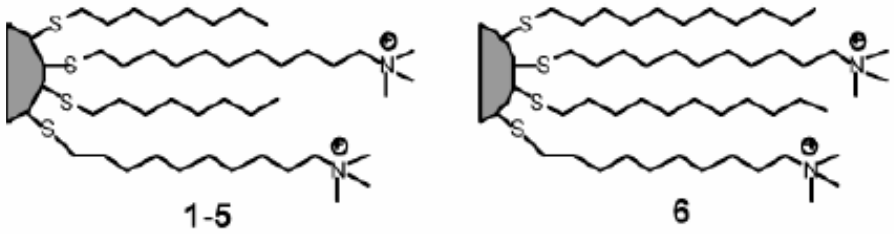

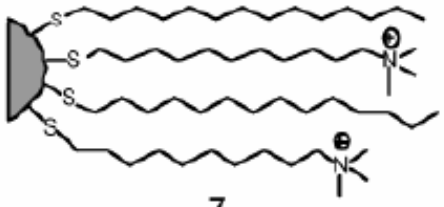

MMPC	1	2	3	4	5	6	7
% cationic coverage	100	85	68	63	58	77	89

Figure 1. MMPCs used for transfection.

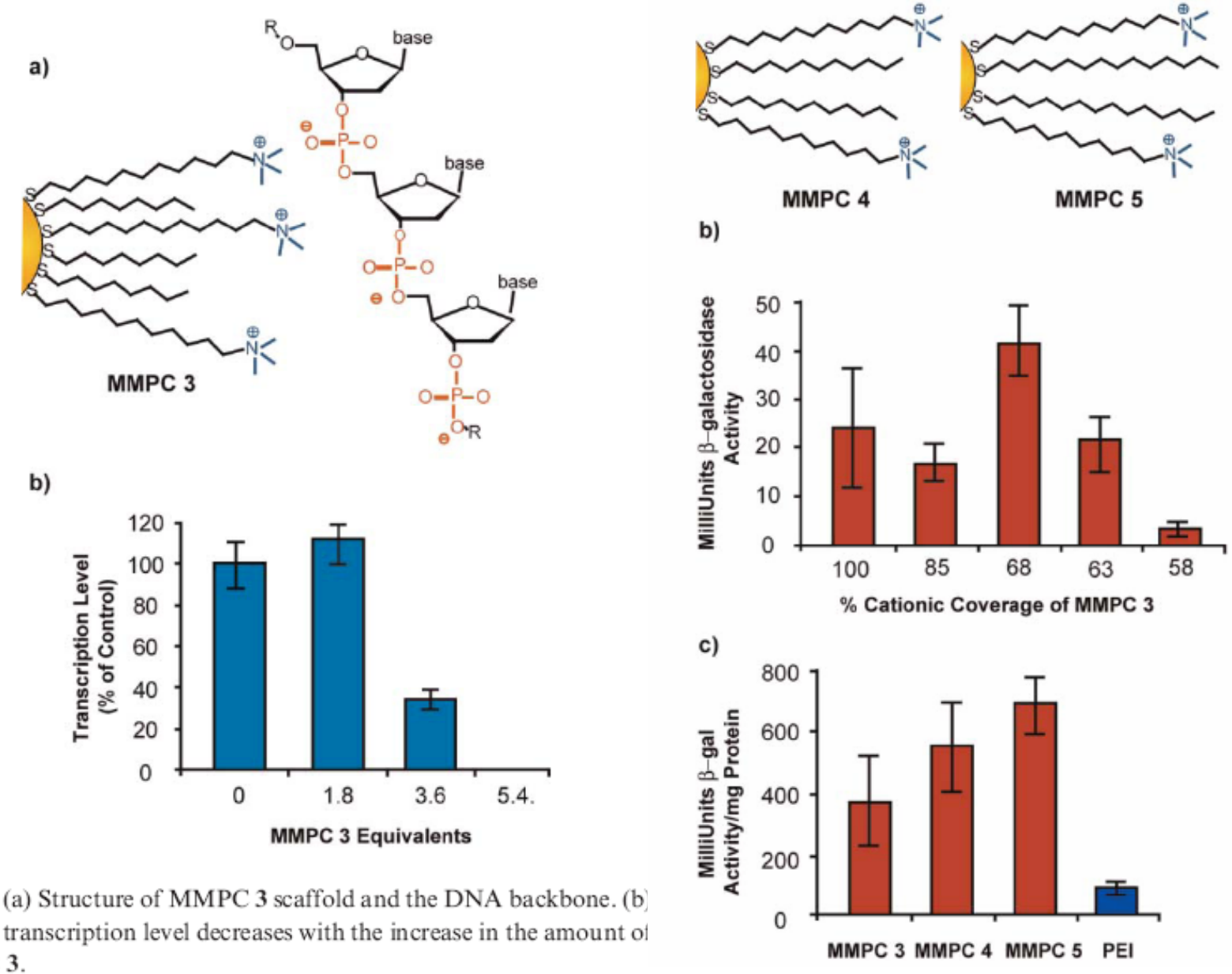

Fig. 5 (a) Structure of MMPC **3** scaffold and the DNA backbone. (b) Percent transcription level decreases with the increase in the amount of MMPC **3**.

a)

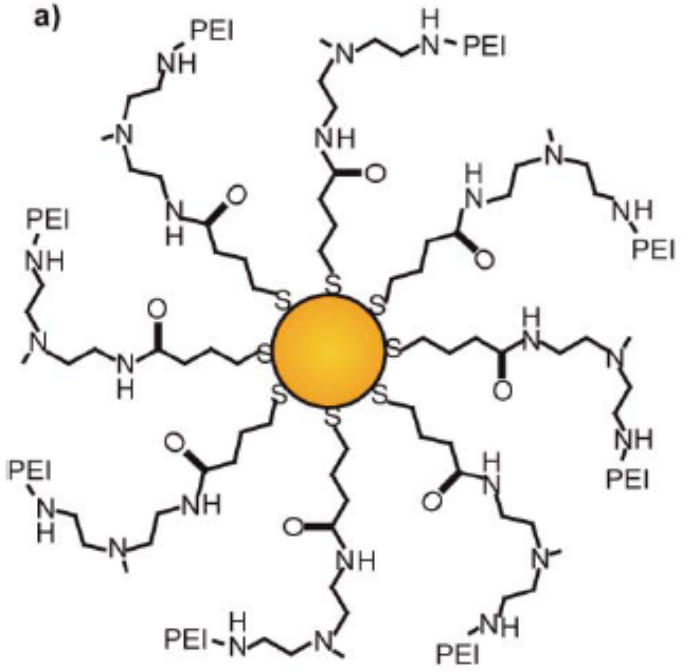
PEI
NH
N
H
O
S

MPC 6

b)

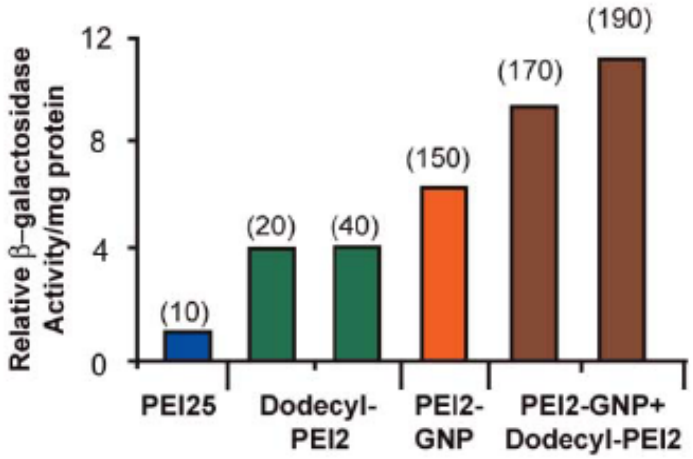
Relative β–galactosidase Activity/mg protein
12
8
4
0
(10)
(20)
(40)
(150)
(170)
(190)
PEI25
Dodecyl-PEI2
PEI2-GNP
PEI2-GNP+ Dodecyl-PEI2

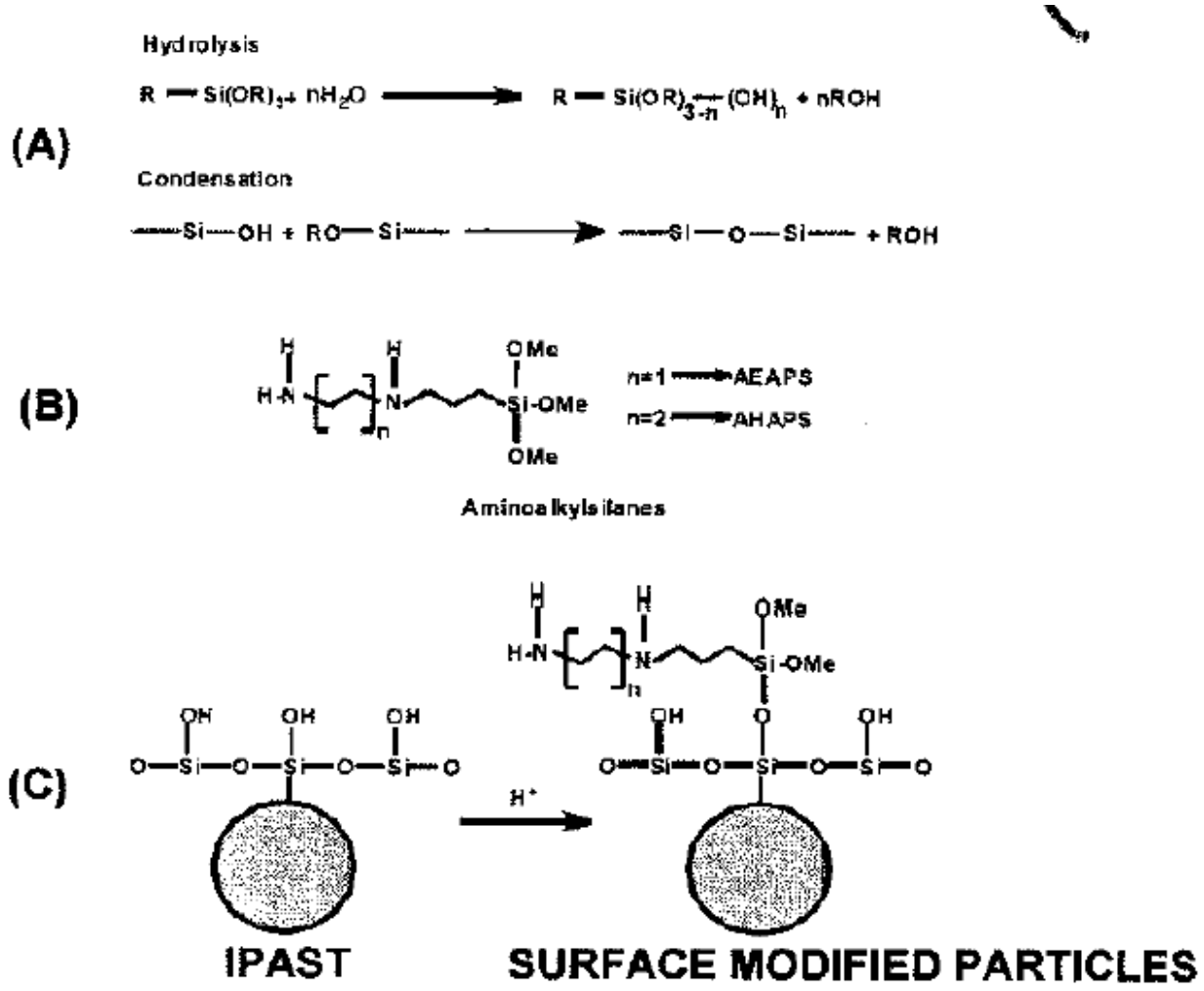

Figure 21.11 (A) Hydrolysis and condensation of unmodified particles. (B) Alkylaminoalkanes. (C) Modification scheme.

Parameters

- Cell density
- Amount of DNA
- Transfection reagent to DNA ratio
- Incubation period with DNA complex
- Incubation time following transfection

Gene Delivery

- Transfection- the delivery of foreign molecules such as DNA and RNA into eukaryotic cells
- Naked DNA is not suitable for in-vivo transport of genetic materials-> degradation by serum nucleases
- Ideal gene delivery system
  - Biocompatible
  - Non-immunogenic
  - Stable in blood stream
  - Protect DNA during transport
  - Small enough to extravagate
  - Cell and tissue specific

Synthesis of Nanoparticles and Surface Modifications

Synthesis of Silver Nanoparticles

1. ***A solution of $AgNO_3$ (1.0×10^{-3} M) in deionized water was heated until it began to boil.***
2. ***Sodium citrate solution was added dropwise to the silver nitrate solution as soon as the boiling commenced. The color of the solution slowly turned into grayish yellow, indicating the reduction of the Ag+ ions.***
3. ***Heating was continued for an additional 15 min, and then the solution was cooled to room temperature before employing for further experimentation.***

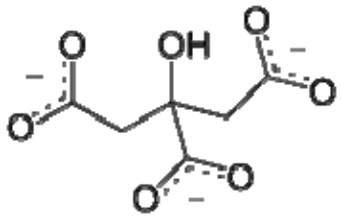

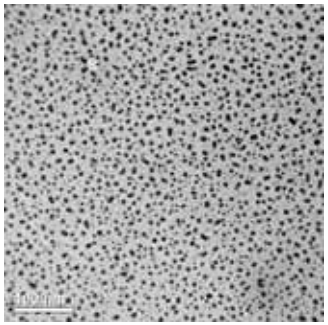

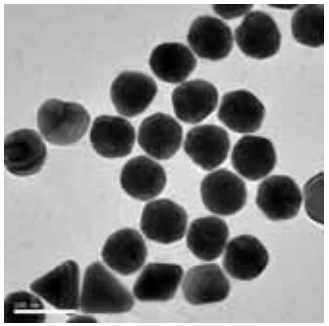

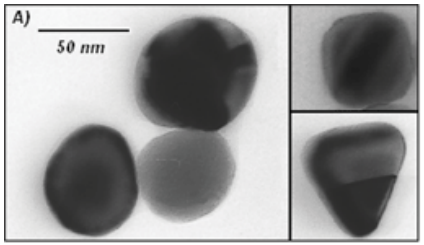

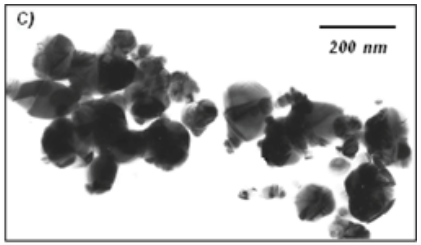

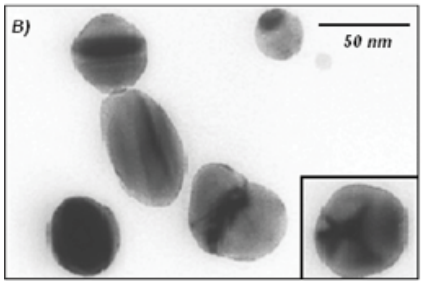

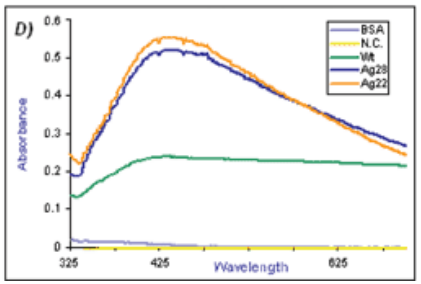

Synthesis of Gold Nanoparticles

1. ***Add 20 mL of 1.0 mM $HAuCl_4$ to a 50 mL round bottom flask on a stirring hot plate.***
2. ***Add a magnetic stir bar and bring the solution to a boil.***
3. ***To the boiling solution, add 2 mL of a 1% solution of trisodium citrate dihydrate***
4. ***The gold sol gradually forms as the citrate reduces the gold(III). Stop heating when a deep red color is obtained.***

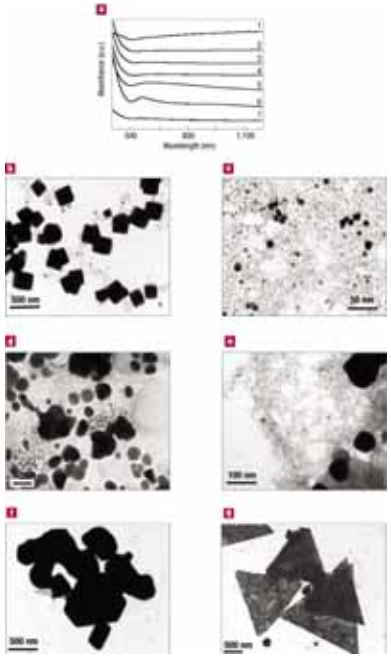

(1) $$M_xO_y \xrightarrow[(\text{medium})\ \Delta_T]{\text{Reducing Agent}} M_n + H_2O$$

(Reducing Agent = R - COH)

(2) $$M(L)_x \xrightarrow[(\text{medium})\ \Delta_T]{\text{Reducing Agent}} M_n + L^-$$

($L=NO_3^-, C_2H_5O^-$)

(Reducing Agent = R - COH)

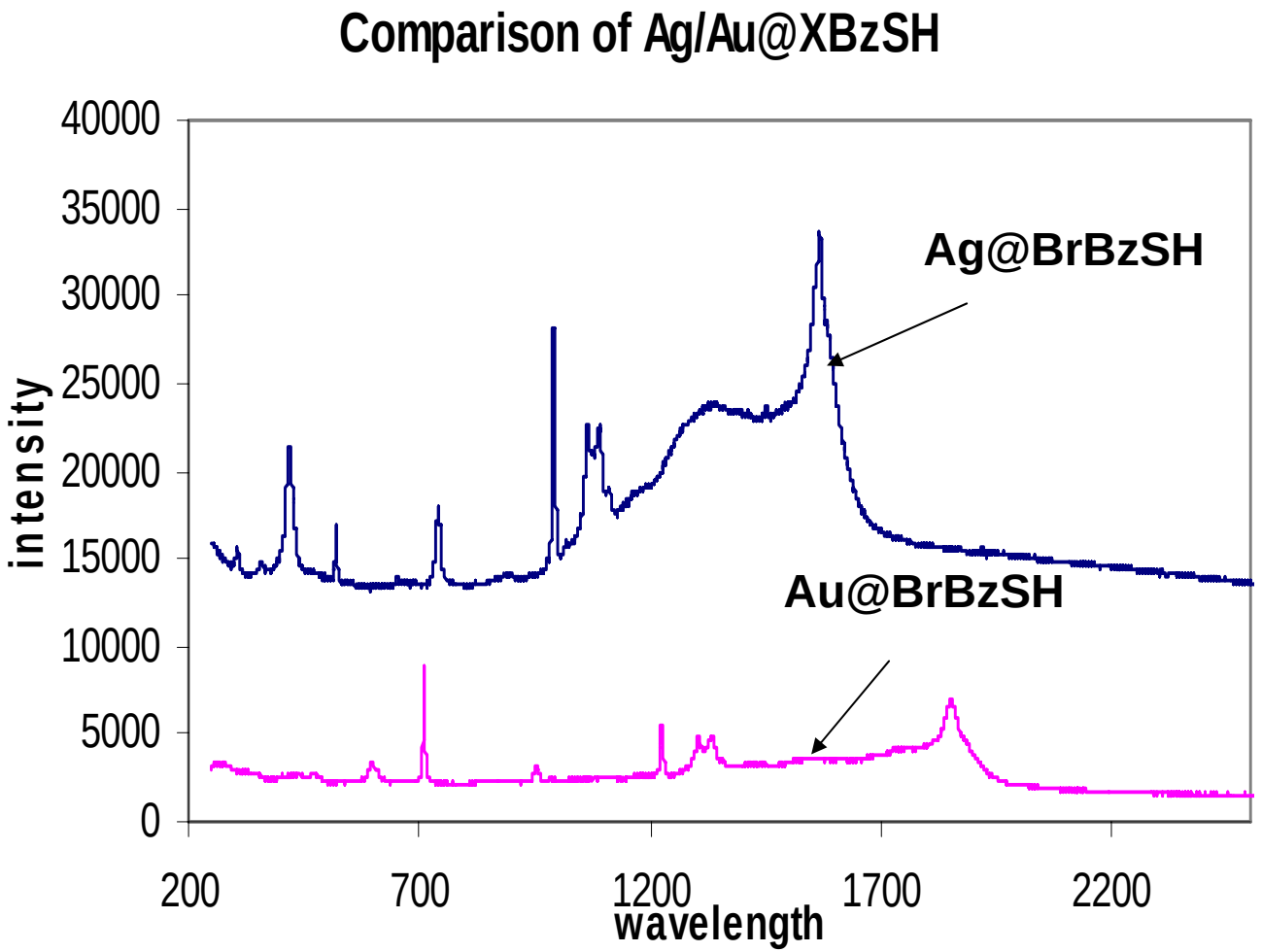
Comparison of Ag/Au@XBzSH
40000
35000
30000
25000
20000
15000
10000
5000
0
intensity
200
700
1200
1700
2200
wavelength
Ag@BrBzSH
Au@BrBzSH

Construction of Core Shell Ag/Au@SiO_2 Nanoparticles

1. *Under vigorous stirring, 1 ml of the silver/ gold colloids solution was mixed with 250 mL of isopropanol and 25 mL of deionized water.*
2. *Immediately after the addition of 4 mL of 30% ammonium hydroxide, different amounts of tetraethoxysilane (TEOS) were added to the reaction mixture.*
3. *To obtain different silica layer thicknesses, TEOS solutions with a concentration between 50% and 100% was added to the suspension. The reaction was stirred at room temperature for 30 minutes and then was allowed to age without agitation at 4℃ overnight.*
4. *Each suspension of silica-coated silver/gold nanoparticles was washed and centrifuged, followed by re-suspension in water. The thickness of the silica layers was determined from TEM images .*

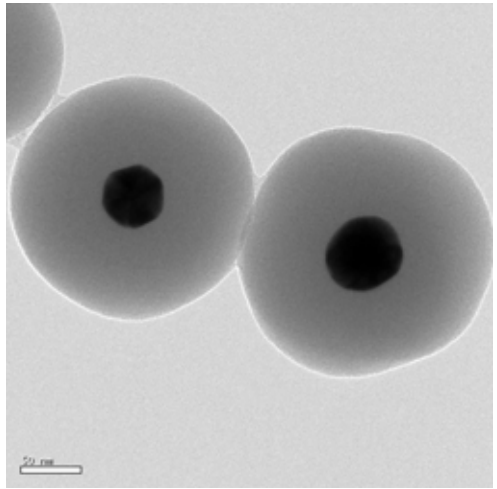

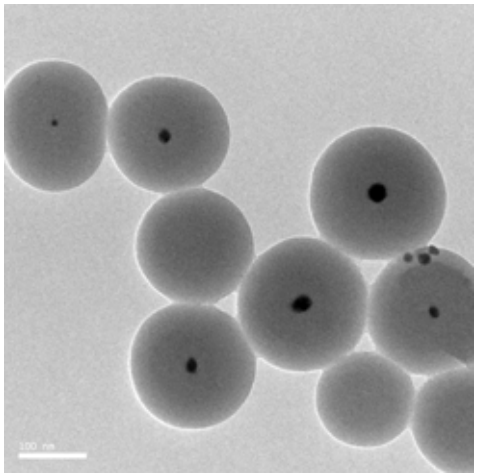

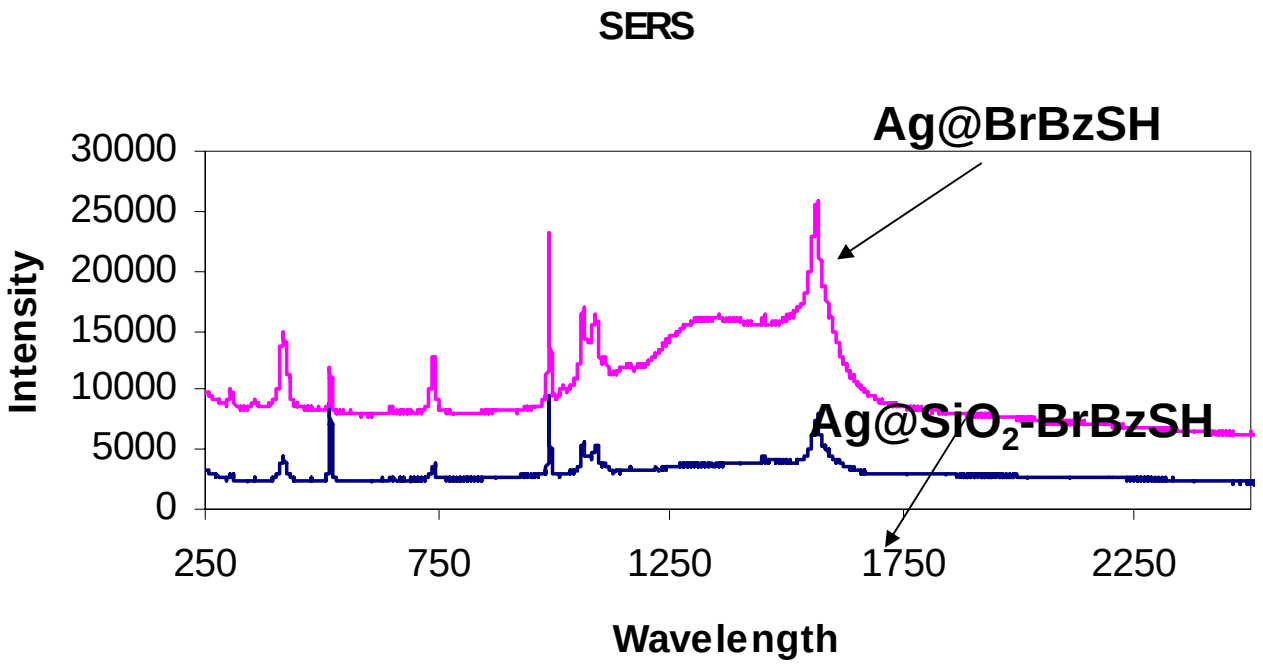
SERS
Ag@BrBzSH
Ag@SiO2-BrBzSH
Intensity
30000
25000
20000
15000
10000
5000
0
250
750
1250
1750
2250
Wavelength

Core-Shell Nanoparticles

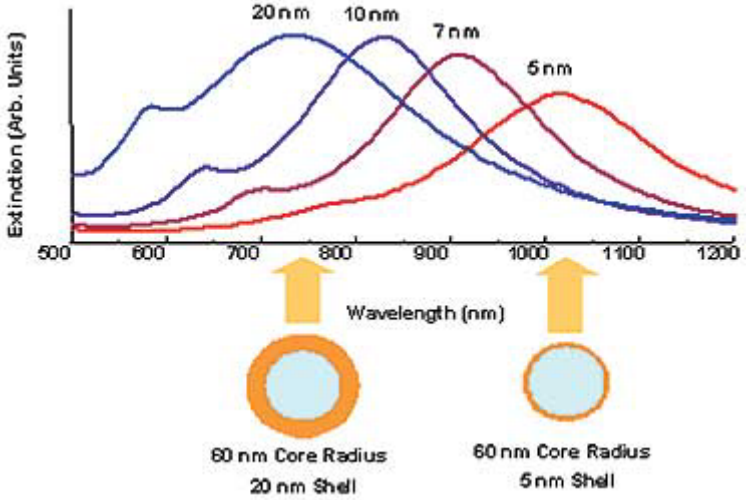

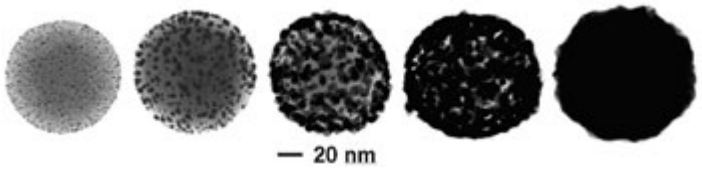

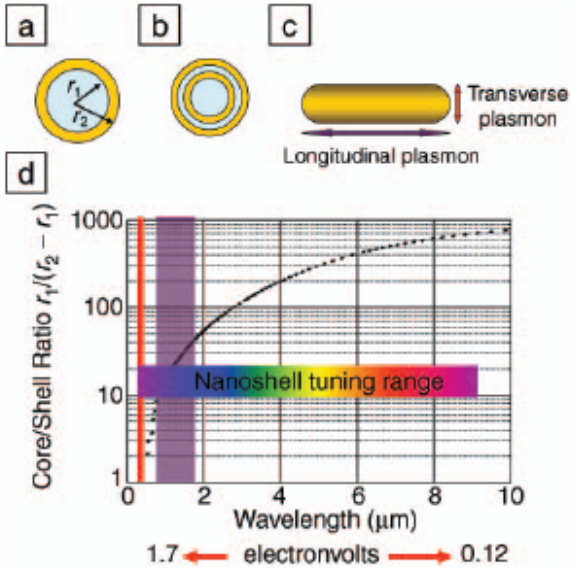

Figure 1. (a) Schematic illustration of a silica-core, gold-shell nanoshell, indicating inner (r_1) and outer (r_2) radii of the shell layers. (b) Depiction of a four-layer, concentric nanoshell. (c) Schematic illustration of a metallic nanorod. (d) Plot of nanoshell resonance as a function of core and shell dimensions, overlaid with reported spectral ranges of nanorod resonances (red, transverse plasmon; purple, longitudinal plasmon), and reported nanoshell and concentric nanoshell combined spectral range of plasmon response.

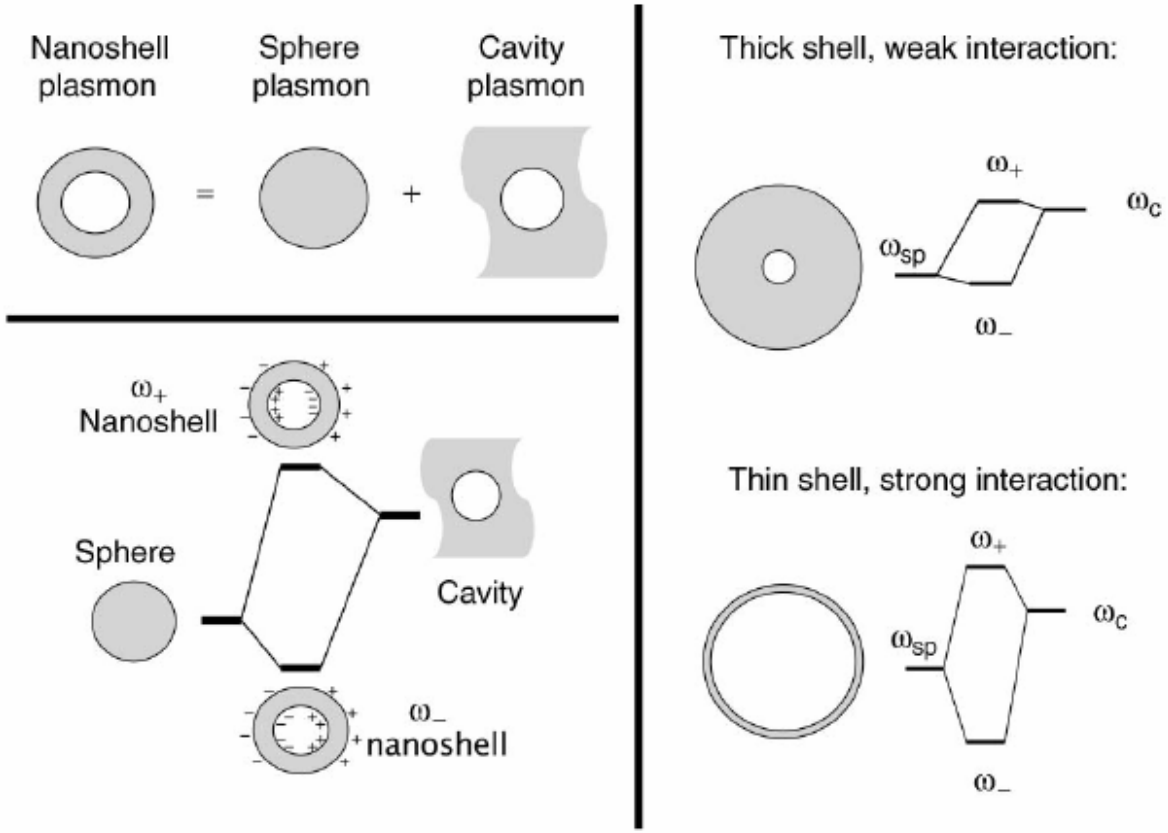

Figure 2. Plasmon hybridization and the sphere–cavity model for nanoshells: the interaction between a sphere (resonance frequency, ω_{sp}) and a cavity plasmon (resonance frequency, ω_c) is tuned by varying the thickness of the shell layer of the nanoparticle. Two hybrid plasmon resonances, the ω_- "bright," or "bonding," plasmon and the ω_+ "dark," or "anti-bonding," plasmon resonances are formed. The lower-energy plasmon couples most strongly to the optical field.

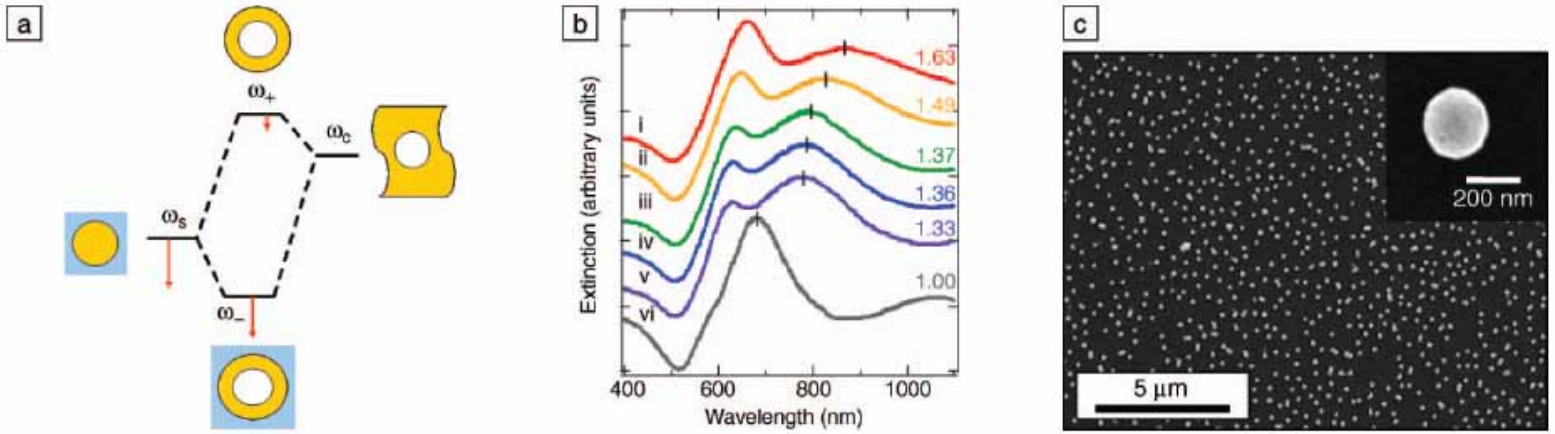

Figure 5. (a) Plasmon hybridization picture applied to surface plasmon resonance sensing with nanoshells: the low-energy "bonding" plasmon, ω_-, is sensitized to changes in its dielectric environment. The blue background schematically denotes the embedding medium for the nanoparticle. (b) Experimental curves showing plasmon resonance shifts for nanoshell-coated films in various media: (i) carbon disulfide, (ii) toluene, (iii) hexane, (iv) ethanol, (v) H_2O, and (vi) air. The index of refraction for each embedding medium is noted on the far right of the spectra. Spectra are offset for clarity. (c) Scanning electron micrograph of nanoshells deposited onto a poly(vinyl pyridine) functionalized glass surface, as used to acquire data in (b). Inset: individual nanoshell.

Preparation of Fe_3O_4@Ag/Au

1. *To the magnetic nanoparticle suspension obtained from commercial company, add 50 ml of a solution of Au (III) salt or Ag (I) salt at concentration of 0.01–1% mmol/L , shaking for 30 minutes, allowing Au (III) or Ag (I) ion to absorb on the surface of magnetic nanoparticle sufficiently,*
2. *Then adding 15–40 ml of reducing agent, such as hydroxylamine hydrochloride at concentration of 40 mmol/L, reacting for 5–40 minutes.*
3. *Further adding 1–10 ml of a solution of Au (III) salt or Ag (I) salt at concentration of 0.01–1%, shaking for 10 minutes, coating a reduced layer of gold or silver on the surface of the magnetic nanoparticle, forming super-paramagnetic composite particles having core/shell structure, separating magnetically, washing repeatedly with distilled water.*

.

Nanorods

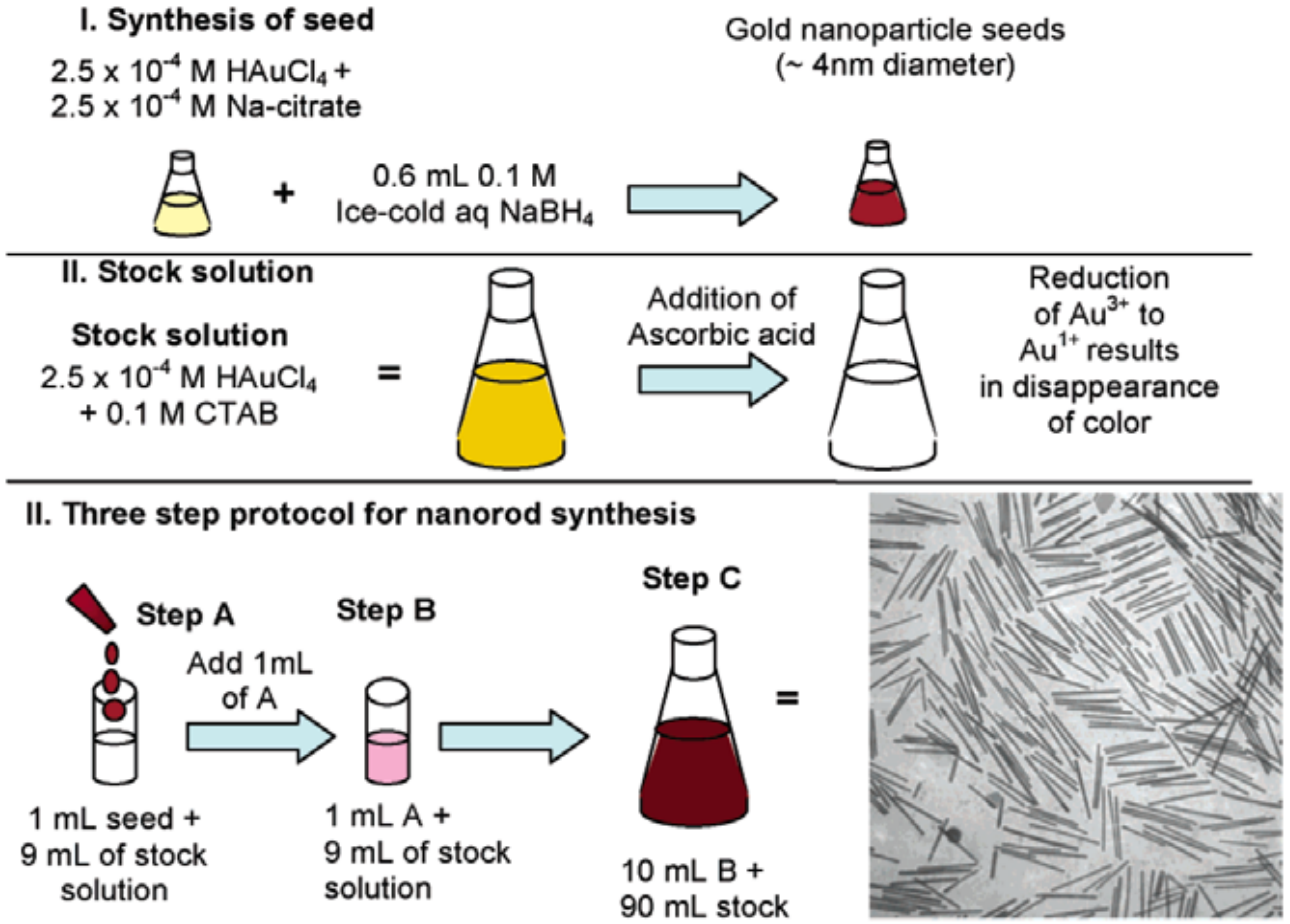

Figure 2. Seed-mediated growth approach to making gold and silver nanorods of controlled aspect ratio. The specific conditions shown here, for 20 mL volume of seed solution, lead to high-aspect ratio gold nanorods. (bottom right) Transmission electron micrograph of gold nanorods that are an average of 500 nm long.

J. Phys. Chem. B **2005,** *109,* 13857−13870

Directional Growth

Cetrimonium bromide ($(C_{16}H_{33})N(CH_3)_3Br$) (CTAB)

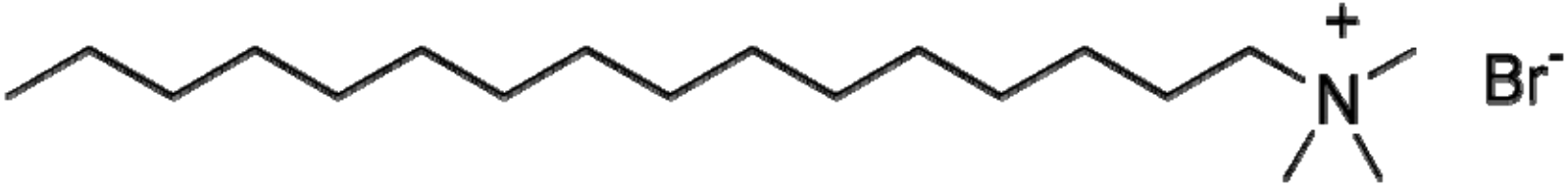

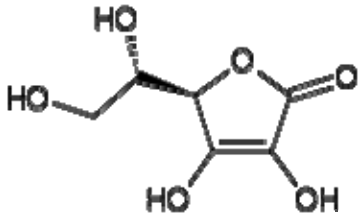

Ascorbic acid

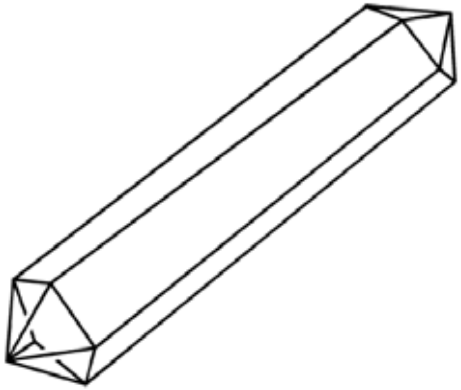

Figure 5. Cartoon of the crystallography of gold nanorods. The direction of elongation is [110]. The cross-sectional view is a pentagon; each end of the rod is capped with five triangular faces that are Au{111}. The sides of the rods are not as well-defined; either Au{100} or Au{110} faces, or both.

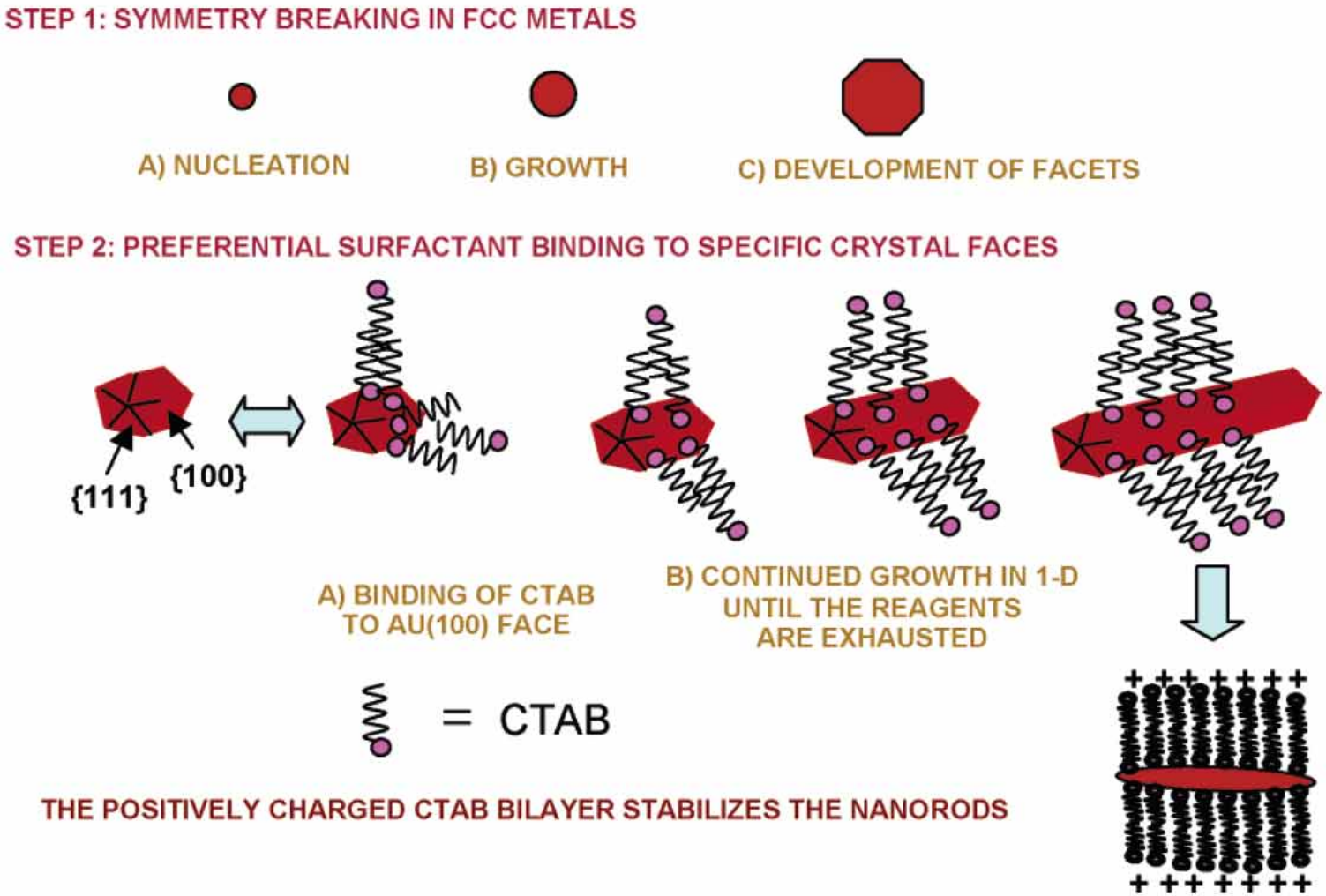

Figure 8. Proposed mechanism of surfactant-directed metal nanorod growth. The single crystalline seed particles have facets that are differentially blocked by surfactant (or an initial halide layer that then electrostatically attracts the cationic surfactant). Subsequent addition of metal ions and weak reducing agent lead to metallic growth at the exposed particle faces. In this example, the pentatetrahedral twin formation leads to Au {111} faces that are on the ends of the nanorods, leaving less stable faces of gold as the side faces, which are bound by the surfactant bilayer.

Nanorods

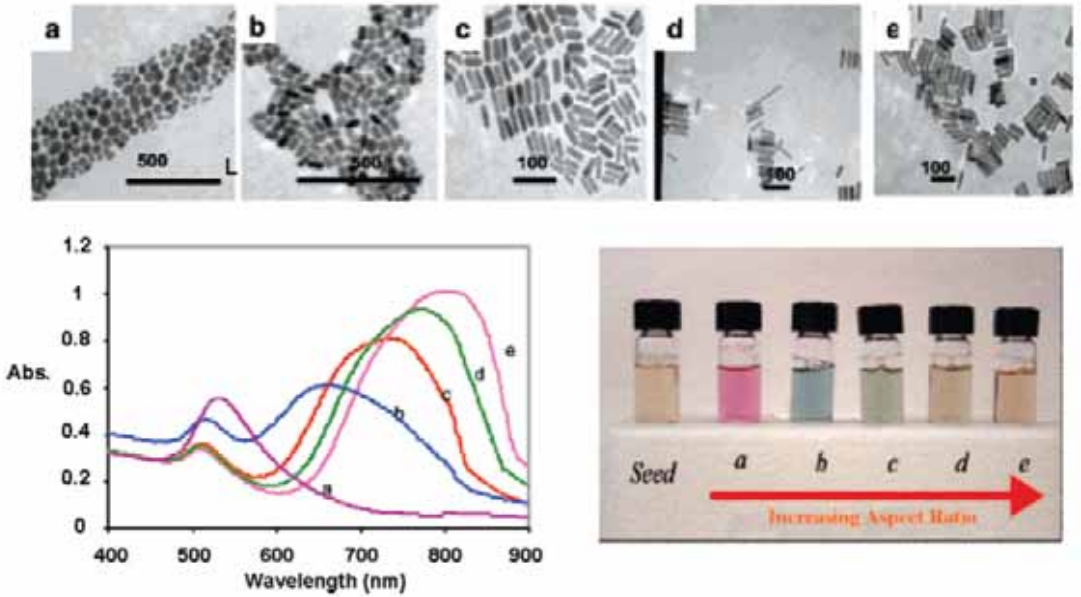

Figure 3. Transmission electron micrographs (top), optical spectra (left), and photographs (right) of aqueous solutions of Au nanorods of various aspect ratios. The seed sample has an aspect ratio of 1. Samples a, b, c, d, and e have aspect ratios of 1.35 ± 0.32, 1.95 ± 0.34, 3.06 ± 0.28, 3.50 ± 0.29, and 4.42 ± 0.23, respectively. Scale bars: 500 nm for a and b, 100 nm for c−e. Reprinted with permission from ref 16. Copyright 2005 American Chemical Society.

Nanocube and Nanorice

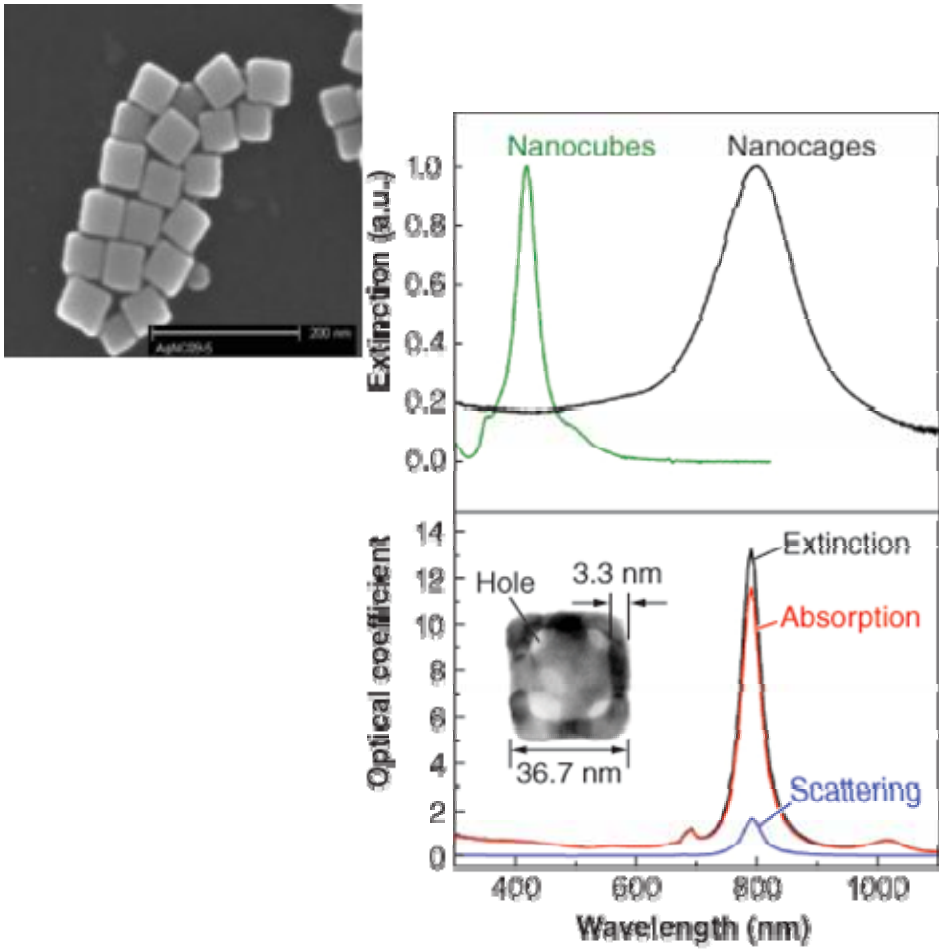

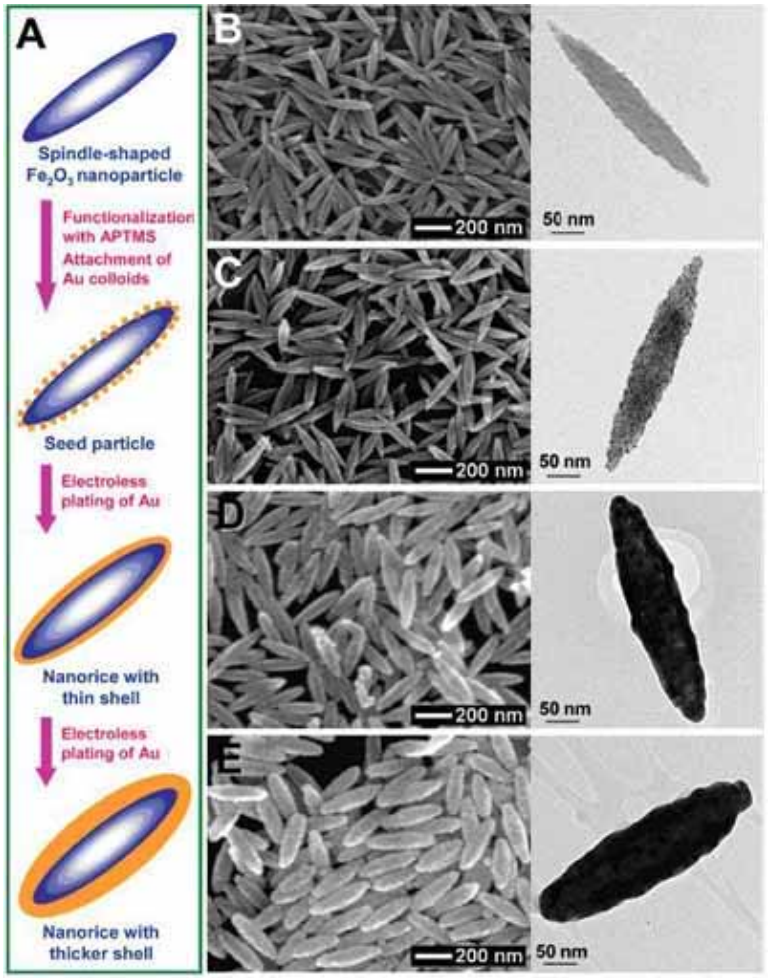

The graphic above depicts various magnitudes of nanorice, which is a rice-shaped nanoparticle with a non-conducting core made of iron oxide and covered by a metallic shell made of gold. Scientists plan to attach the nanorice to scanning probe microscopes to obtain very clear image quality that surpasses today's technology. For the Air Force, this technology could be used as a tool to develop new high-speed optoelectronic materials and to monitor chemical reactions. (Graphic provided by Prof. Naomi Halas)

Synthesis of CdSe Quantum Dots

Synthesis of TOPO/HDA capped quantum dots of CdSe

Cadmium acetate (0.107g, 0.4mmol) and oleic acid (0.27mL, 0.4mmol) in 1:2 ratio were placed in a two neck flask degassed and refilled with nitrogen, stirred at 120-130 ^{0}C under nitrogen atmosphere for 2-3 hours, obtained a clear light yellow solution. Then a mixture of capping reagent i.e. 6g of hexadecylamine (HDA) and 6g of tri-octylphosphine oxide (TOPO) prepared in separate flask was added at the same temperature and stirring was done for another 30min at temperature ~ 350 ^{0}C. The temperature was reduced and TOPSe was added at different temperatures at 250 ^{0}C through syringe immediately the color of reaction mixture became dark brown (TOPSe was prepared simultaneously in a separate vessel, appropriate quantity of Se (0.032g) powder was heated in 2mL tri-octyl phosphine (TOP) at 70-90 ^{0}C for about an hour to get a clear solution of TOPSe), stirring was continued for another 30min aliquots were taken from the reaction solution to monitor the reaction. The temperature of the reaction was reduced the stirring was done for another 1-2 hours. 50mL toluene was added before the cooling the reaction to prevent the solidification of TOPO and HDA. It was centrifuged at 3000rpm for 15min, a pallet was discarded, the supernatant solution was treated with the methanol for precipitation of CdSe nano-crystals, centrifuged at 7000rpm washed with methanol (3 x 6mL) to get product. A red residue was obtained which was re-dispersed in toluene.

Synthesis of CdSe Quantum dots

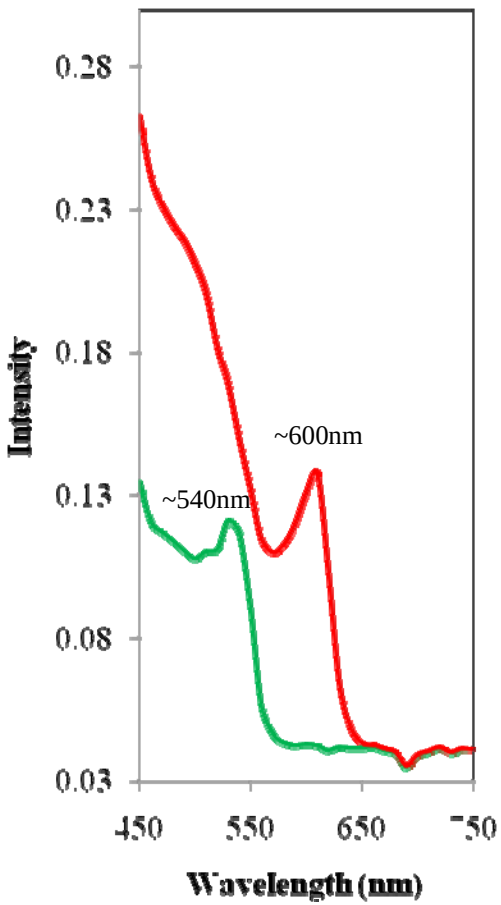

FWHM= ~28nm ± 2

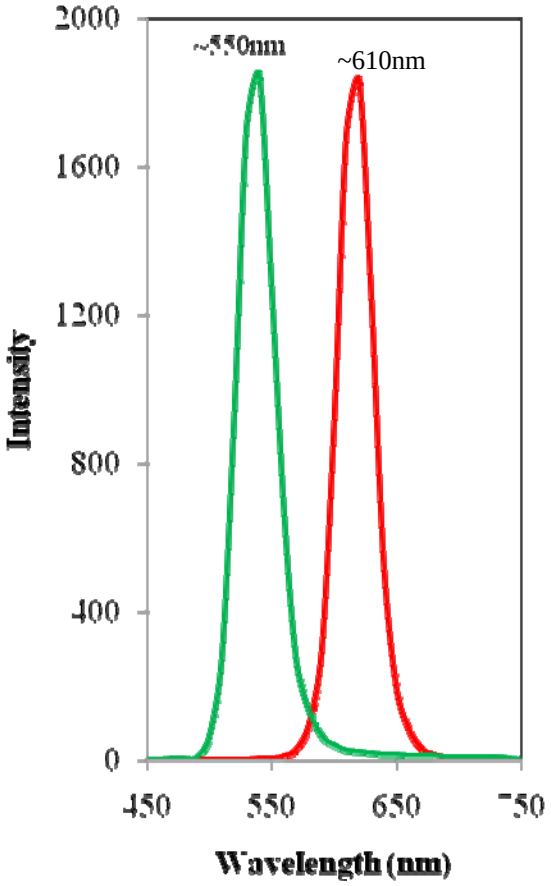

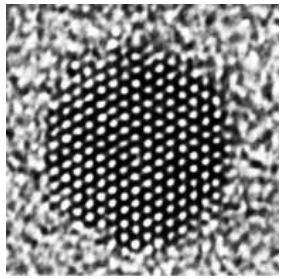

Cooperative UV and PL spectra of CdSe core

Synthesis of CdSe/ZnS Quantum Dots

20mL (31mg, 0.16 mmol) colloidal solution of CdSe QDs from stock solution (54mg dissolved in 35mL toluene) was placed in a two-neck flask. TOPO (6g) and HAD (6g) were added and then toluene was removed through vacuum, flask refilled with nitrogen. The reaction mixture was heated at 350 ^{0}C for two hours. In another flask zinc acetate in 1:3 ratio with respect of CdSe and was dissolved in 4mL of oleic acid stirred at 120 ^{0}C for 2 hours obtained a light yellow coloured solution and temperature reduced to 60-70 ^{0}C. After cooling to room temperature, TOPSe was mixed with Zn salt solution. And the mixture was injected slowly through syringe in to reaction solution of CdSe-TOPO at 180-200 ^{0}C. The stirring was done for another an hour. The similar procedure was followed for work up of reaction as avobe experiment. The final product was re-dispersed in toluene.

Light emission from CdSe/ZnSe Quantum dots

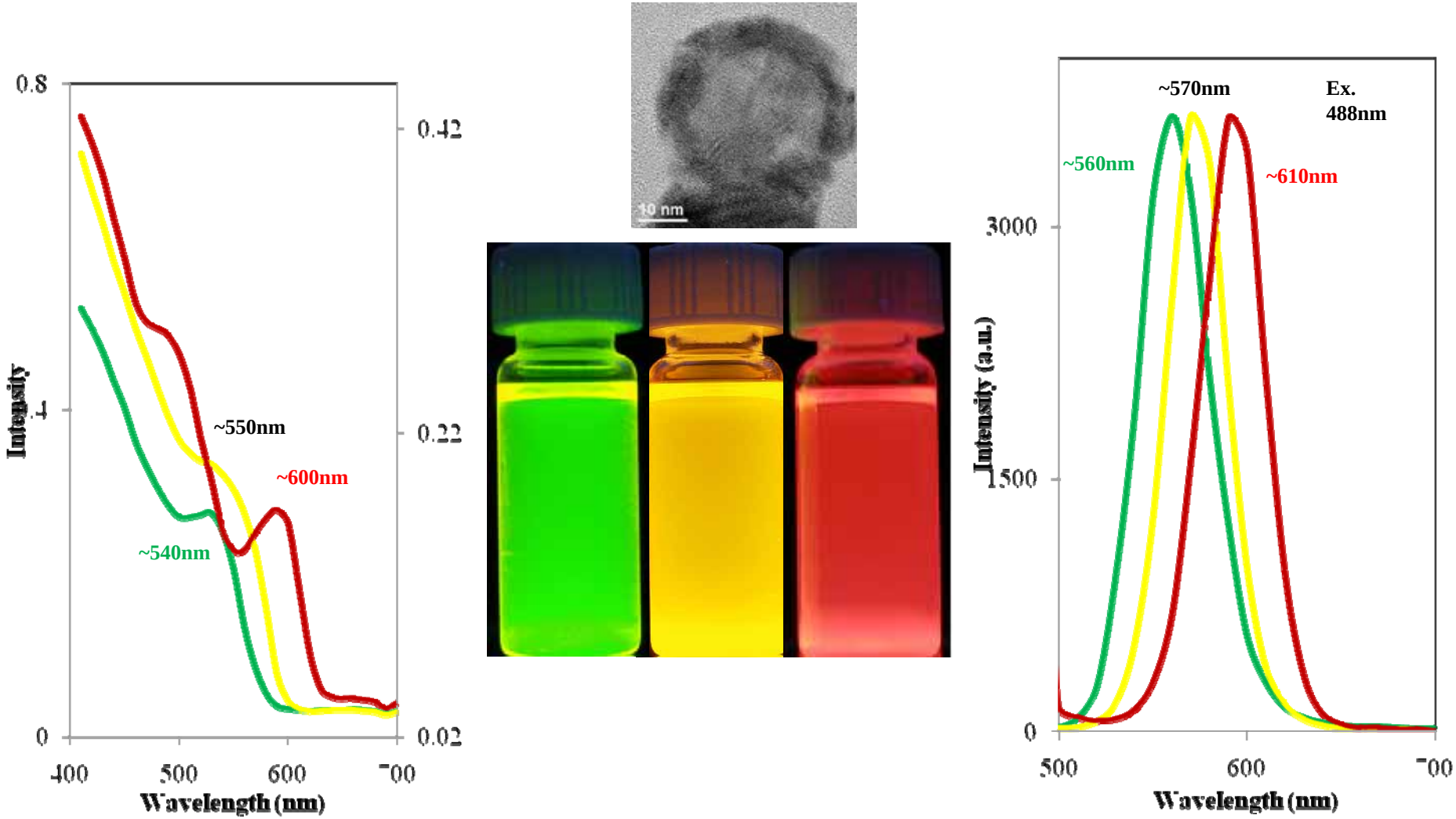

UV-Visible and PL spectra of CdSe/ZnSe re-dispersed in toluene

Carboxyl Presenting Surfaces

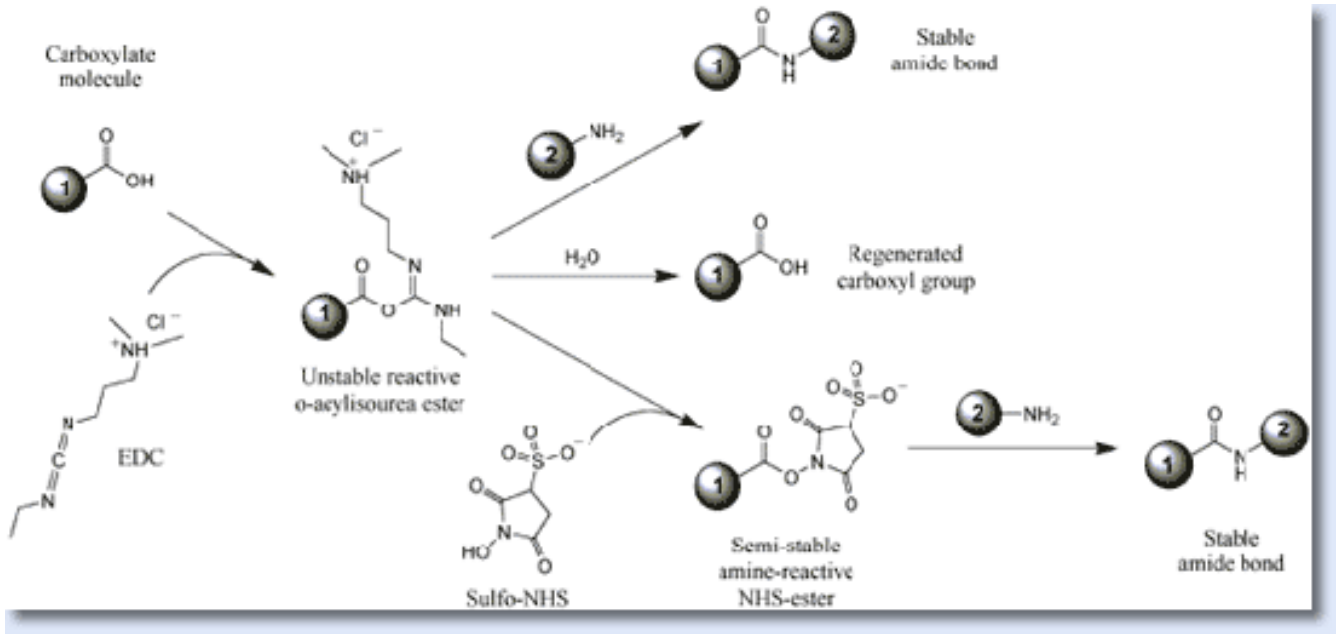

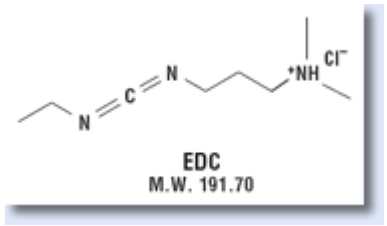

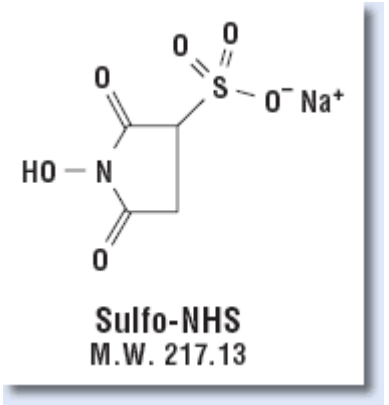

EDC (1-Ethyl-3-[3-dimethylaminopropyl]carbodiimide Hydrochloride)

Amine Presenting Surface

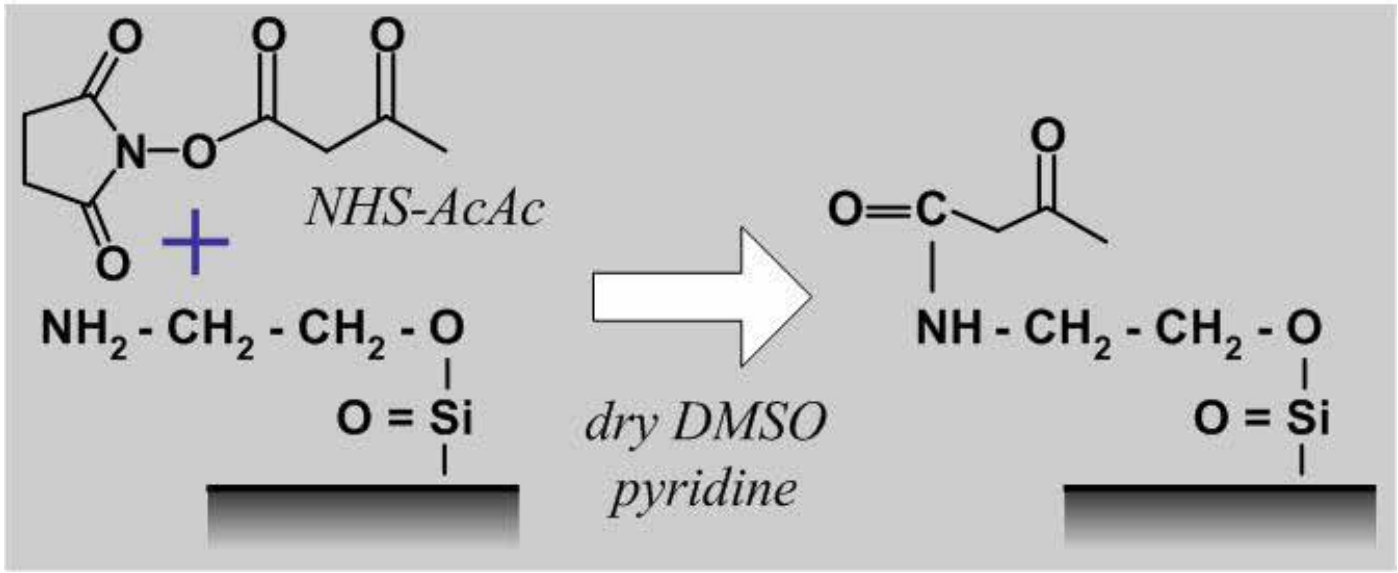

Sulfhydryl Labeling

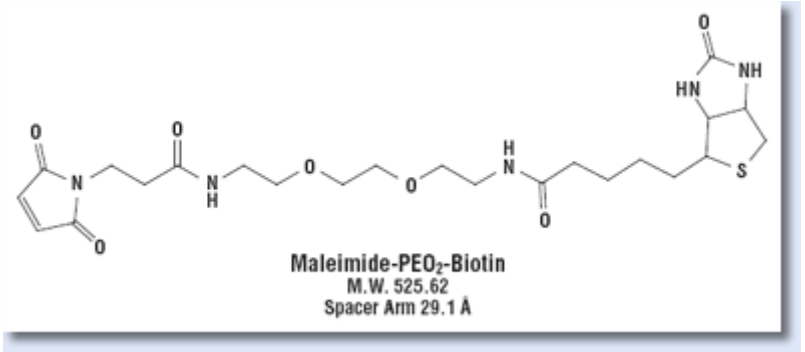

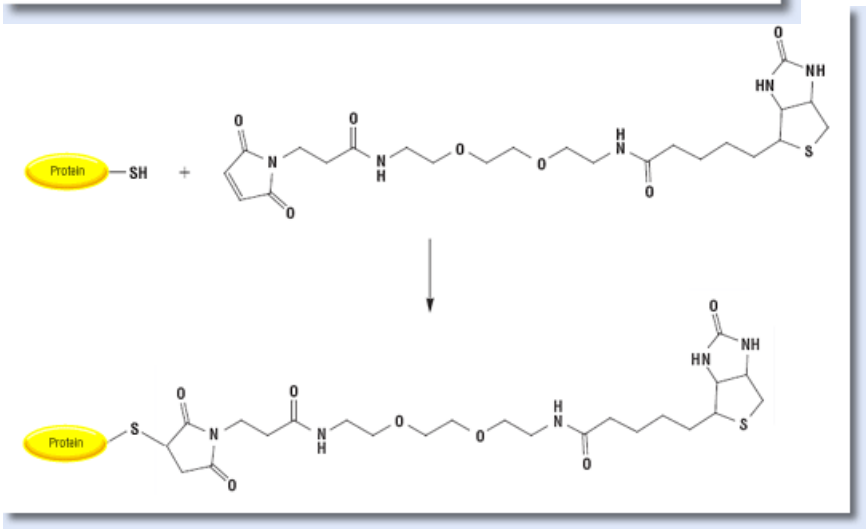

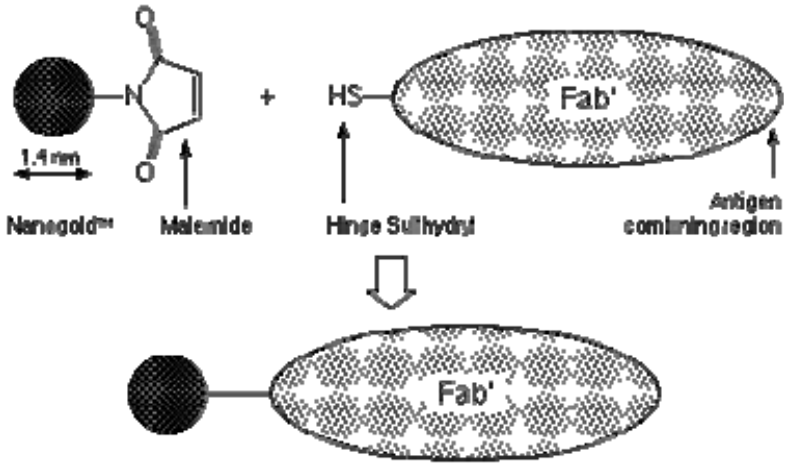

Silica Modification

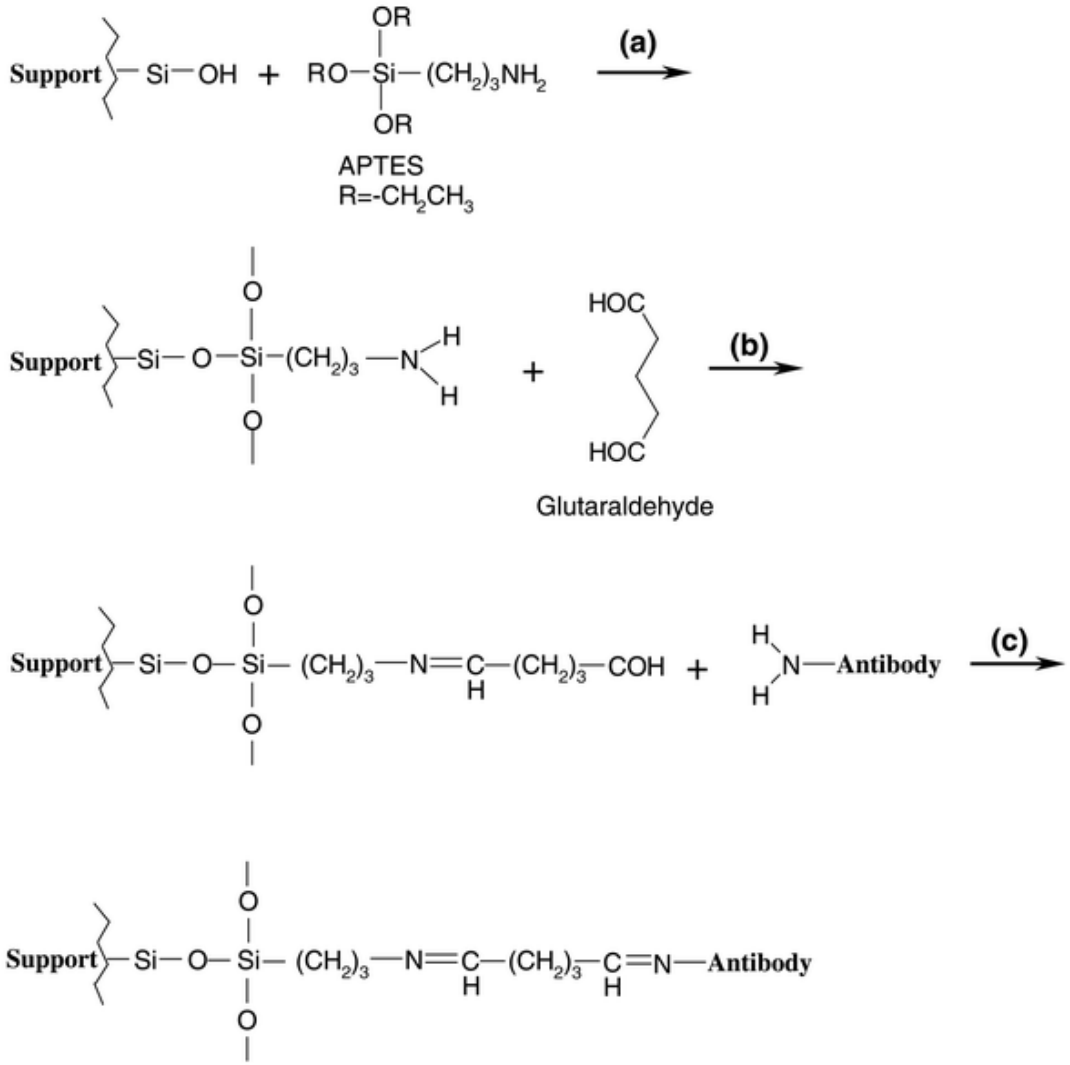

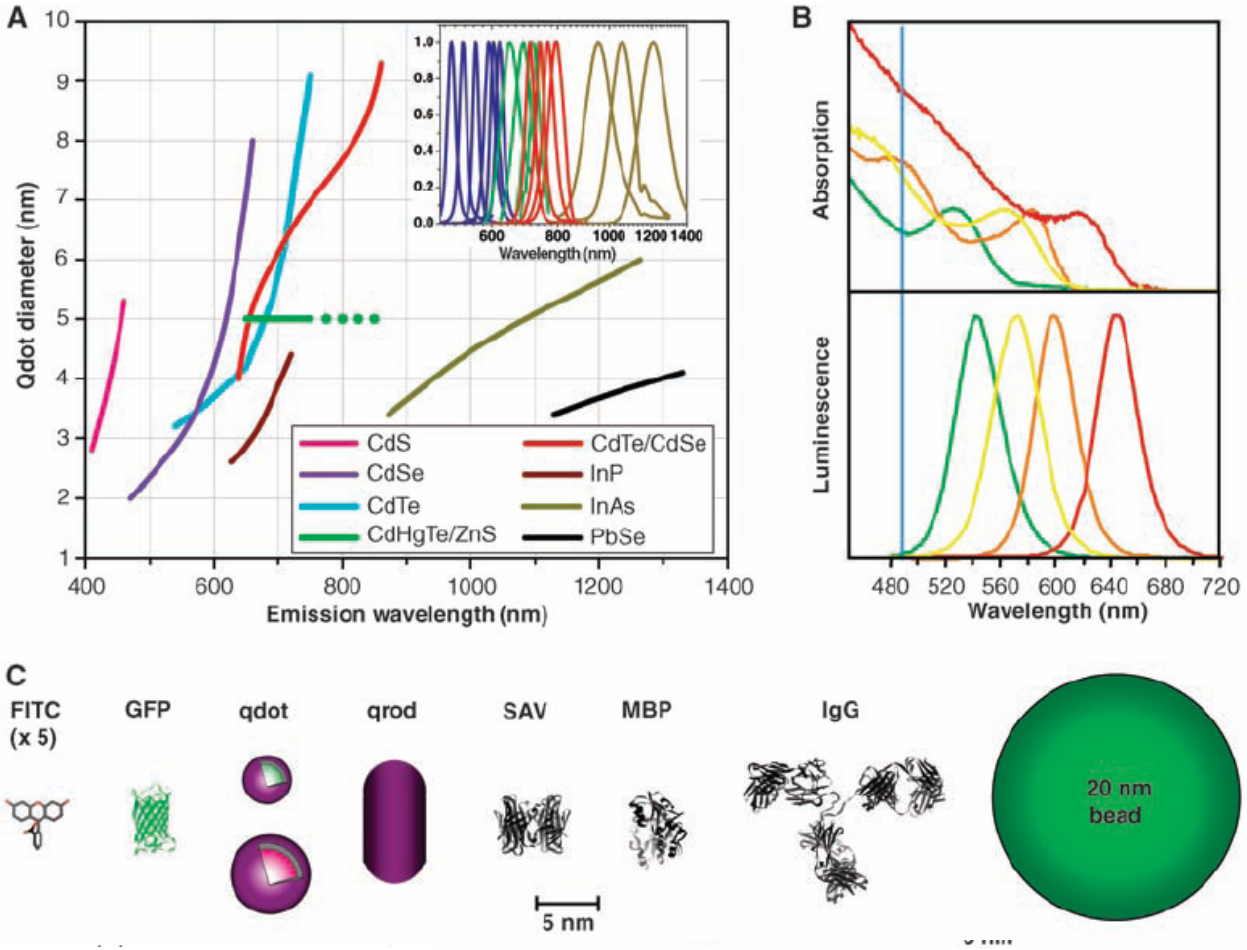

Fig. 1. (**A**) Emission maxima and sizes of quantum dots of different composition. Quantum dots can be synthesized from various types of semiconductor materials (II-VI: CdS, CdSe, CdTe…; III-V: InP, InAs…; IV-VI: PbSe…) characterized by different bulk band gap energies. The curves represent experimental data from the literature on the dependence of peak emission wavelength on qdot diameter. The range of emission wavelength is 400 to 1350 nm, with size varying from 2 to 9.5 nm (organic passivation/solubilization layer not included). All spectra are typically around 30 to 50 nm (full width at half maximum). Inset: Representative emission spectra for some materials. Data are from (*12*, *18*, *27*, *76*–*82*). Data for CdHgTe/ZnS have been extrapolated to the maximum emission wavelength obtained in our group. (**B**) Absorption (upper curves) and emission (lower curves) spectra of four CdSe/ZnS qdot samples. The blue vertical line indicates the 488-nm line of an argon-ion laser, which can be used to efficiently excite all four types of qdots simultaneously. [Adapted from (*28*)] (**C**) Size comparison of qdots and comparable objects. FITC, fluorescein isothiocyanate; GFP, green fluorescent protein; qdot, green (4 nm, top) and red (6.5 nm, bottom) CdSe/ZnS qdot; qrod, rod-shaped qdot (size from Quantum Dot Corp.'s Web site). Three proteins—streptavidin (SAV), maltose binding protein (MBP), and immunoglobulin G (IgG)—have been used for further functionalization of qdots (see text) and add to the final size of the qdot, in conjunction with the solubilization chemistry (Fig. 2).

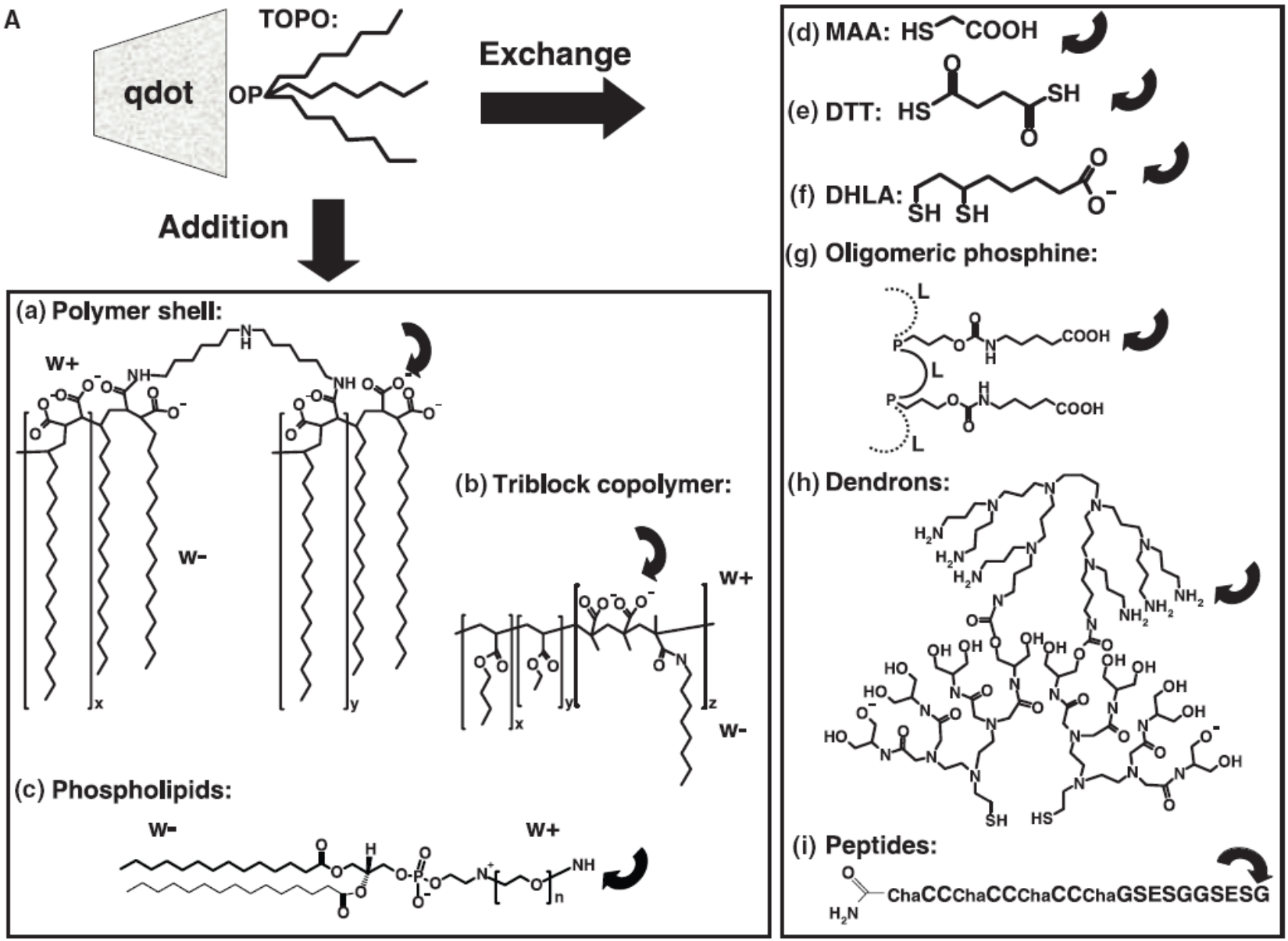
A
qdot
TOPO:
OP
Exchange
Addition
(a) Polymer shell:
W+
W-
(b) Triblock copolymer:
W+
W-
(c) Phospholipids:
W-
W+
(d) MAA: HS COOH
(e) DTT: HS SH
(f) DHLA: SH SH
(g) Oligomeric phosphine:
COOH
COOH
(h) Dendrons:
(i) Peptides:
ChaCCChaCCChaCCChaGSESGGSESG

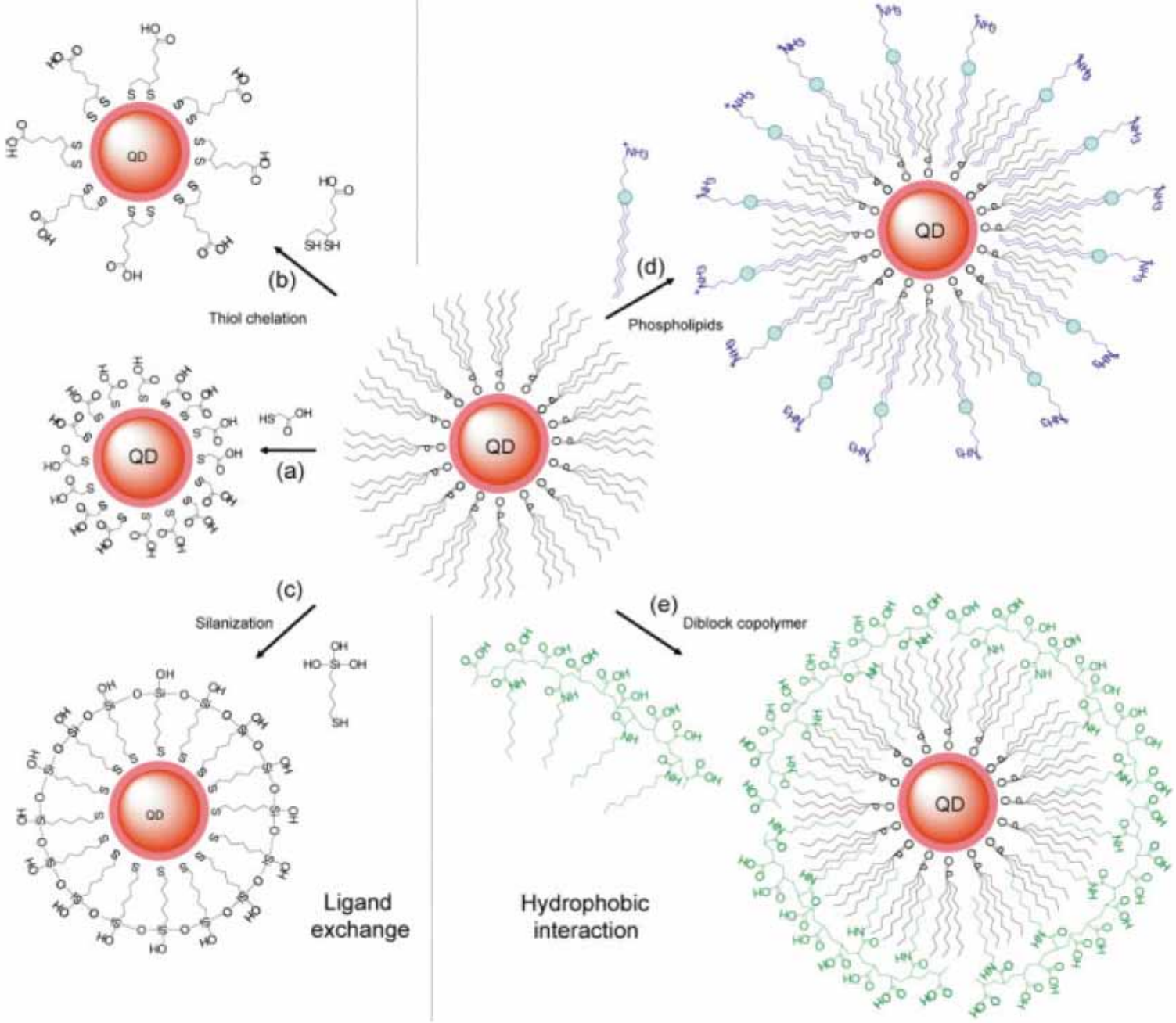
QD
(a)
(b)
Thiol chelation
(c)
Silanization
(d)
Phospholipids
(e)
Diblock copolymer
Ligand
exchange
Hydrophobic
interaction

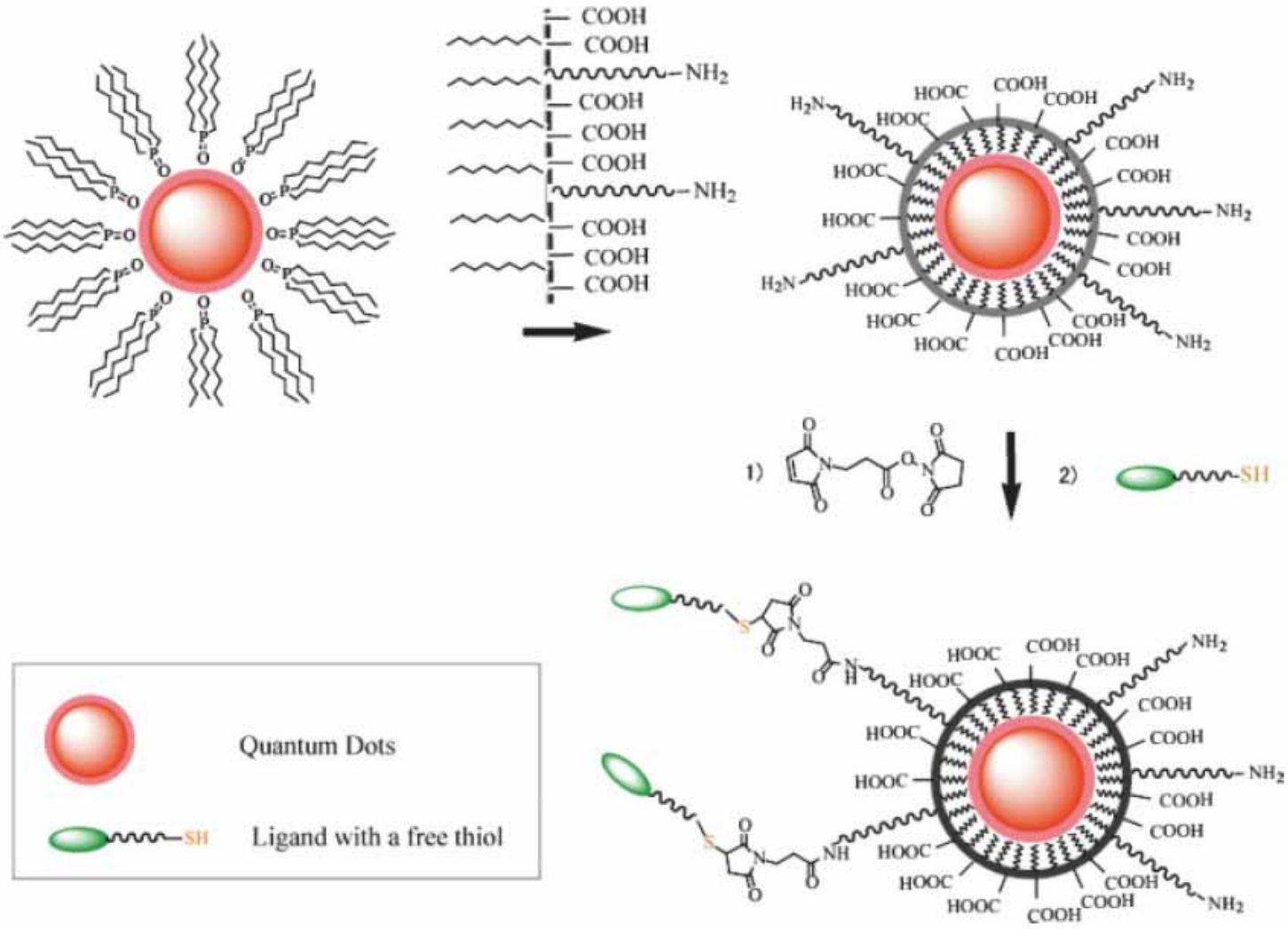

FIGURE 3 Maleimide functionalized QDs for conjugating thiol-containing ligands. TOPO stabilized QDs are coated with a primary amine functionalized tri-block amphiphilic copolymer for producing water-soluble QDs, which facilitate further conjugation to ligands with free thiols through bi-functional cross-linkers.

Cells incubated with tiopronin coated QDs

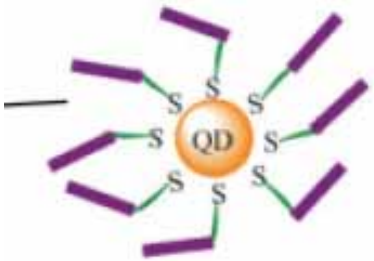

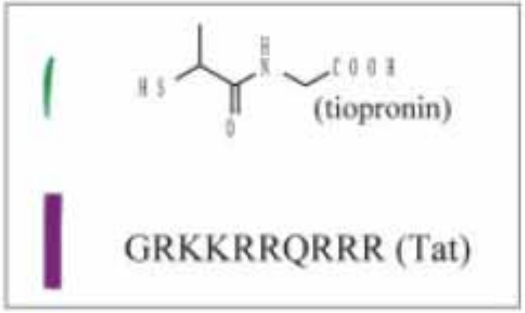

Cells incubated with Tat functionlized QDs

Scheme 1. Modular Design of Hydrophilic Ligands with Terminal Functional Groups Used in This Study

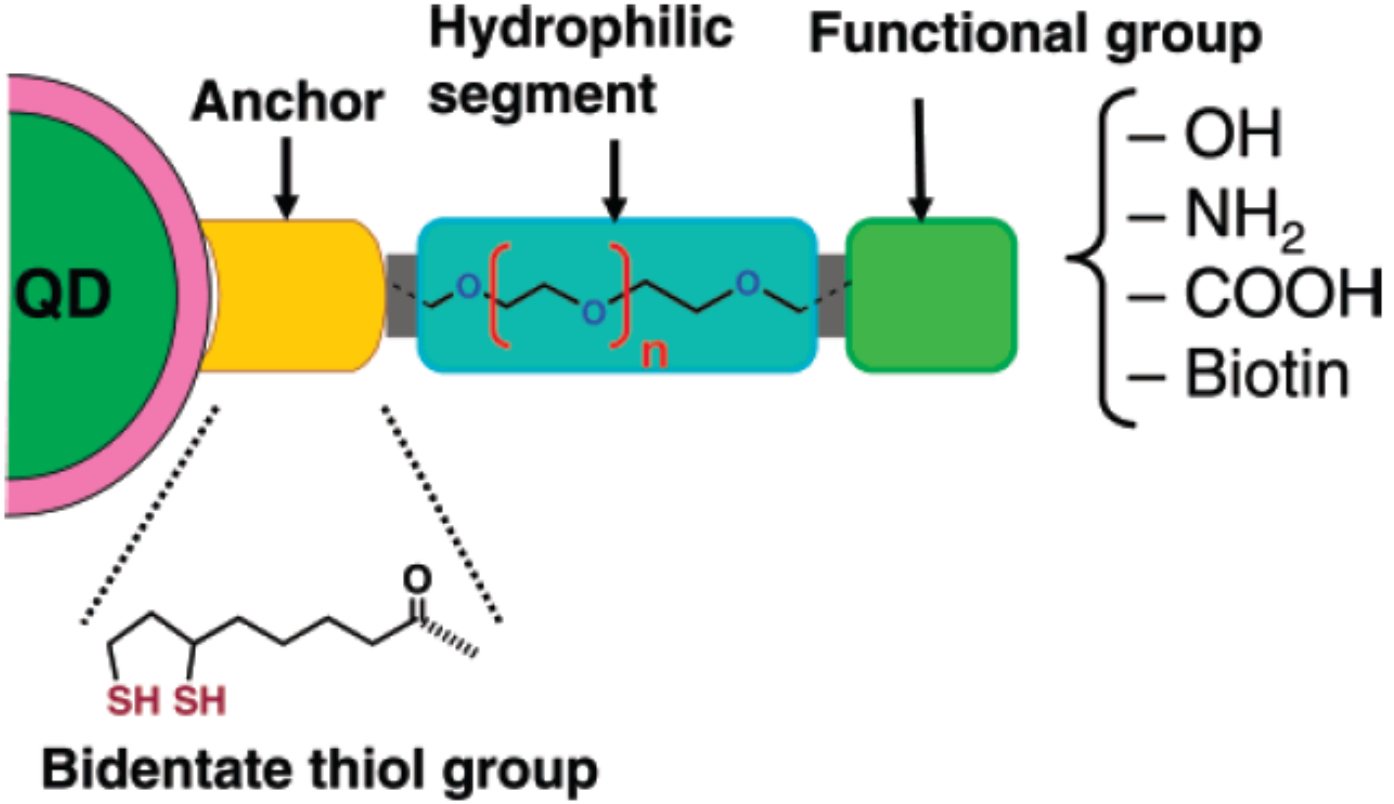

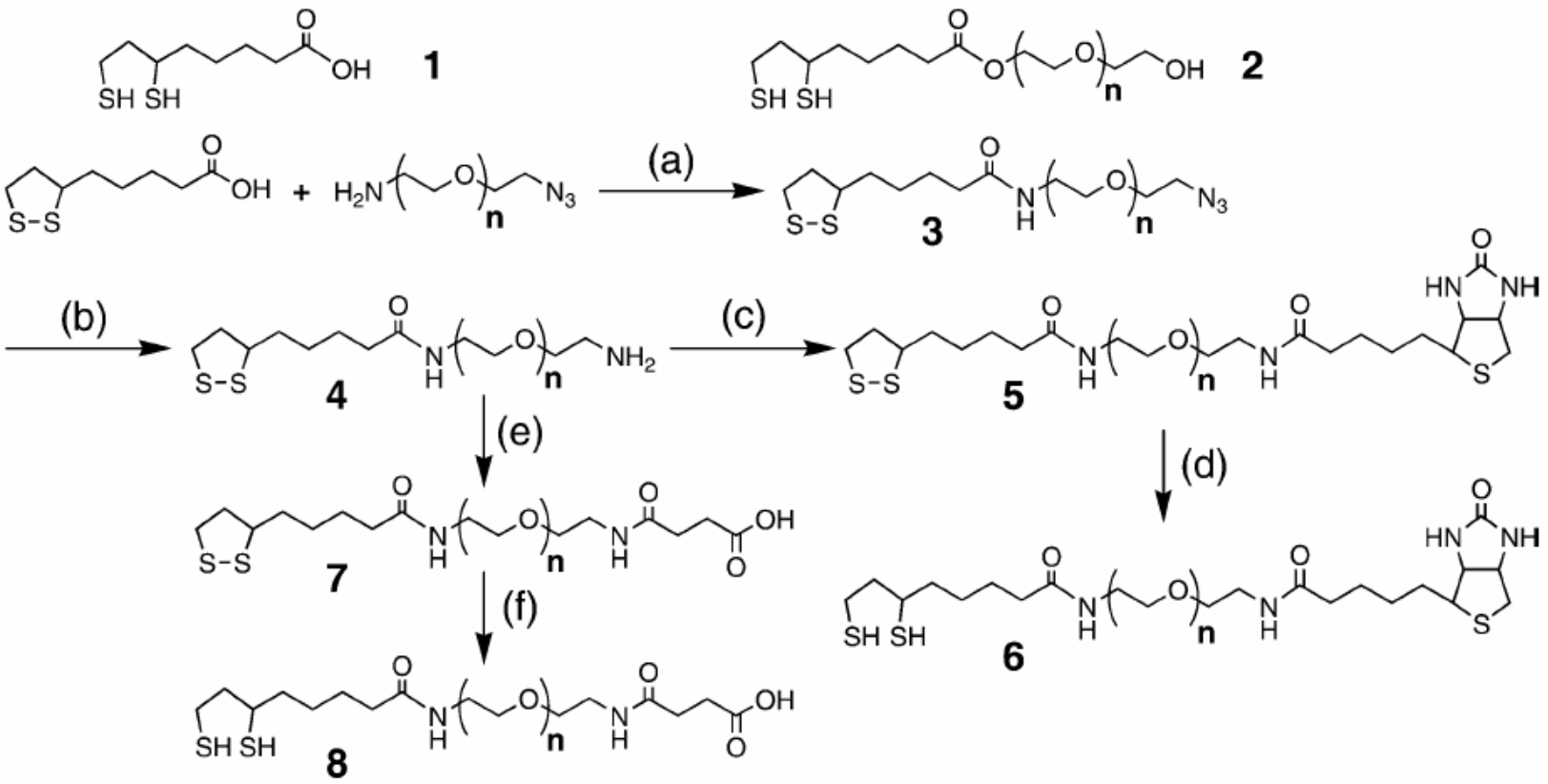

Figure 1. Chemical structures and synthetic routes of the surface ligands used in this study: (a) DCC, DMAP, CH_2Cl_2; (b) PPh_3, H_2O, THF; (c) biotin *N*-hydroxysuccinimide ester, Et_3N, DMF; (d) $NaBH_4$, EtOH, H_2O; (e) succinic anhydride, pyridine; (f) $NaBH_4$, EtOH, H_2O.

Plasmonics

Plasmonics in Biology and Plasmon-Controlled Fluorescence

Joseph R. Lakowicz

Plasmonics (2006) 1: 5–33

Chem. Rev. **2008,** *108,* 494–521

Nanostructured Plasmonic Sensors

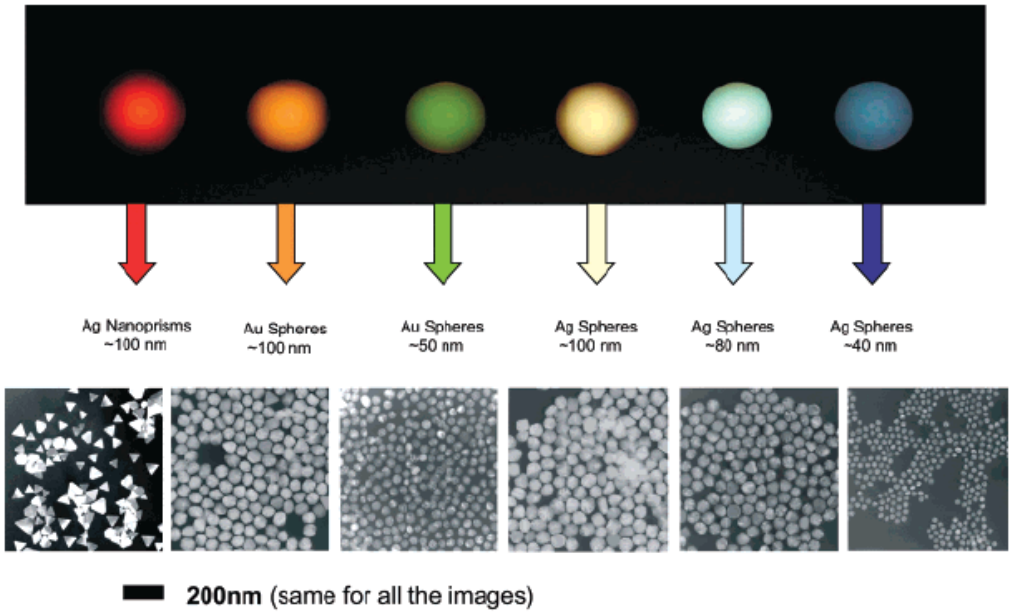

Surface Plasmon

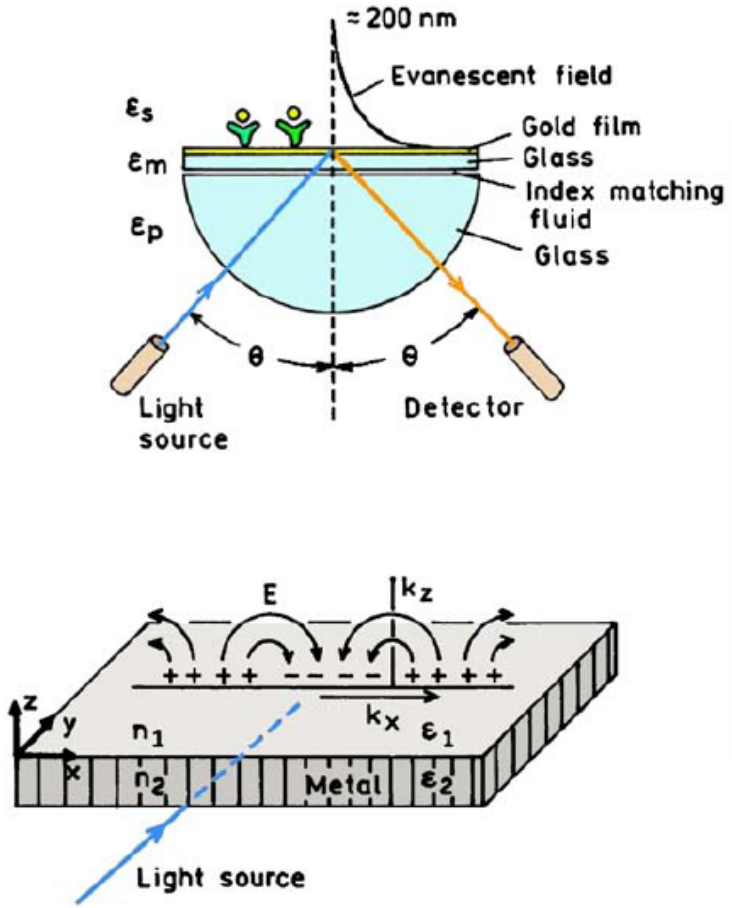

Figure 3. Schematics of an SPR experiment (top) and of the light-induced surface plasmons (bottom).

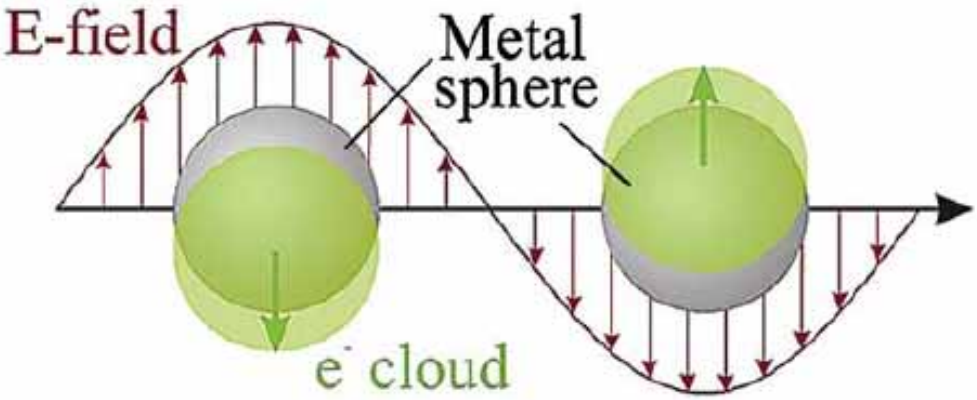

Figure 6. Schematic of plasmon oscillation for a sphere. From [39].

Drift: Drude model

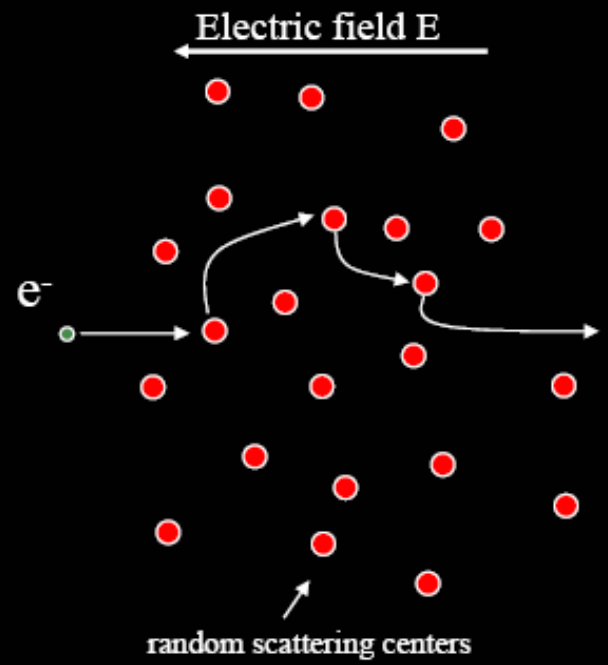

$$F = ma$$

$$eE = m\frac{\partial v}{\partial t}$$

$$v_{avg} = \underbrace{\frac{e\tau}{m}}_{\mu} E$$

$$j = nev_{avg} = \underbrace{\frac{ne^2\tau}{m}}_{\sigma} E$$

$$m\frac{\partial}{\partial t}\langle\vec{v}\rangle = q\vec{E} - \gamma\langle\vec{v}\rangle$$

$$\sigma(\omega) = \frac{\sigma_0}{1 + i\omega\tau}$$

Far-Field Optical Microscopy of Single Metal Nanoparticles

Acc. Chem. Res. **2005**, *38*, 594–601

The optical properties of metals are, to a large extent, determined by conduction electrons. The response of these free electrons follows the Drude model. They collectively react to perturbation by an external electric field. The Coulomb restoring force between the electrons and the lattice leads to harmonic oscillations with the plasma frequency $\omega_p^2 = Ne^2/(m_e\epsilon_0)$ where N is the electron density and m_e the electron mass. The damping of the oscillation is described by a phenomenological damping constant, γ. In this model, the dielectric function, $\epsilon(\omega)$, equals

$$\epsilon(\omega) = 1 - \frac{\omega_p^2}{\omega(\omega + i\gamma)}$$

For noble metals, the contribution of the bound d-electrons to the optical properties cannot be neglected.[9]

Maxwell Equations

$$\nabla \cdot \vec{H} = 0, \tag{4.}$$

$$\nabla \cdot \vec{E} = 0, \tag{5.}$$

$$\nabla \times \vec{E} + \frac{1}{c}\frac{\partial \vec{H}}{\partial t} = 0, \tag{6.}$$

$$\nabla \times \vec{H} - \frac{\varepsilon}{c}\frac{\partial \vec{E}}{\partial t} = 0, \tag{7.}$$

Surface Plasmon Polaritons (SPP)

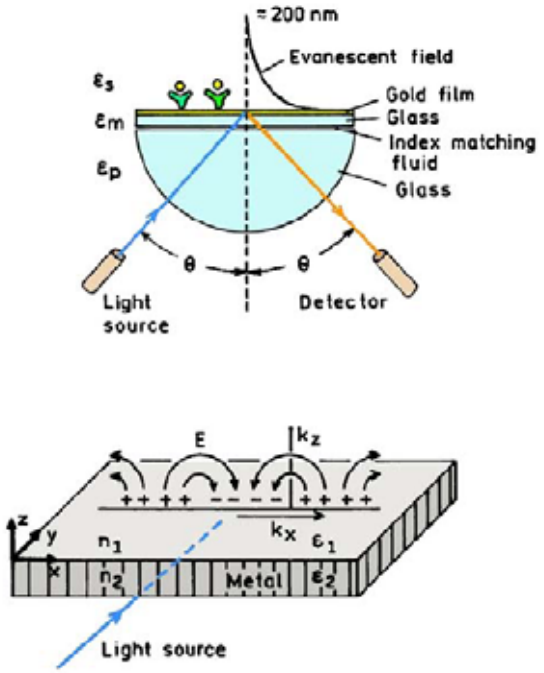

Figure 3. Schematics of an SPR experiment (top) and of the light-induced surface plasmons (bottom).

$$k_{sp} = \frac{\omega}{c}\left(\frac{\varepsilon_m \varepsilon_s}{\varepsilon_m + \varepsilon_s}\right)^{1/2} = k_0\left(\frac{\varepsilon_m \varepsilon_s}{\varepsilon_m + \varepsilon_s}\right)^{1/2} \quad (1)$$

$$\varepsilon_m = \varepsilon_r + i\varepsilon_{im} \quad (2)$$

$$k_{sp} = k_0\left(\frac{\varepsilon_r \varepsilon_s}{\varepsilon_r + \varepsilon_s}\right)^{1/2} \quad (3)$$

$$k_p = k_0 n_p \quad (4)$$

$$k_{sp} = k_x = k_0\, n_p \sin\theta_{sp} \quad (5)$$

Dielectric Constant

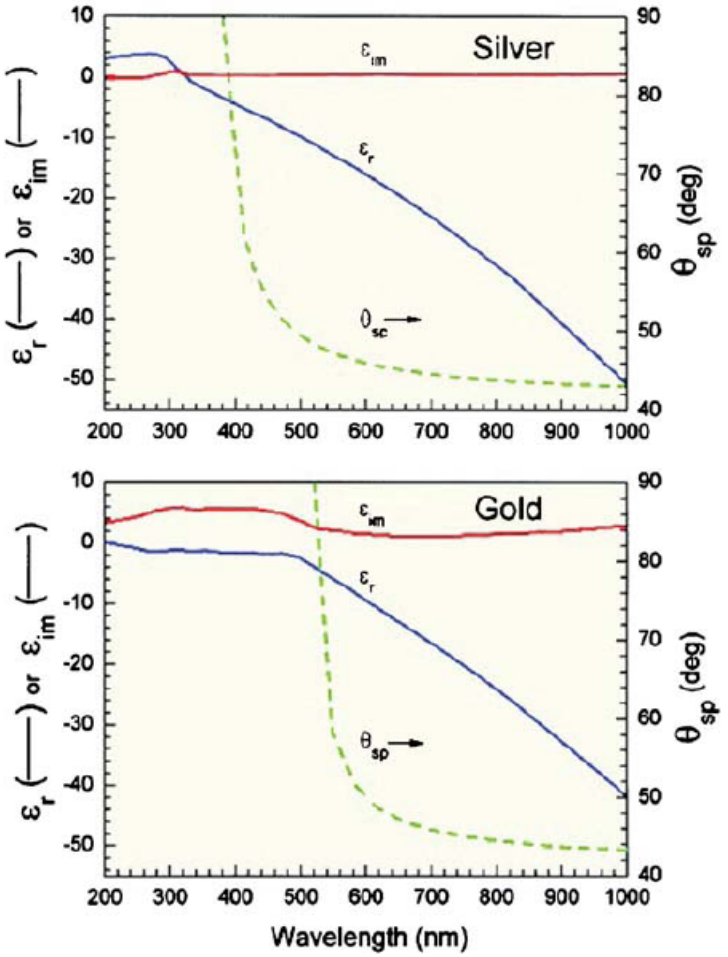

Figure 4. Dielectric constants for silver and gold.

$$\epsilon(\lambda) = \epsilon_r(\lambda) + i\epsilon_i(\lambda)$$

$$\epsilon = m^2 \text{ and } m = n + ik$$

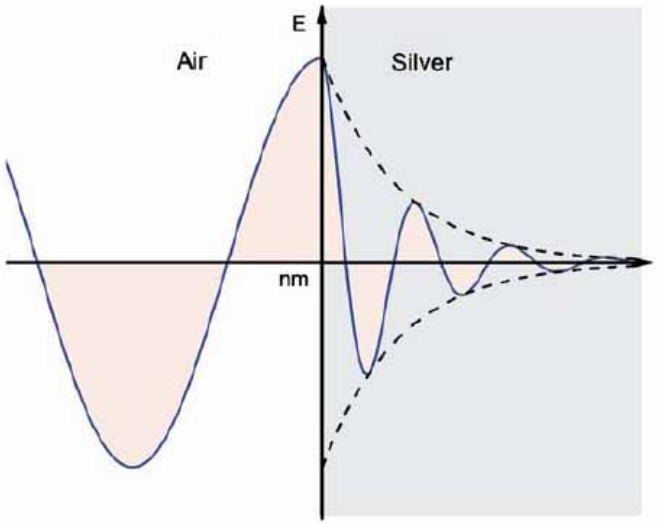

Figure 5. Schematic of attenuation of 600 nm light on a metal surface.

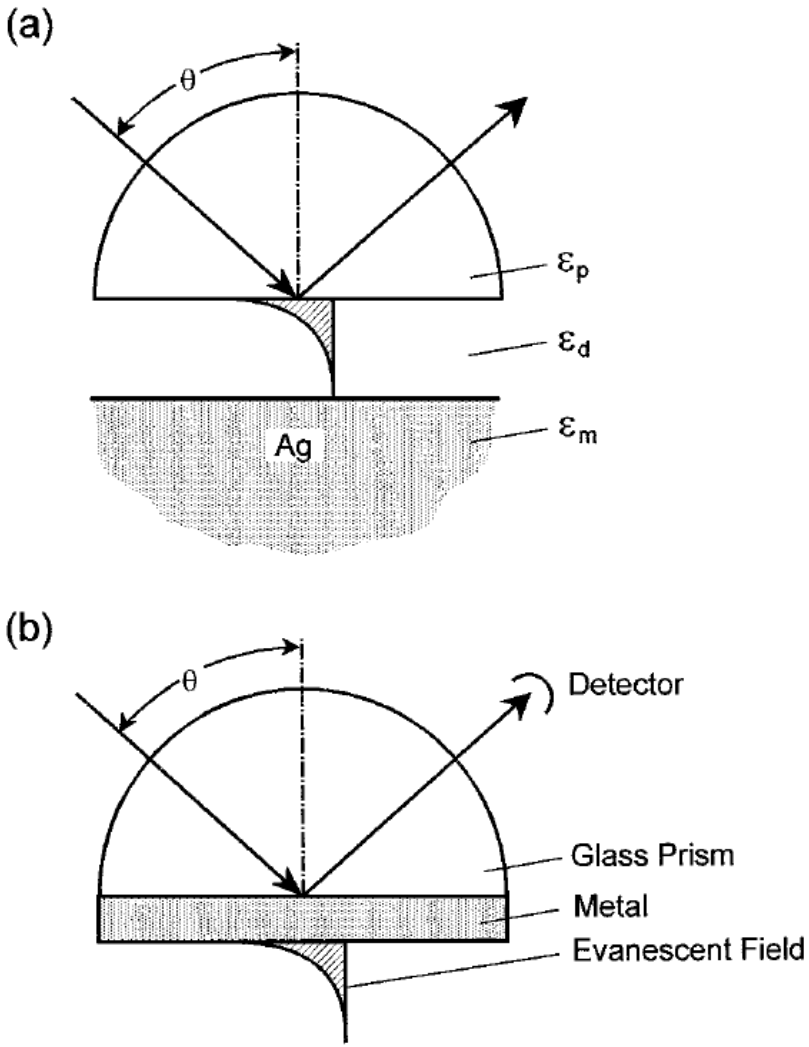

Figure 4 (*a*) The Otto configuration is based on the total internal reflection of a plane wave incident at an angle θ at the base of a prism. The evanescent tail of this inhomogeneous wave can excite PSP states at an Ag-dielectric interface, provided the coupling gap is sufficiently narrow. (*b*) Attenuated total internal reflection (ATR) construct for PSP excitation in the Kretschmann geometry. A thin metal film ($d \sim 50$ nm) is evaporated onto the base of the prism and acts as a resonator driven by the photon field incident at an angle θ.

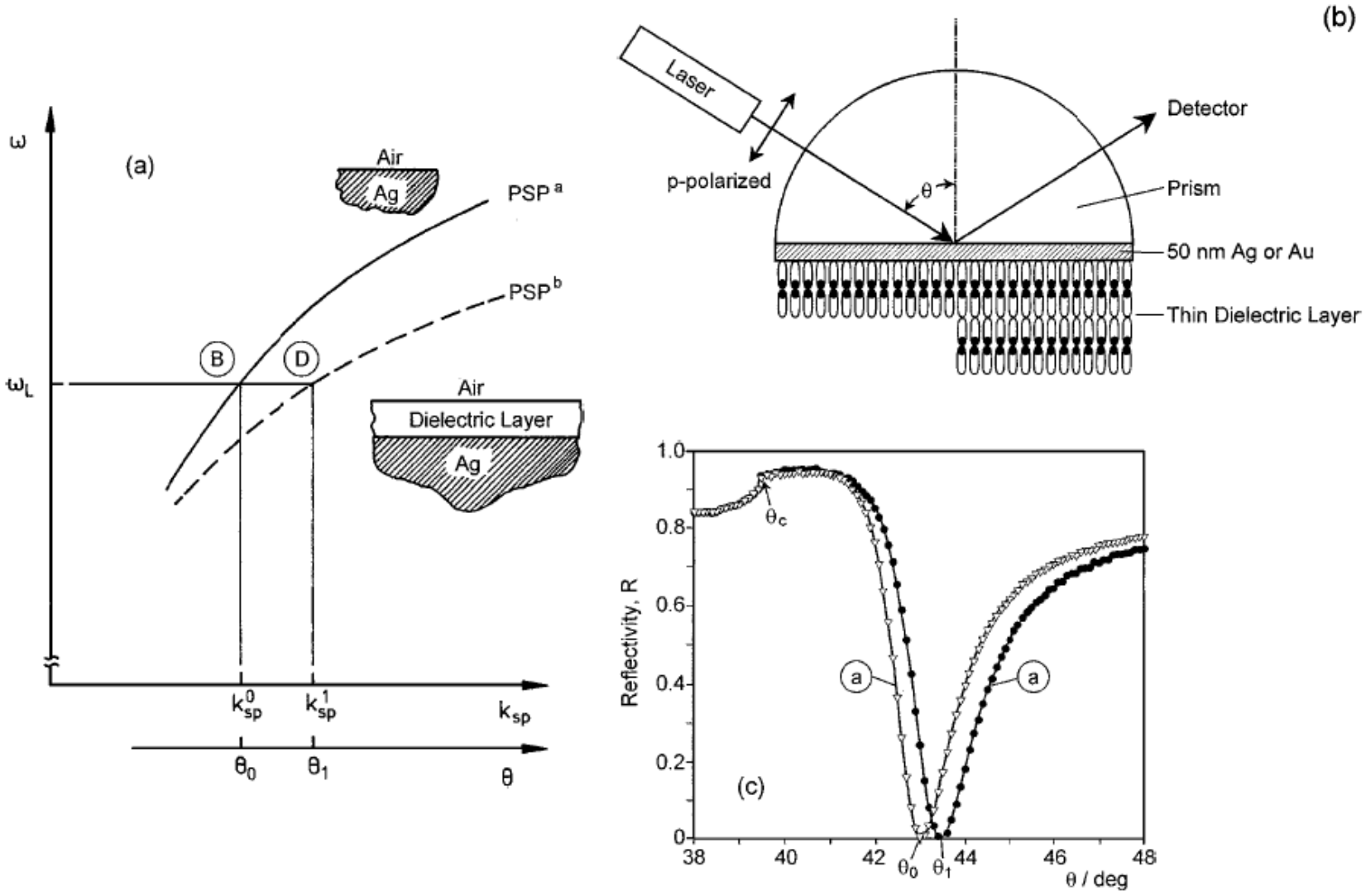

after self-assembling a monomolecular layer of HS-$(CH_2)_{21}$-OH. The symbols are experimental data points; the full curves are Fresnel fits with $\varepsilon_{BK7} = 2.29$, $\tilde{\varepsilon}_{Au} = -12.45 + i \cdot 1.3$, $d_{Au} = 46.9$ nm, $\varepsilon_{layer} = 2.1025$, $d_{layer} = 2.65$ nm. Data were taken at $\lambda = 633$ nm in air.

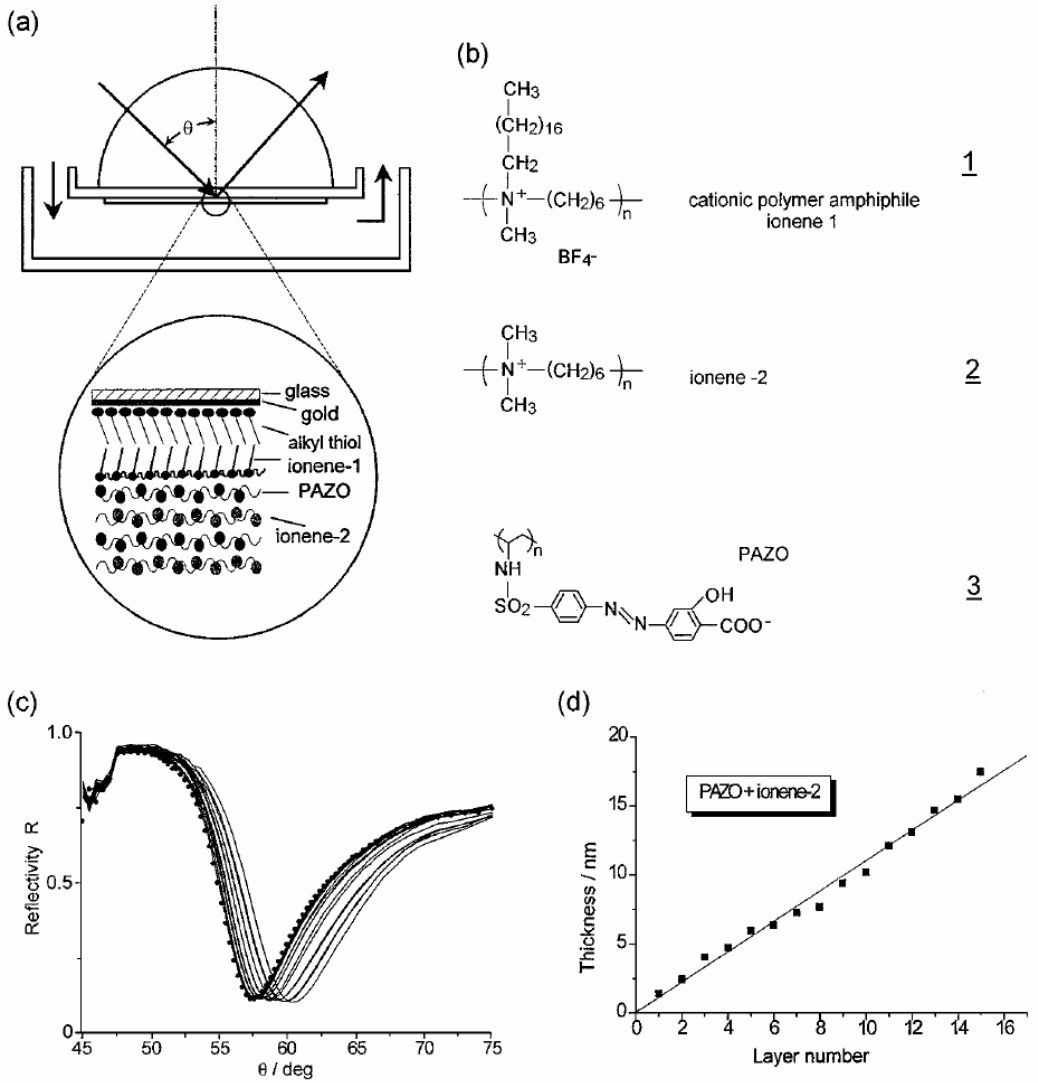

Figure 14 (*a*) Experimental construct for on-line surface plasmon optical observation of the alternating deposition of cationic and anionic polymers from solution to an Au substrate precoated by an alkyl thiol and an ionene-1 monolayer [refer to (*b*)]. The build-up architecture is given in the enlargement. (*b*) Structural formulas of the employed materials. (*c*) Series of ATR scans taken after each polyelectrolyte monolayer deposition. (*d*) Thickness increase as obtained from the ATR scans given in (*c*).

Nanoparticle Enhancement

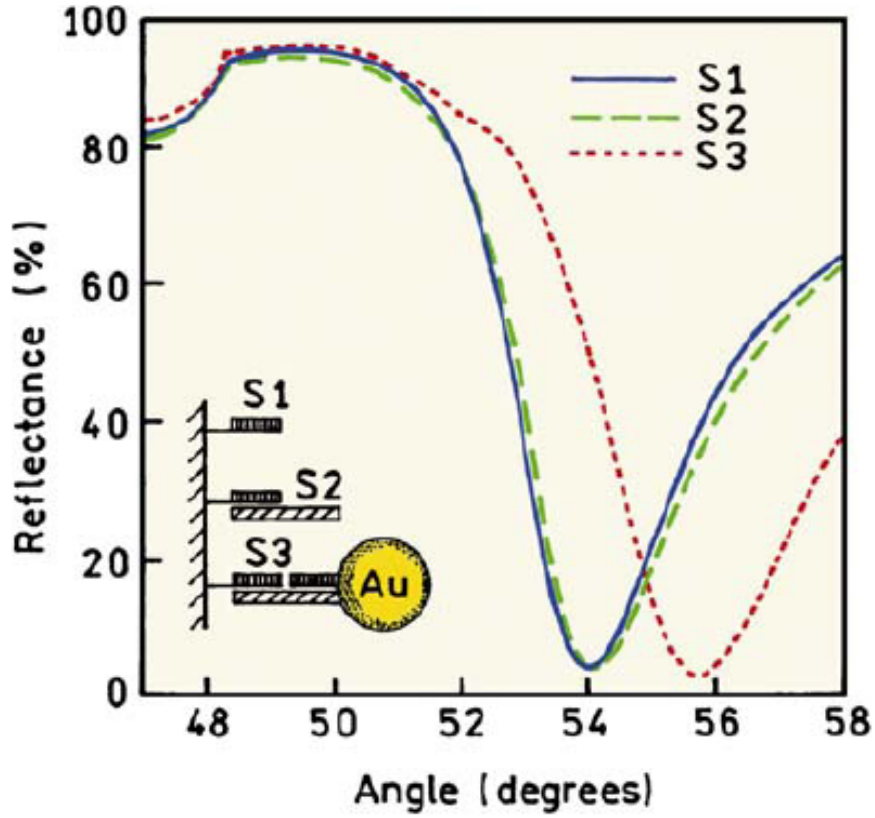

Figure 12. SPR measurements of DNA hybridization without (S2) and with Au particle amplification (S3). Revised from [51].

Localized Surface Plasmon

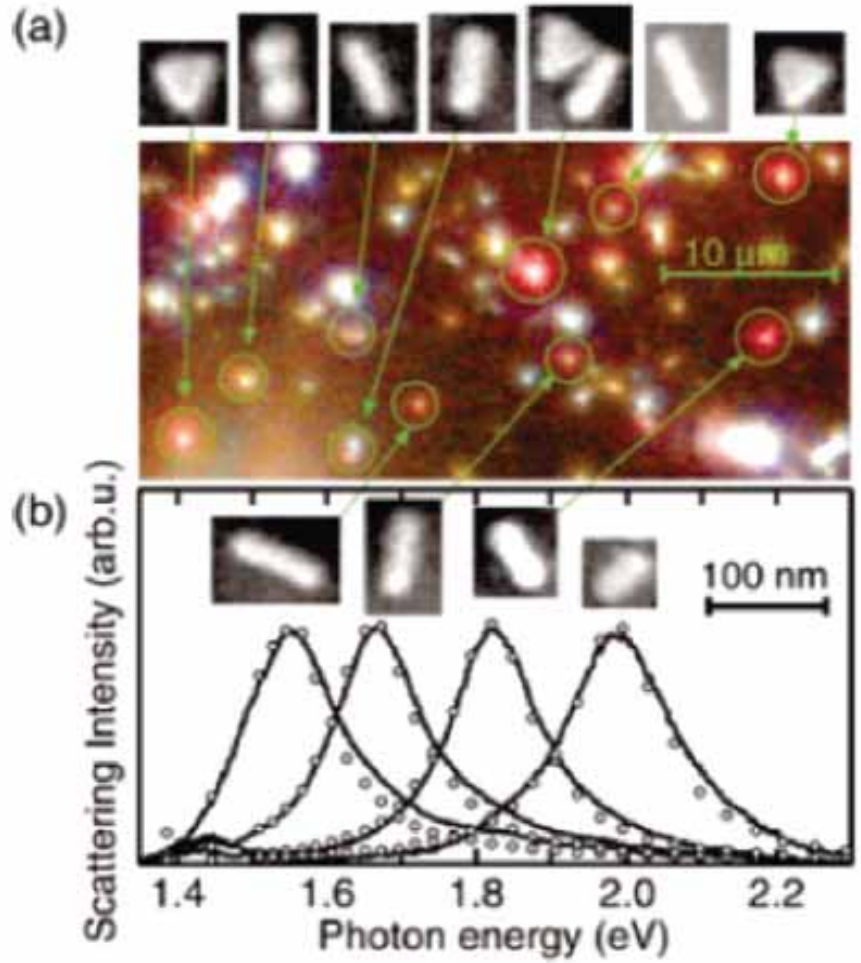

Figure 2. (a) Dark-field microscopy image and corresponding SEM images and (b) light scattering spectra of Au nanocrystals of different shapes. Reprinted with permission from ref 54. Copyright 2003 American Institute of Physics.

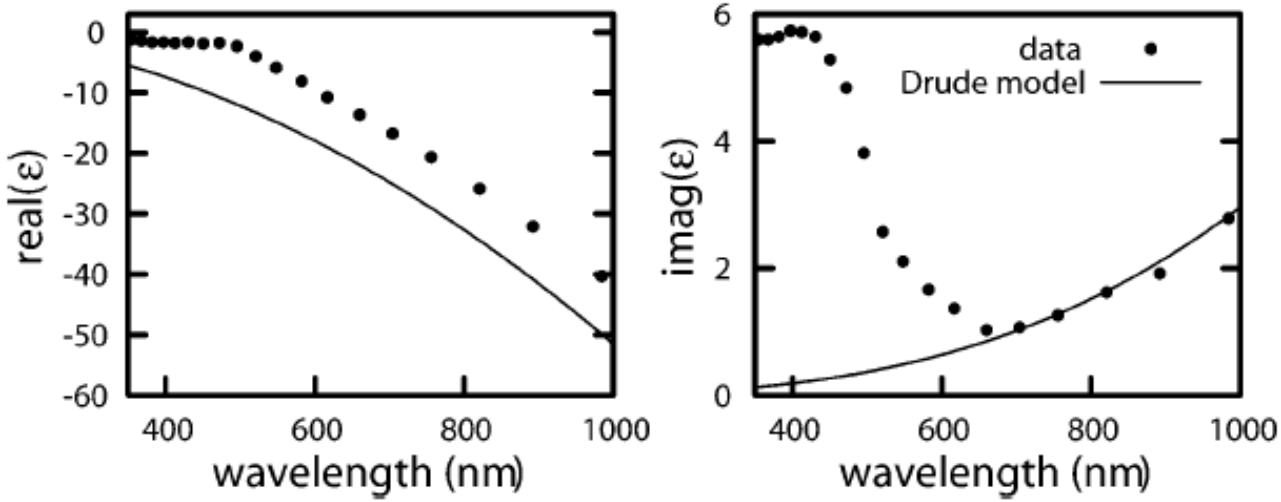

FIGURE 1. Dielectric function of gold[8] compared with the free electron model of Drude. The deviations are due to the interband contribution.

$$\sigma_{\text{ext}} = \sigma_{\text{abs}} + \sigma_{\text{sca}}.$$

$$m^2 = \frac{\epsilon_{\text{metal}}}{\epsilon_{\text{medium}}} \qquad -2$$

Mie's theory

$$\sigma_{\text{ext}} = 2\frac{2\pi}{k^2}x^3\ \text{Im}\left(\frac{m^2-1}{m^2+2}\right)$$

$$\sigma_{\text{sca}} = \frac{4}{3}\frac{2\pi}{k^2}x^6\left|\frac{m^2-1}{m^2+2}\right|^2$$

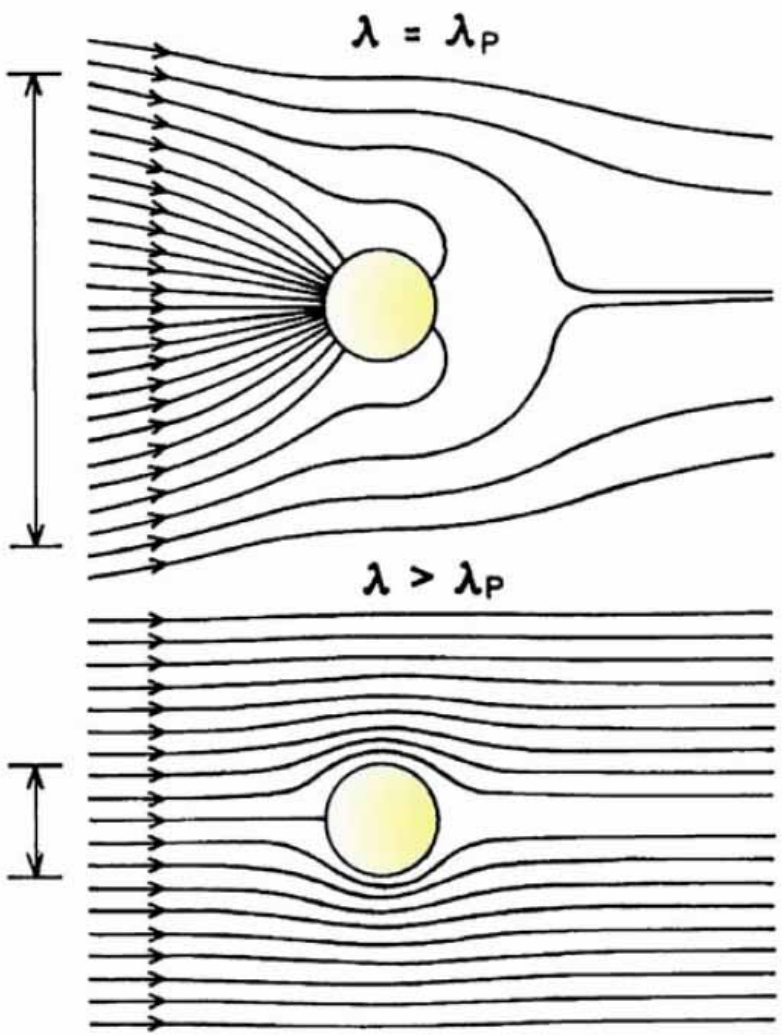

Figure 7. Poynting vector or energy flow (lines) around a subwavelength metallic colloid illuminated at the plasmon wavelength (top) and at a wavelength longer than the plasmon wavelength (bottom). The vertical lines on the left indicate the diameter of the cross sections for absorption. This diagram does not show the energy flow due to scattered light. From [40].

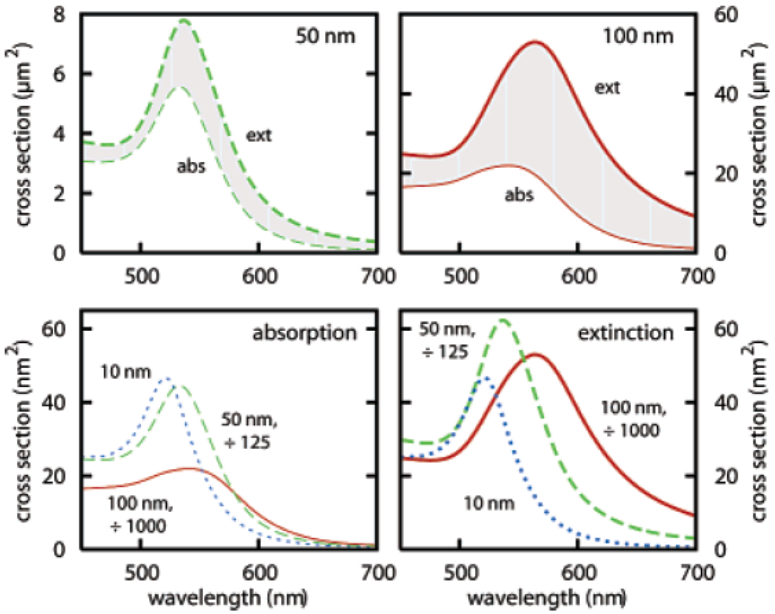

FIGURE 2. Extinction (thick lines) and absorption (thin lines) spectra of gold particles with a diameter of 10 nm (blue, dotted), 50 nm (green, dashed), and 100 nm (red, solid) plotted in different combinations of the same curves. The surrounding medium is water ($n = 1.3$). In the top panels, with increasing colloid size the additional scattering contribution to the extinction becomes more important; the gap between absorption and scattering spectra gets larger. In the bottom panels to compare colloids of different sizes the spectra are scaled with d^3 to the 10-nm particle. Both absorption and scattering spectra show a red shift and broadening of the plasmon resonance with particle size.

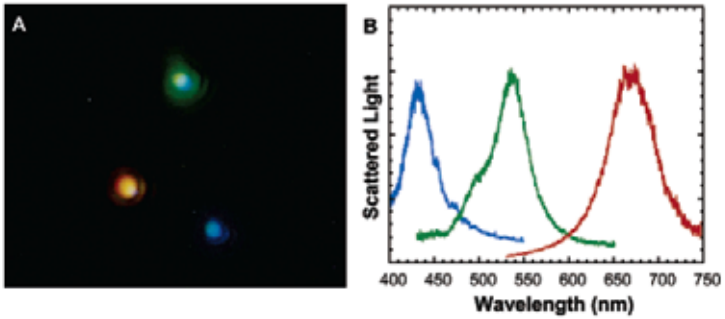

FIGURE 3. Dark-field image of silver particles of different sizes leading to different colors in the scattered white light.[15] The spot size is about 400 nm, and the height of the image is about 9 μm. The corresponding spectra are shown in the right panel. Reprinted with permission from ref 15. Copyright 2000 National Academy of Sciences, U.S.A.

Plasmonic Sensors

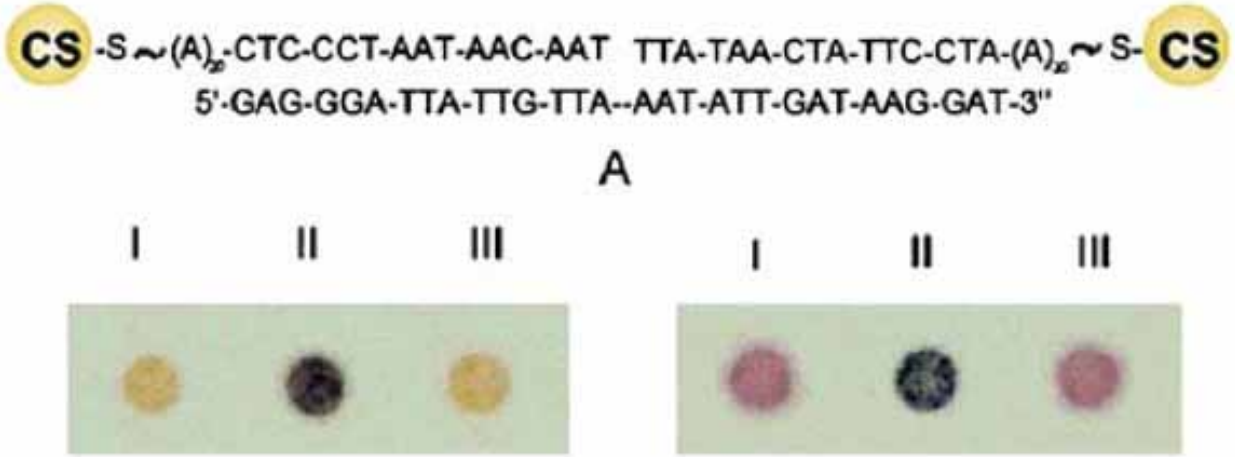

Figure 8. Top, structure of metal particle-labeled DNA with a complementary oligomer. Bottom, photographs of the labeled DNA without target (I), with target (II), and with target at $T > T_m$. On the left are Ag/Au core shell particles. On the right are Au particles. From [43].

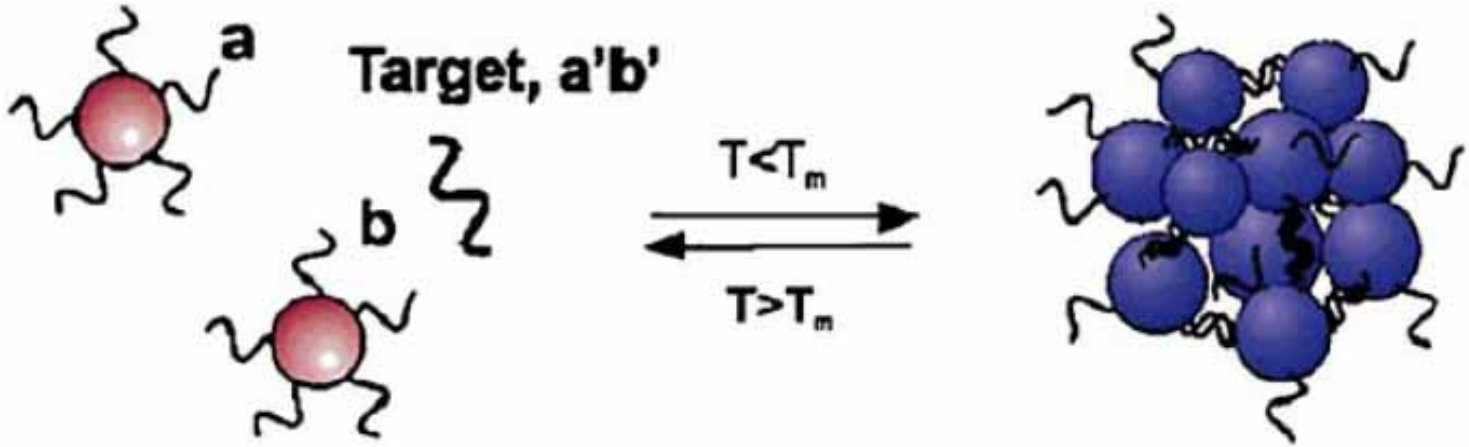
a
Target, a'b'
b
T<T$_m$
T>T$_m$

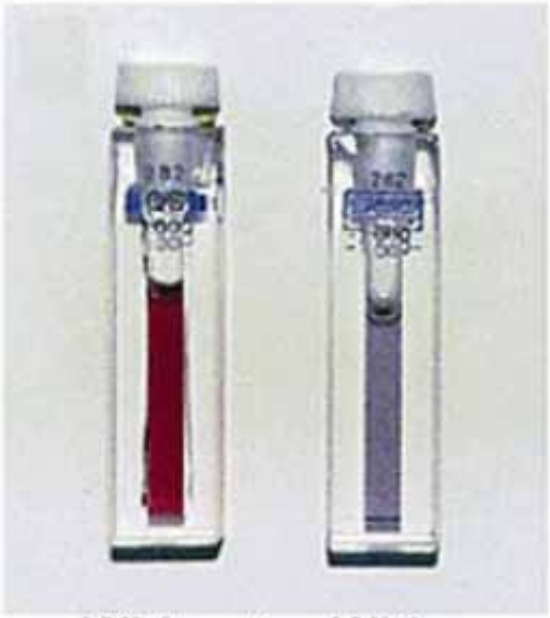
Without target
With target

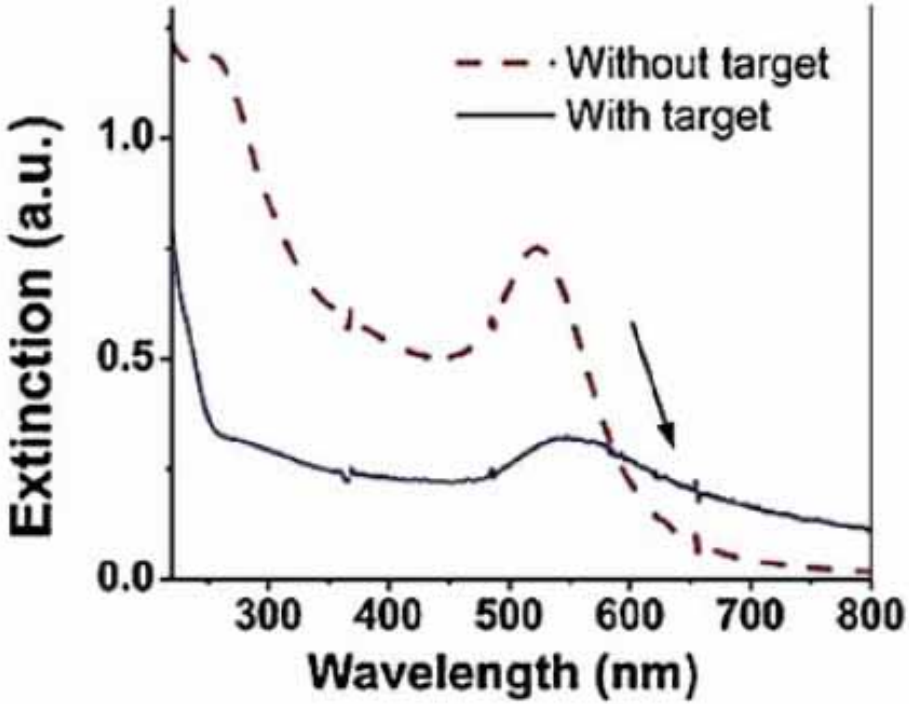
Without target
With target
Extinction (a.u.)
1.0
0.5
0.0
300
400
500
600
700
800
Wavelength (nm)

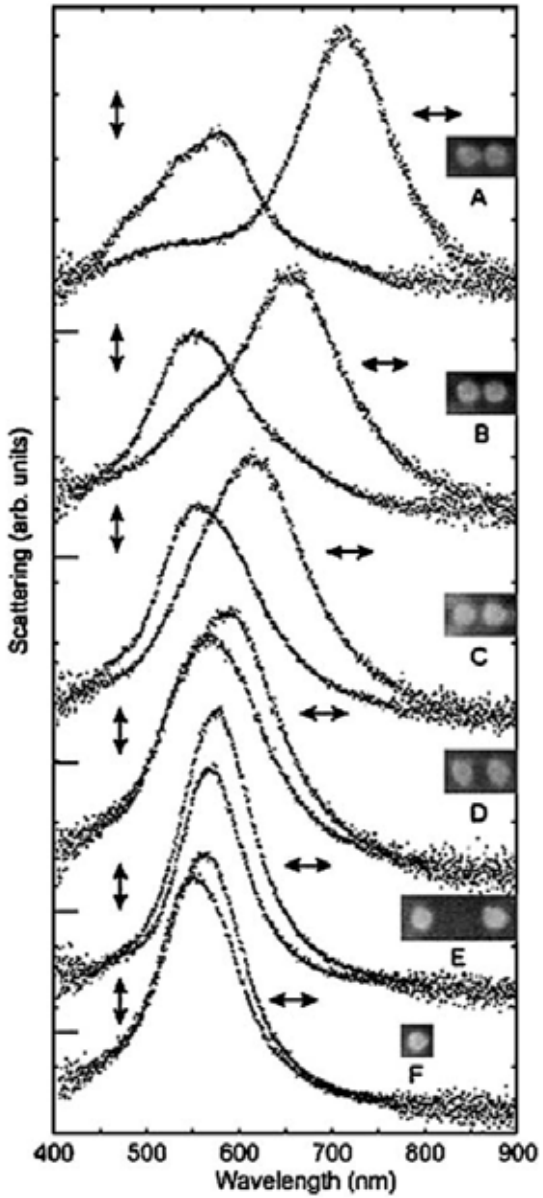

Figure 17. Dark-field scattering spectra and scanning electron micrography of isolated disk-shaped particle pairs. The arrows indicate the polarization of the incident light. The gaps between the particles are approximately 10, 15, 25, 50, and 250 nm, for A through E. F is an isolated particle. The disks are about 95 nm in diameter and 25 nm high. From [72].

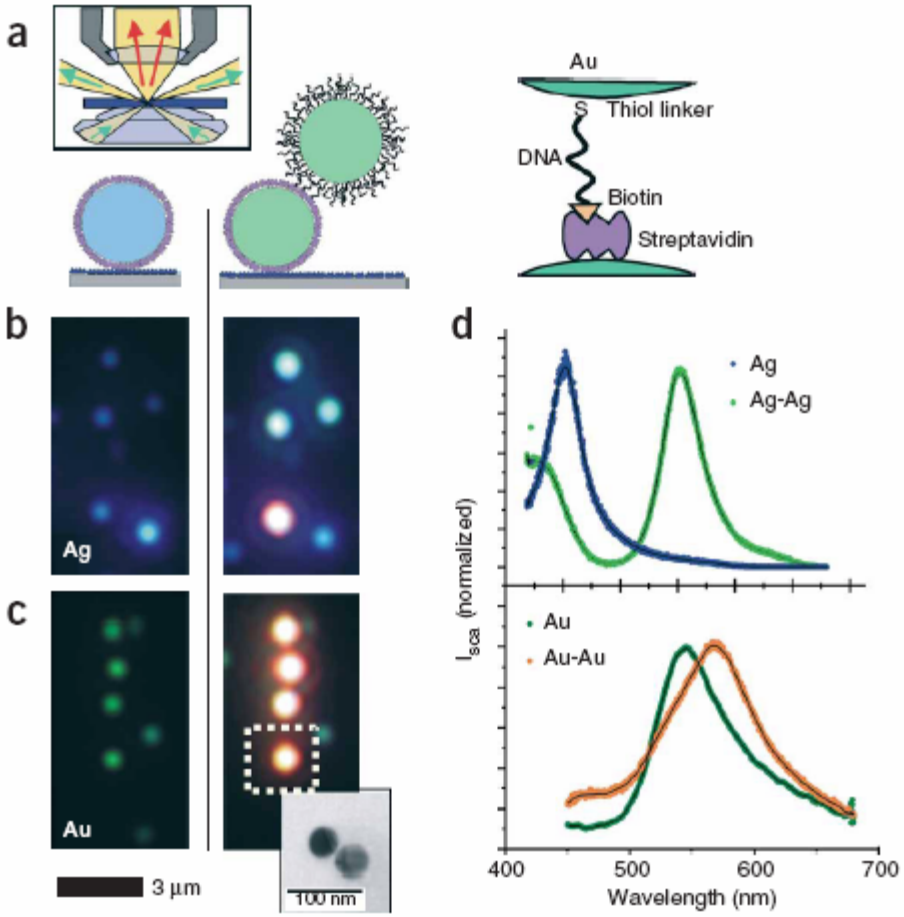

Figure 1 Color effect on directed assembly of DNA-functionalized gold and silver nanoparticles. (**a**) First, nanoparticles functionalized with streptavidin are attached to the glass surface coated with BSA-biotin (left). Then, a second particle is attached to the first particle (center), again via biotin-streptavidin binding (right). The biotin on the second particle is covalently linked to the 3′ end of a 33 base pair long ssDNA strand bound to the particle via a thiol group at the 5′ end. Inset: principle of transmission darkfield microscopy. (**b**) Single silver particles appear blue (left) and particle pairs blue-green (right). The orange dot in the bottom comes from an aggregate of more than two particles. (**c**) Single gold particles appear green (left), gold particle pairs, orange (right). Inset: representative transmission electron microscopy image of a particle pair to show that each colored dot comes from light scatted from two closely lying particles, which cannot be separated optically. (**d**) Representative scattering spectra of single particles and particle pairs for silver (top) and gold (bottom). Silver particles show a larger spectral shift (102 nm) than gold particles (23 nm), stronger light scattering and a smaller plasmon line width. Gold, however, is chemically more stable and is more easily conjugated to biomolecules via –SH, –NH2 or –CN functional groups.

should increase the electrostatic repulsion between the charged gold particles[26]. Consistent with this model, a blue-shift in the spectrum of individual nanoparticle pairs occurred when we decreased the salt concentration of our buffer (normally 0.1 M NaCl) to 0.005 M NaCl (Fig. 2a). When we restored the ionic concentration to the original

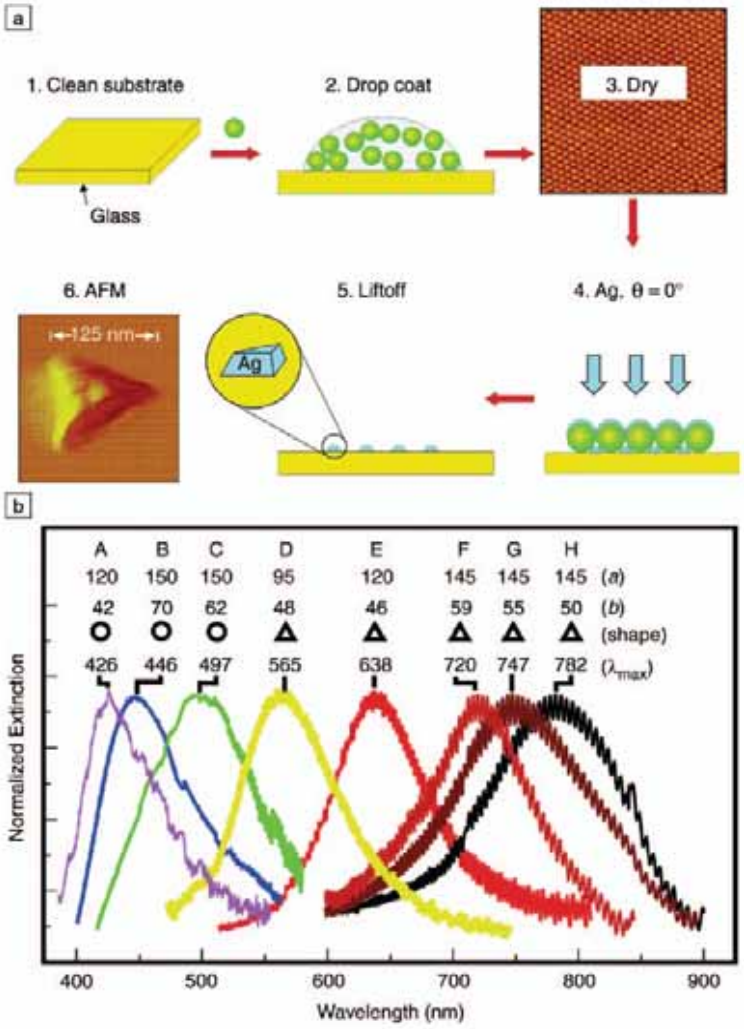

Figure 1. (a) Schematic representation of the nanosphere lithography (NSL) fabrication process. The AFM image in step 3 is 5 μm × 5 μm. (b) Size- and shape-tunable localized surface plasmon resonance spectra of various Ag nanoparticles (labeled A–H) fabricated by NSL. The wavelength of maximum extinction, λ_{max}, is changed by varying the in-plane width a and out-of-plane height b of the nanoparticles.

The simplest theoretical approach available for modeling the optical properties of nanoparticles is classical electrodynamics (i.e., solving Maxwell's equations with the metal dielectric constant taken from bulk measurements). For spherical particles, this leads to the following (Mie theory) expression for the extinction coefficient $E(\lambda)$ in the long-wavelength limit:[23]

$$E(\lambda) = \frac{24\pi N_A a^3 \varepsilon_m^{3/2}}{\lambda \ln(10)} \times \left[\frac{\varepsilon_i}{(\varepsilon_r + 2\varepsilon_m)^2 + \varepsilon_i^2} \right]. \quad (1)$$

Here, N_A is the areal density of the nanoparticles, a is the radius of the metallic nanosphere, ε_m is the dielectric constant of the medium surrounding the nanosphere (assumed to be a positive, real number), λ is the wavelength, and ε_r and ε_i are the real and imaginary parts of the metal dielectric function. This formula predicts a resonant peak when $\varepsilon_r = -2\varepsilon_m$, which for silver and gold occurs in the visible portion of the spectrum. In addition, any change in the dielectric constant of the medium (e.g., when molecules adsorb on the particle) leads to a change in the resonance wavelength.

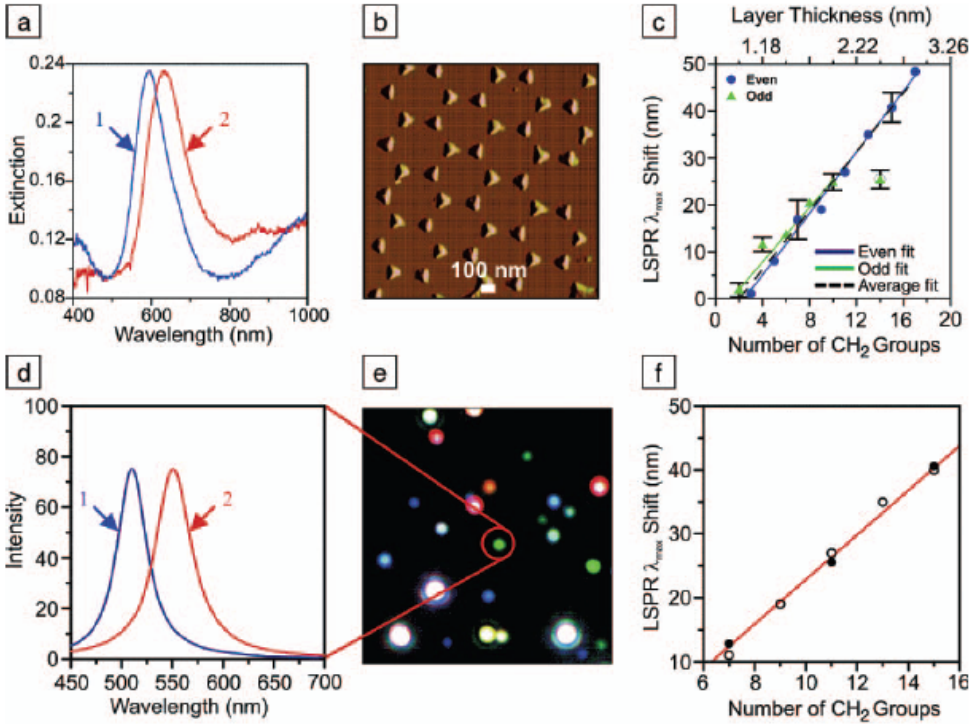

Figure 3. (top row) Localized surface plasmon resonance (LSPR) spectroscopy of a Ag nanoparticle array fabricated by nanosphere lithography in a N_2 environment: (a) Extinction spectrum of the array (curve 1) before chemical modification, wavelength of extinction maximum λ_{max} = 594.8 nm, and (curve 2) after modification with 1 mM hexadecanethiol, λ_{max} = 634.8 nm. (b) Tapping-mode atomic force microscopy (AFM) image of the array in (a); nanosphere diameter D = 390 nm, deposited mass thickness d_m = 50 nm; Ag on mica substrate; scan area, 3.0 μm^2. After solvent annealing, nanoparticle in-plane width is 100 nm and out-of-plane height is 51 nm. (c) Alkanethiol chain length dependence on the LSPR spectral peak shifts for the array. Even and odd carbon chain lengths are depicted with different symbols to emphasize the difference in the terminal bond orientation with respect to the substrate, which leads to different observed trends for the two cases. (bottom row) LSPR spectroscopy of single Ag nanoparticles produced by chemical synthesis: (d) scattering spectrum of a single Ag nanoparticle (curve 1) before chemical modification, λ_{max} = 510.2 nm, and (curve 2) after modification with 1 mM hexadecanethiol, λ_{max} = 550.9 nm. The circled nanoparticle in (e) produced the signal for these curves. (e) Dark-field resonant Rayleigh scattering image of a random array of chemically synthesized Ag nanoparticles (image dimensions, 130 $\mu m \times 130 \mu m$). (f) Alkanethiol chain length dependence on the LSPR spectral peak shifts for a single Ag nanoparticle. The open circles represent an overlay of the array data from (c). The solid circles are single nanoparticle measurements.

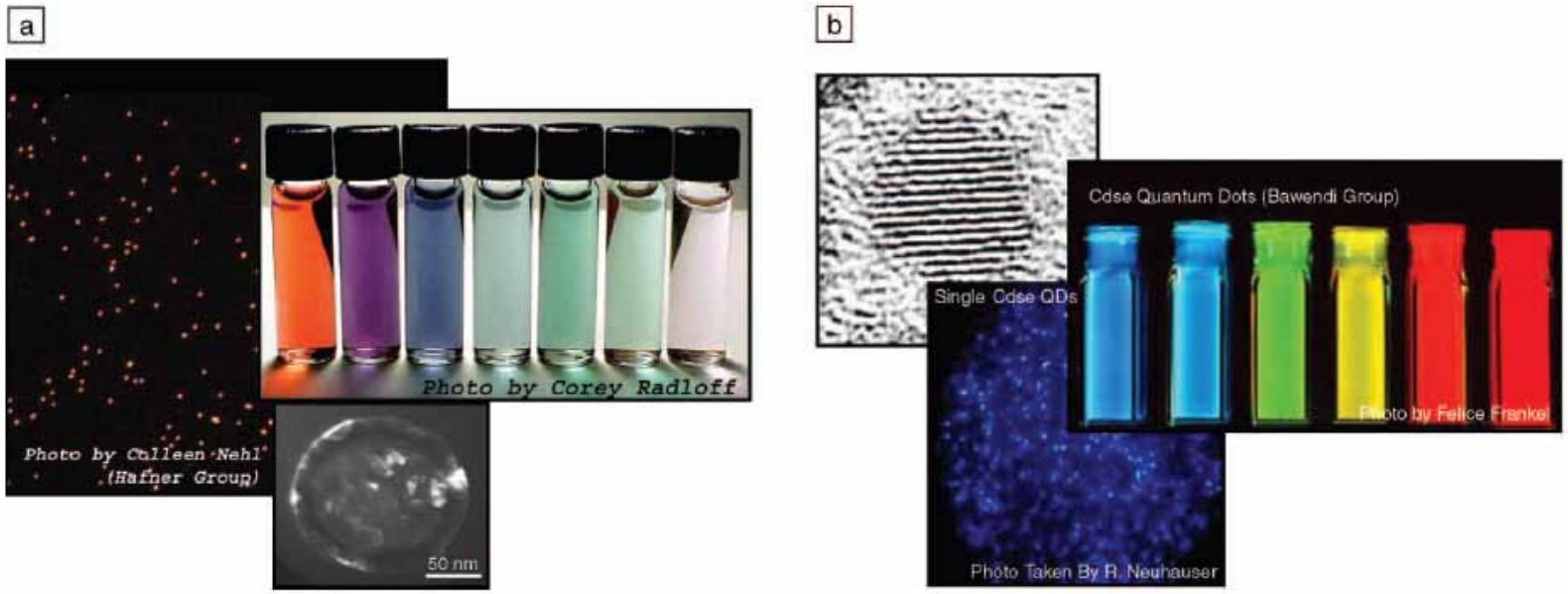

Figure 3. (a) Nanoshells are tunable plasmonic nanoparticles. Micrographs show a field of many nanoshells (large micrograph) and one nanoshell (small micrograph). Vials show nanoshells in solution. (b) Semiconductor quantum dots are tunable excitonic nanoparticles (courtesy of the Bawendi group). A field of quantum dots is displayed in the bottom image; an individual quantum dot is shown in the upper-left micrograph. Vials of quantum dots are also shown. Comparing single nanoshells to single quantum dots, nanoshells typically have a 10^6 larger absorption cross section, nominally five times the physical cross section of the nanoparticle.

Probing Single Molecules and Single Nanoparticles by Surface-Enhanced Raman Scattering

SCIENCE • VOL. 275 • 21 FEBRUARY 1997

Shuming Nie* and Steven R. Emory

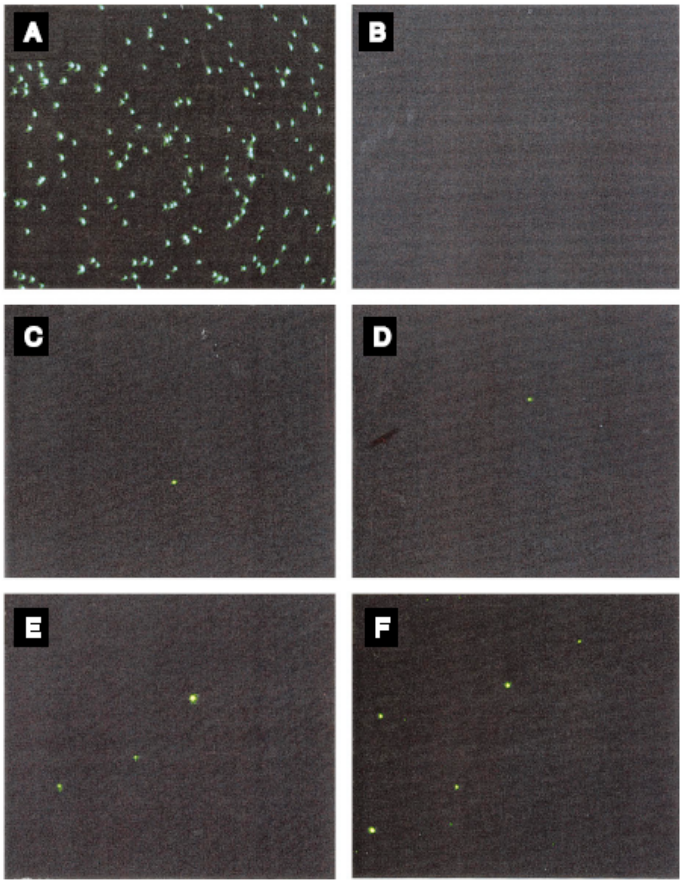

Fig. 1. Single Ag nanoparticles imaged with evanescent-wave excitation. Total internal reflection of the laser beam at the glass-liquid interface was used to reduce the laser scattering background. The instrument setup for evanescent-wave microscopy was adapted from Funatsu *et al.* (*11*). The images were directly recorded on color photographic film (ASA-1600) with a 30-s exposure by a Nikon 35-mm camera attached to the microscope. (**A**) Unfiltered photograph showing scattered laser light from all particles immobilized on a polylysine-coated surface. (**B**) Filtered photographs taken from a blank Ag colloid sample (incubated with 1 mM NaCl and no R6G analyte molecules). (**C**) and (**D**) Filtered photographs taken from a Ag colloid sample incubated with 2×10^{-11} M R6G. These images were selected to show at least one Raman scattering particle. Different areas of the cover slip were rapidly screened, and most fields of view did not contain visible particles. (**E**) Filtered photograph taken from Ag colloid incubated with 2×10^{-10} M R6G. (**F**) Filtered photograph taken from Ag colloid incubated with 2×10^{-9} M R6G. A high-performance bandpass filter was used to remove the scattered laser light and to pass Stokes-shifted Raman signals from 540 to 580 nm (920 to 2200 cm^{-1}). Continuous-wave excitation at 514.5 nm was provided by an Ar ion laser. The total laser power at the sample was 10 mW. Note the color differences between the scattered laser light in (A) and the red-shifted light in (C) through (F).

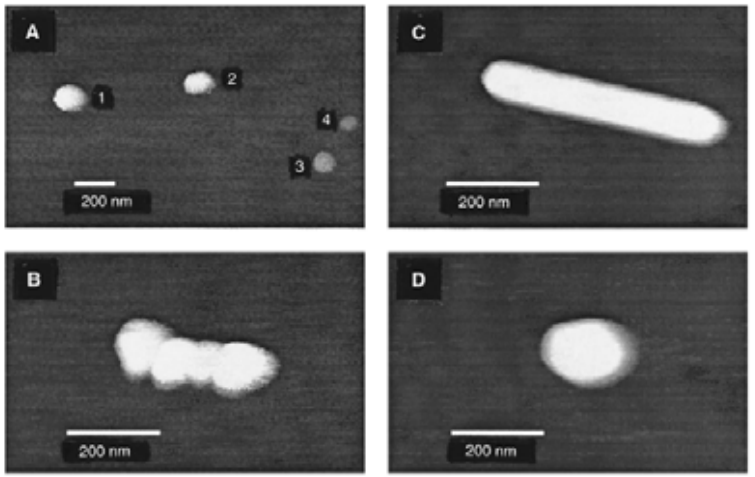

Fig. 2. Tapping-mode AFM images of screened Ag nanoparticles. (**A**) Large area survey image showing four single nanoparticles. Particles 1 and 2 were highly efficient for Raman enhancement, but particles 3 and 4 (smaller in size) were not. (**B**) Close-up image of a hot aggregate containing four linearly arranged particles. (**C**) Close-up image of a rod-shaped hot particle. (**D**) Close-up image of a faceted hot particle.

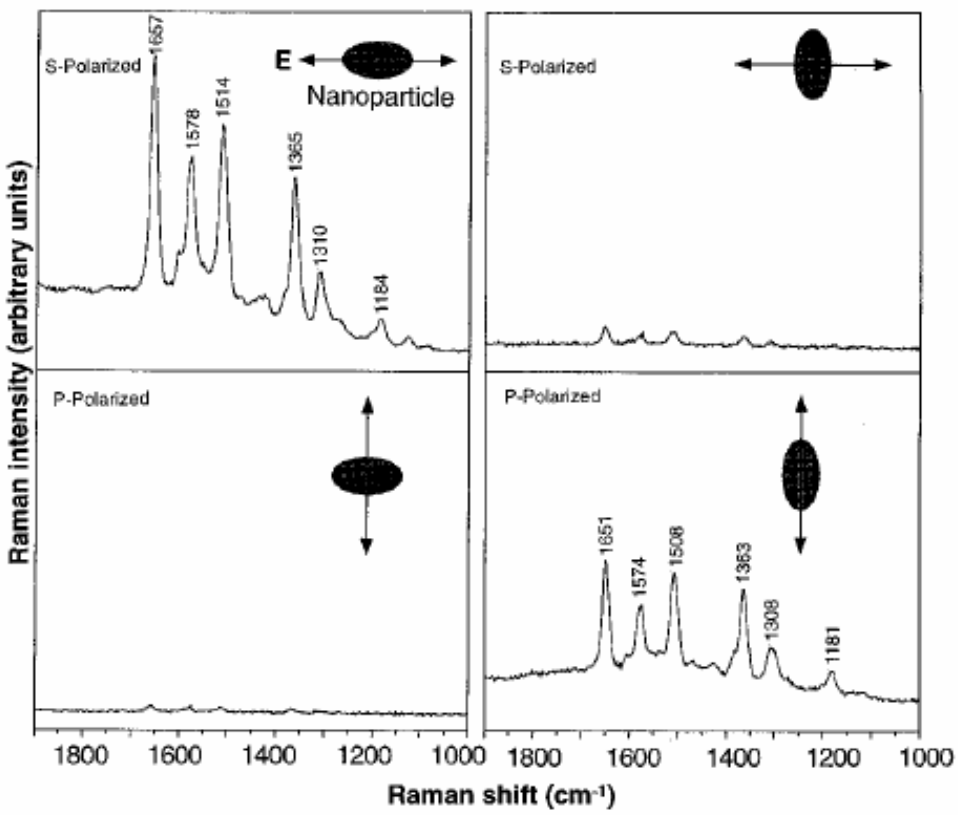

Fig. 3. Surface-enhanced Raman spectra of R6G obtained with a linearly polarized confocal laser beam from two Ag nanoparticles. The R6G concentration was 2×10^{-11} M, corresponding to an average of 0.1 analyte molecule per particle. The direction of laser polarization and the expected particle orientation are shown schematically for each spectrum. Laser wavelength, 514.5 nm; laser power, 250 nW; laser focal radius, ~250 nm; integration time, 30 s. All spectra were plotted on the same intensity scale in arbitrary units of the CCD detector readout signal.

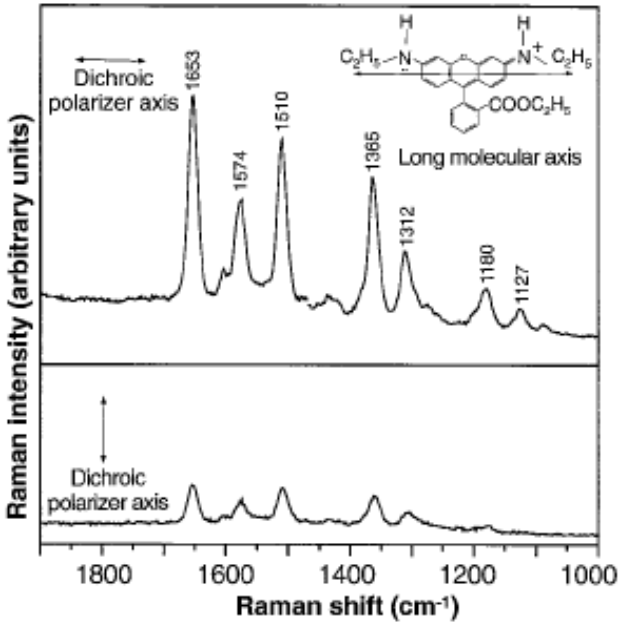

Fig. 4. Emission-polarized surface-enhanced Raman signals of R6G observed from a single Ag nanoparticle with a polarization-scrambled confocal laser beam. A dichroic sheet polarizer was rotated 90° to select Raman scattering signals polarized parallel (upper spectrum) or perpendicular (lower spectrum) to the long molecular axis of R6G. (**Inserts**) Structure of R6G, the electronic transition dipole (along the long axis when excited at 514.5 nm), and the dichroic polarizer orientations. Other conditions as in Fig. 3.

troscopic signatures of adsorbed molecules. For single rhodamine 6G molecules adsorbed on the selected nanoparticles, the intrinsic Raman enhancement factors were on the order of 10^{14} to 10^{15}, much larger than the ensemble-averaged values derived from conventional measurements. This enormous enhancement leads to vibrational Raman signals that are more intense and more stable than single-molecule fluorescence.

Electromagnetic contributions to single-molecule sensitivity in surface-enhanced Raman scattering

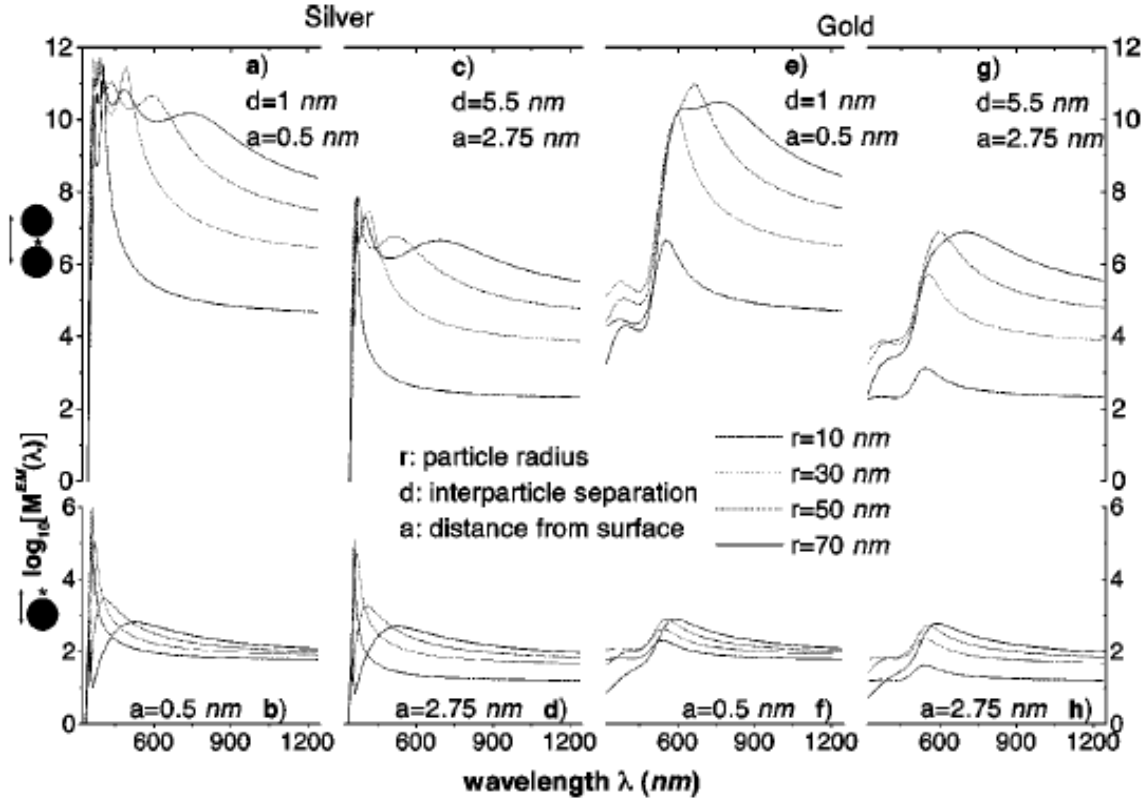

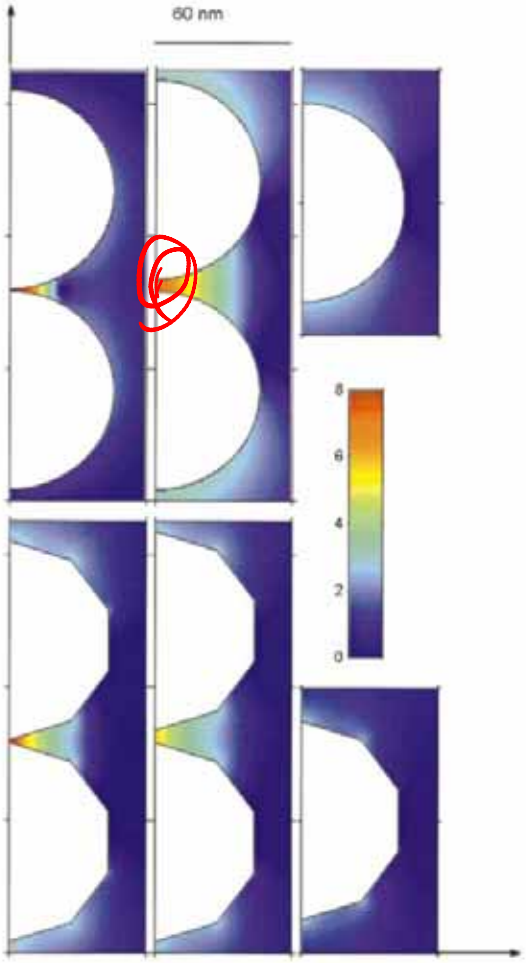

FIG. 3. (Color) EM-enhancement factor M^{EM} at a cross section through six different silver particle configurations. The wavelength of the incident field is $\lambda = 514.5$ nm with vertical polarization. The left-hand column illustrates the EM enhancement for dimer configurations of two spheres (top) and two polygons (bottom) with a separation of 1 nm. The middle column shows the same situation, but with a separation distance of 5.5 nm. The right-hand column shows the case of an isolated single particle. All particles share a common largest dimension of 90 nm. Note that the color scale from dark blue to dark red is logarithmic, covering the interval $10^0 < M^{EM} < 10^8$. Regions with enhancement outside this interval are shown in dark blue and dark red, respectively.

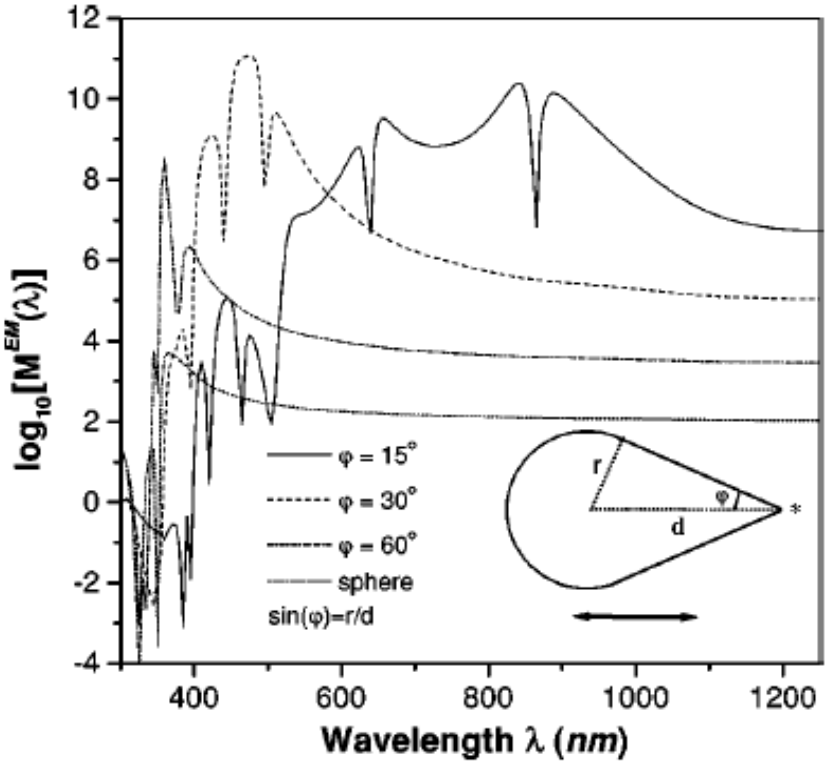

FIG. 5. EM-enhancement factor for a rotationally symmetric silver droplet as a function of the angle defining the opening edge ϕ. The field is polarized parallel to the axis of the droplet and the evaluation position (star) is located 0.5 nm outside the tip. As the droplet becomes sharper the enhancement increases several orders of magnitude.

Nanosphere Arrays with Controlled Sub-10-nm Gaps as Surface-Enhanced Raman Spectroscopy Substrates

J. AM. CHEM. SOC. 2005, *127*, 14992−14993

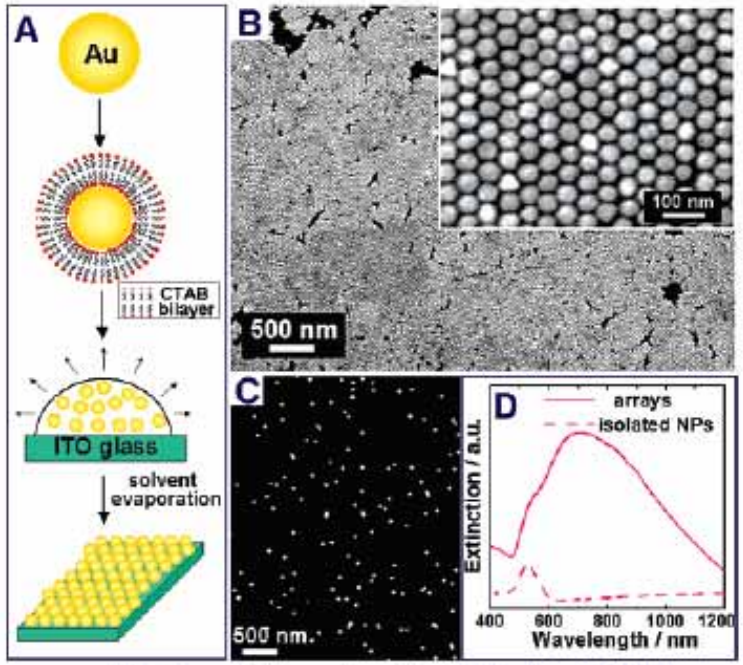

Figure 1. (A) Schematic illustration of the fabrication of sub-10-nm gap Au NP arrays. (B) SEM image of the arrays. (C) SEM image of monolayer of isolated Au NPs on ITO glass. (D) Vis−NIR extinction spectrum of the monolayer of isolated Au NPs and arrays.

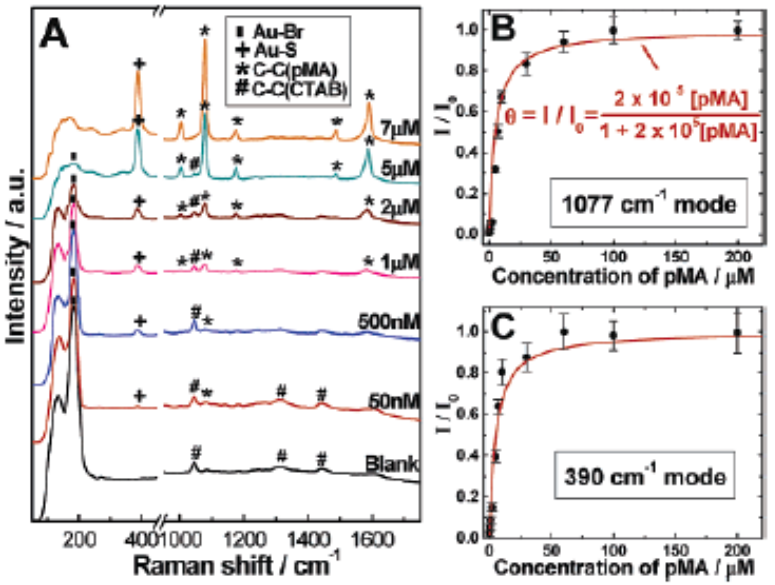

Figure 2. (A) SERS spectra of 5 μL of pMA with different concentrations deposited on the NP arrays. The excitation laser wavelength is 785 nm. Adsorption isotherm of pMA on the NP arrays obtained according to (B) 1077 and (C) 390 cm^{-1} modes in the SERS spectra. I_0 is the peak intensity of a saturated pMA monolayer.

Profiling the Near Field of a Plasmonic Nanoparticle with Raman-Based Molecular Rulers

NANO LETTERS

2006
Vol. 6, No. 10
2338−2343

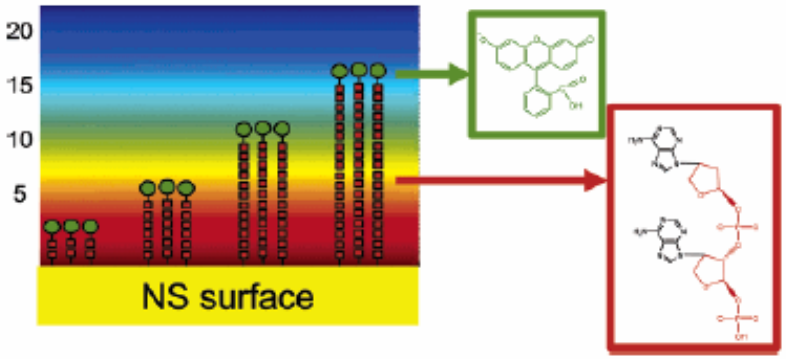

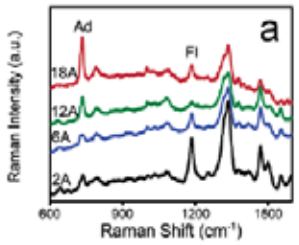

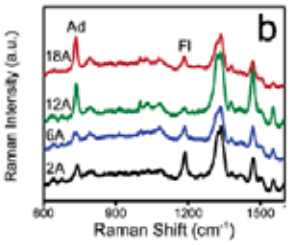

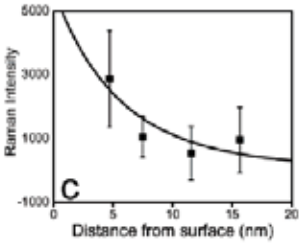

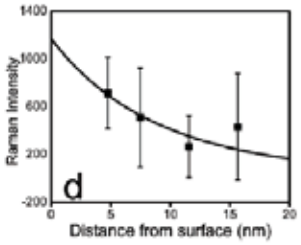

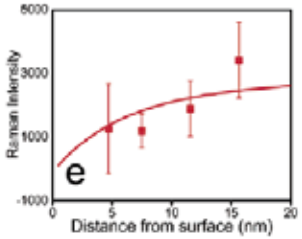

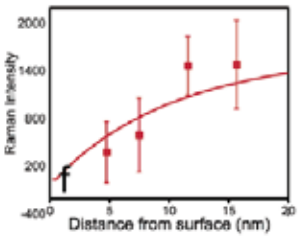

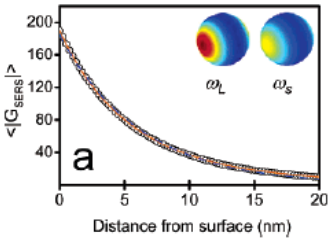

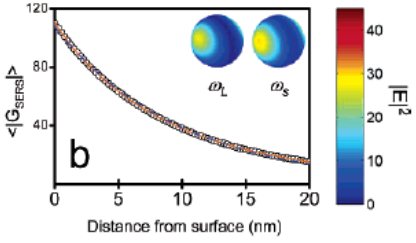

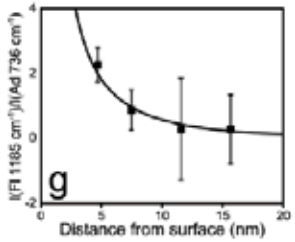

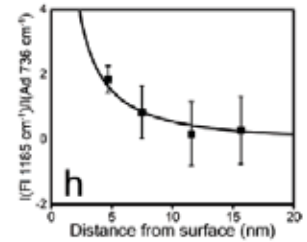

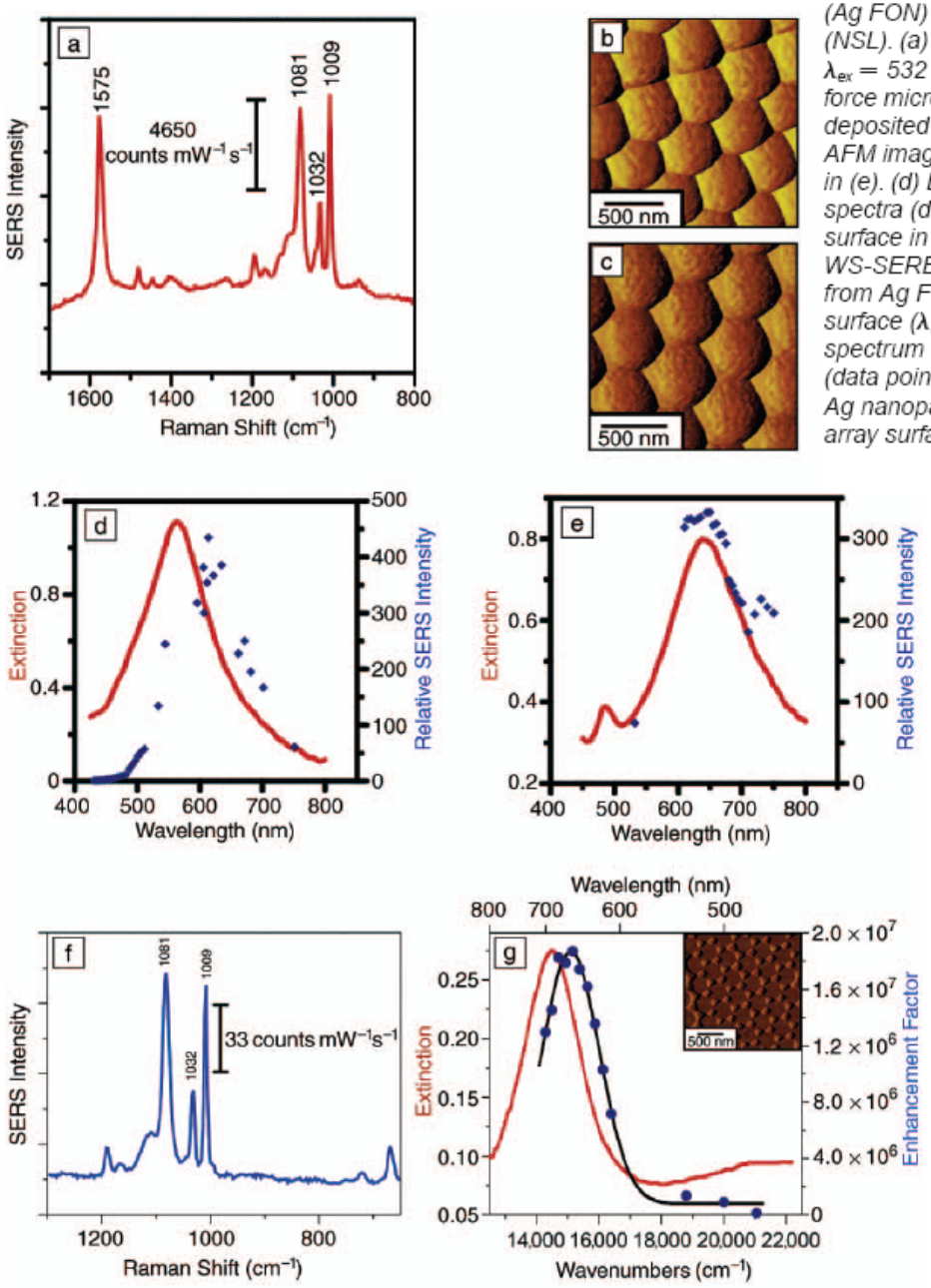

Figure 6. Localized surface plasmon resonance (LSPR), surface-enhanced Raman spectroscopy (SERS), and wavelength-scanned surface-enhanced Raman excitation spectroscopy (WS-SERES) results for benzenethiol adsorbed on Ag film-over-nanosphere (Ag FON) surfaces and nanoparticle arrays fabricated by nanosphere lithography (NSL). (a) SERS spectrum measured from Ag FON surface with excitation wavelength λ_{ex} = 532 nm, power = 3.0 mW, and 100 s data acquisition time. (b) Contact-mode atomic force microscopy (AFM) image of Ag FON surface (nanosphere diameter D = 410 nm, deposited mass thickness d_m = 200 nm) used for SERS in (a). (c) Contact-mode AFM image of Ag FON surface (D = 500 nm, d_m = 250 nm) used for WS-SERES in (e). (d) LSPR spectrum (solid line, λ_{max} = 562 nm, FWHM = 144 nm) and WS-SERES spectra (data points) for the 1081 cm^{-1} band of benzenethiol measured from the Ag FON surface in (b). (e) LSPR spectrum (solid line, λ_{max} = 638 nm, FWHM = 131 nm) and WS-SERES spectra (data points) for the 1081 cm^{-1} band of benzenethiol measured from Ag FON surface in (c). (f) SERS spectrum measured from Ag nanoparticle array surface (λ_{ex} = 532 nm, power = 3.0 mW, 100 s data acquisition time). (g) LSPR spectrum (solid line, λ_{max} = 688 nm, FWHM = 95 nm) and WS-SERES spectra (data points) for the 1081 cm^{-1} band of benzenethiol measured from a Ag nanoparticle array surface. (inset) Tapping-mode AFM image of a representative array surface.

Confocal Raman Image

Sample: 460 nm polystyrene on silicon substrate
Image scan without EM gain

Raman spectrum

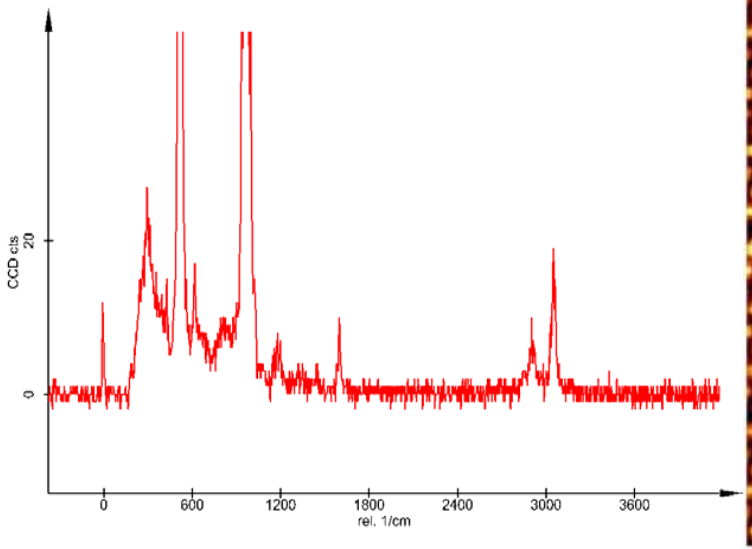

Raman image

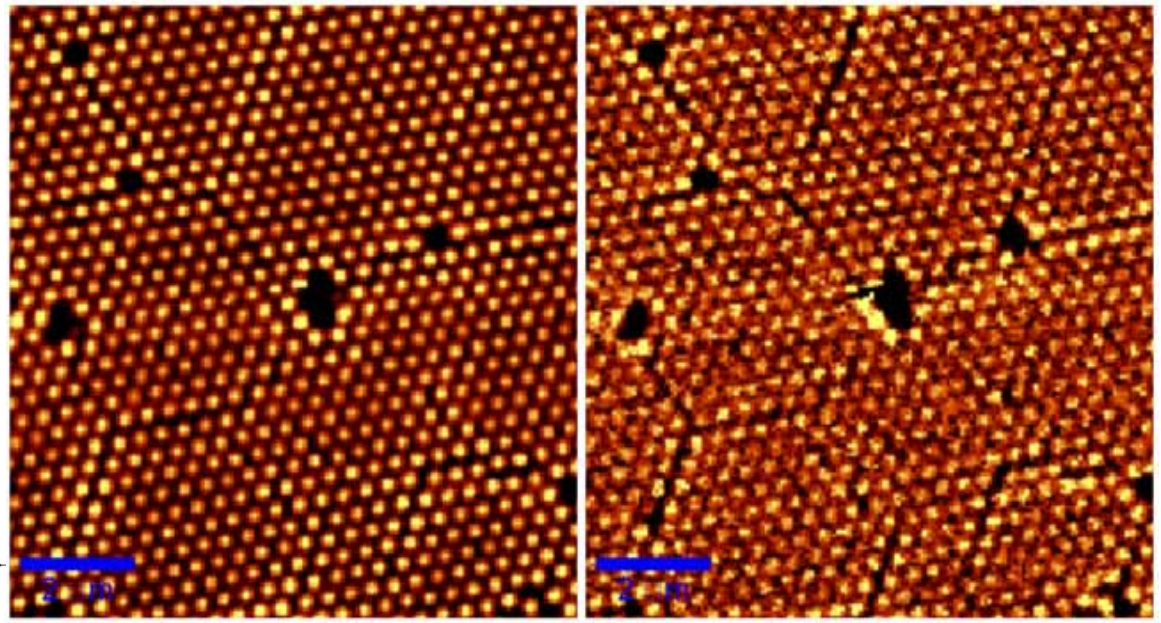

Wavelength filter :
478.33032 ~ 562.13727 cm^{-1}

Wavelength filter :
3011.8789 ~ 3089.2393 cm^{-1}

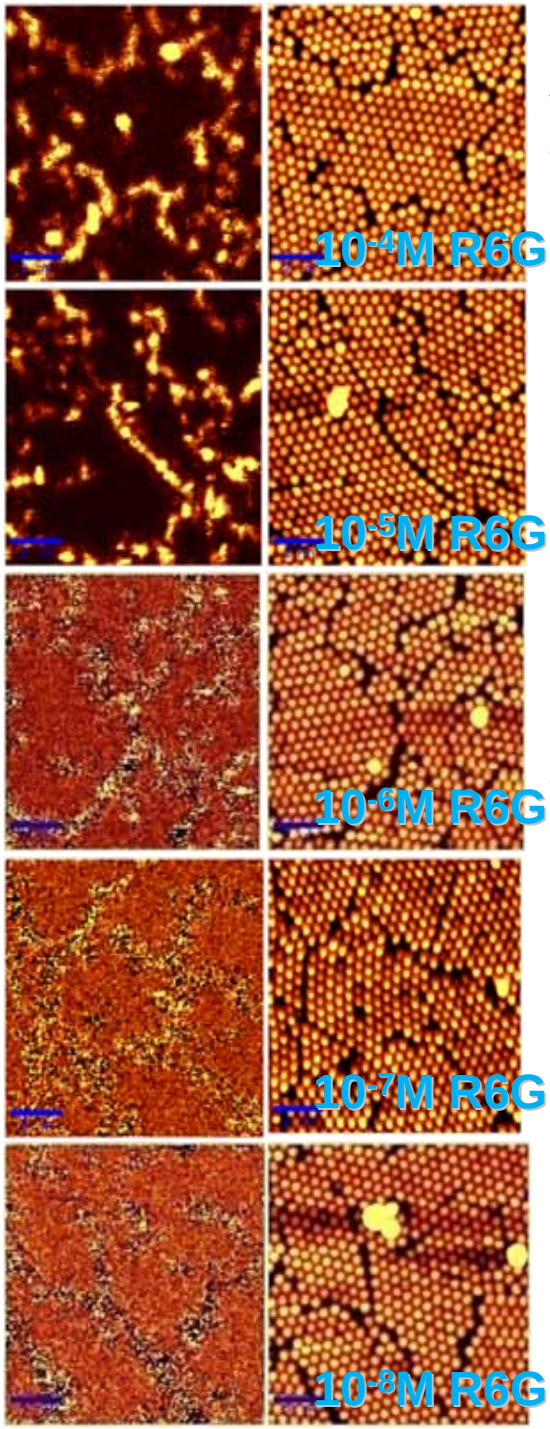

Blue line: 10^{-4} M R6G molecules
Red line: 10^{-5} M R6G molecules
Yellow line: 10^{-6} M R6G molecules
Green line: 10^{-7} M R6G molecules
Black line: 10^{-8} M R6G molecules

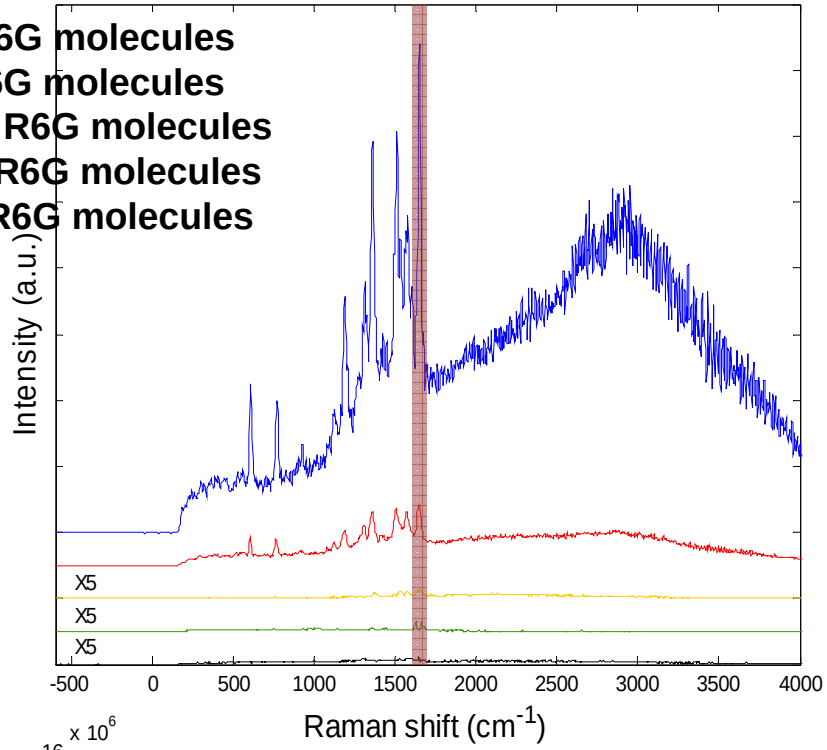

50% I_{Max}
1648 cm^{-1} Raman peak

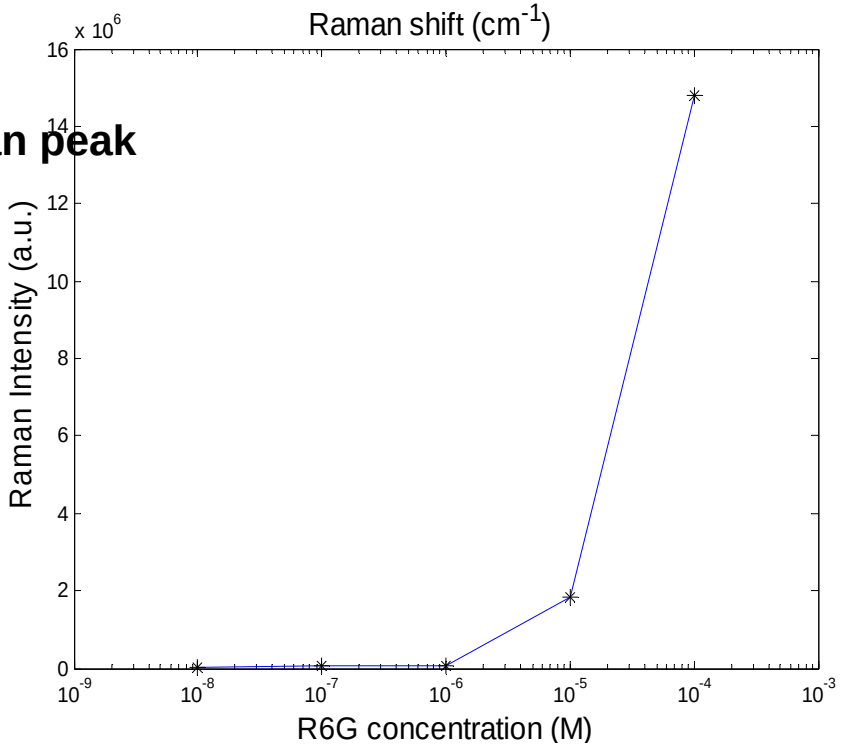

Distribution of SERS active Area

Raman peak : 1648 cm^{-1}

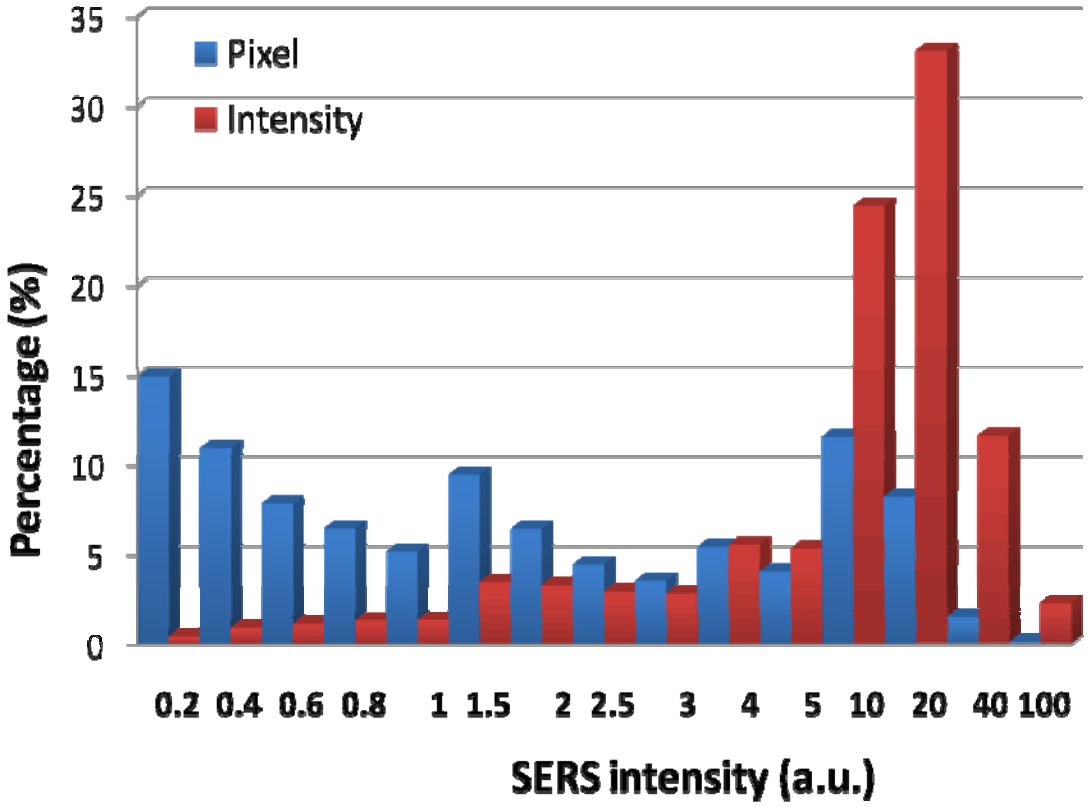

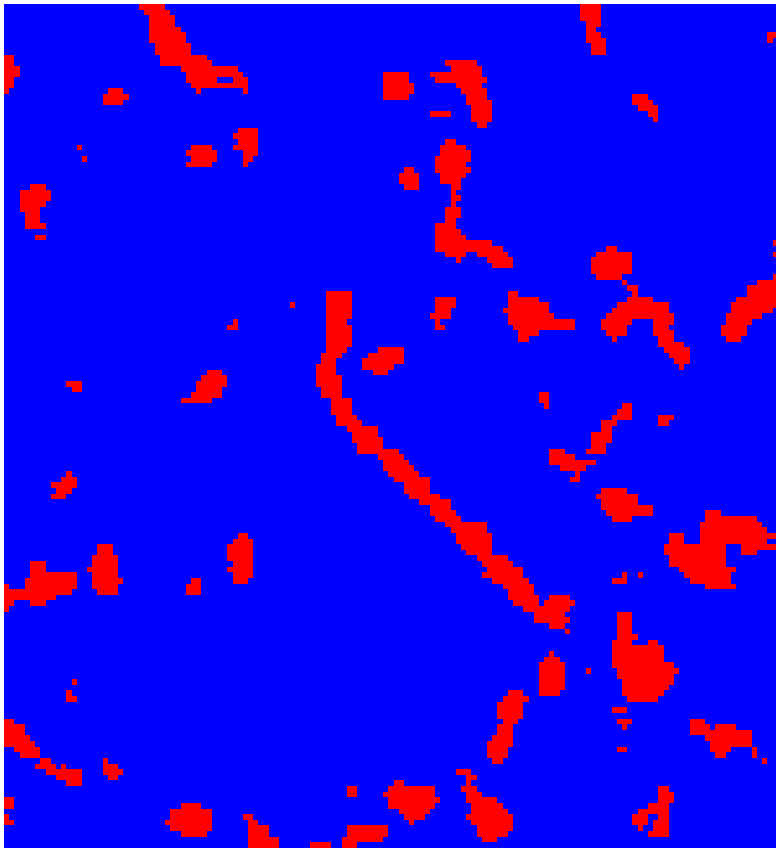

≧10% I_{Max} => 9.90% pixel => 46.97% intensity

＜ 1% I_{Max} => 45.28% pixel => 5.20% intensity

Blue area : 0~10% enhancement

Red area : 10~100% enhancement

The Enhancement of SERS Active Substrate

Excitation laser : Ar^+ laser (488 nm)

Rhodamine 6G

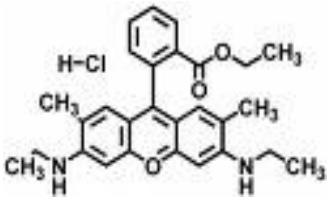

Red line: R6G on silicon substrate with 460 nm PS covered by 200 nm silver film.

Blue line: R6G on silicon substrate coating with 200 nm silver film.

Black line: R6G on silicon

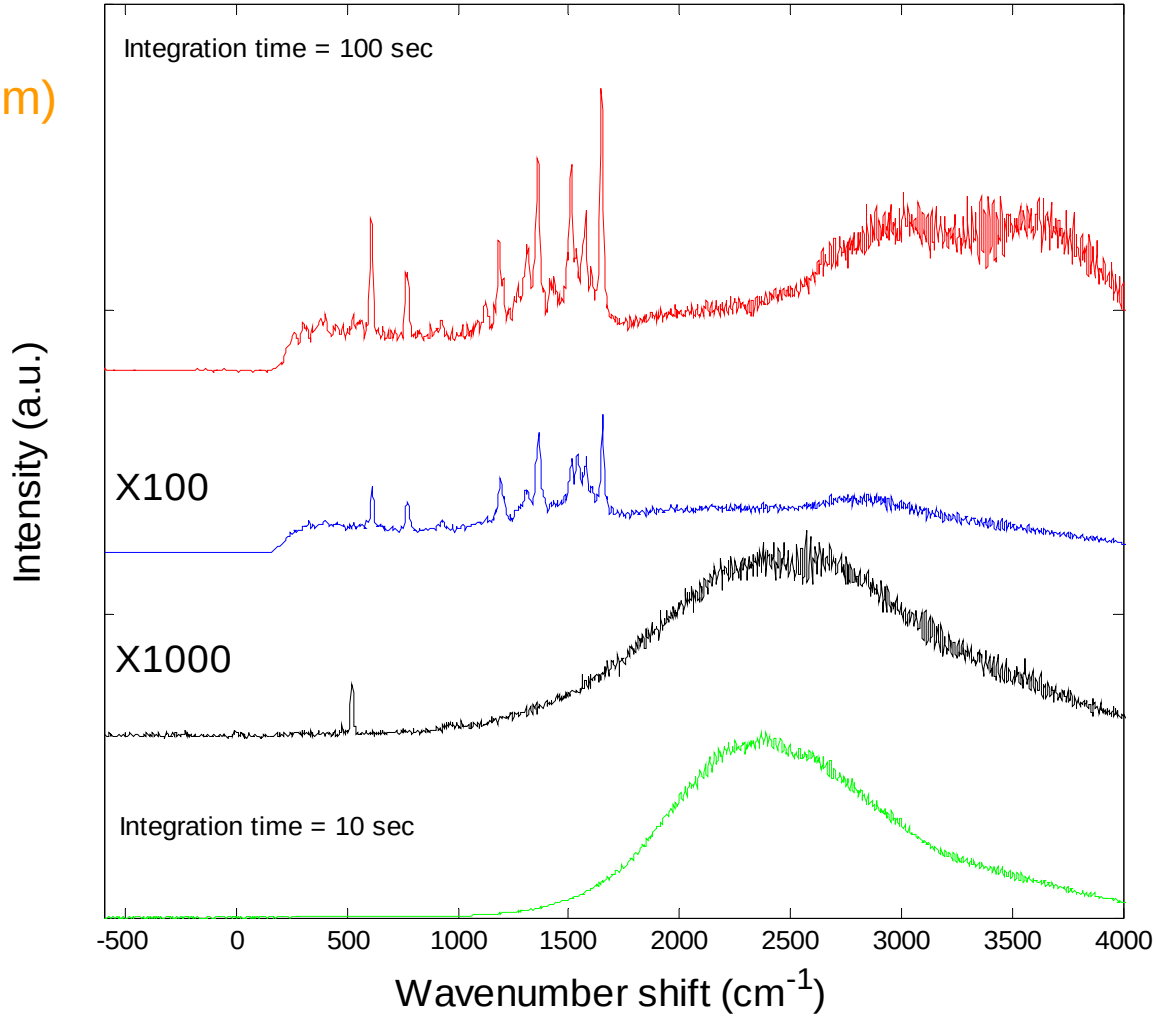

R6G solution

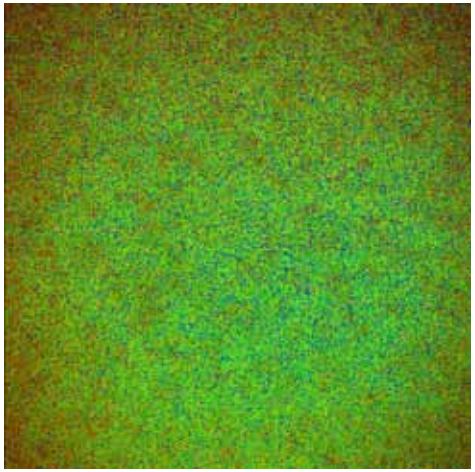

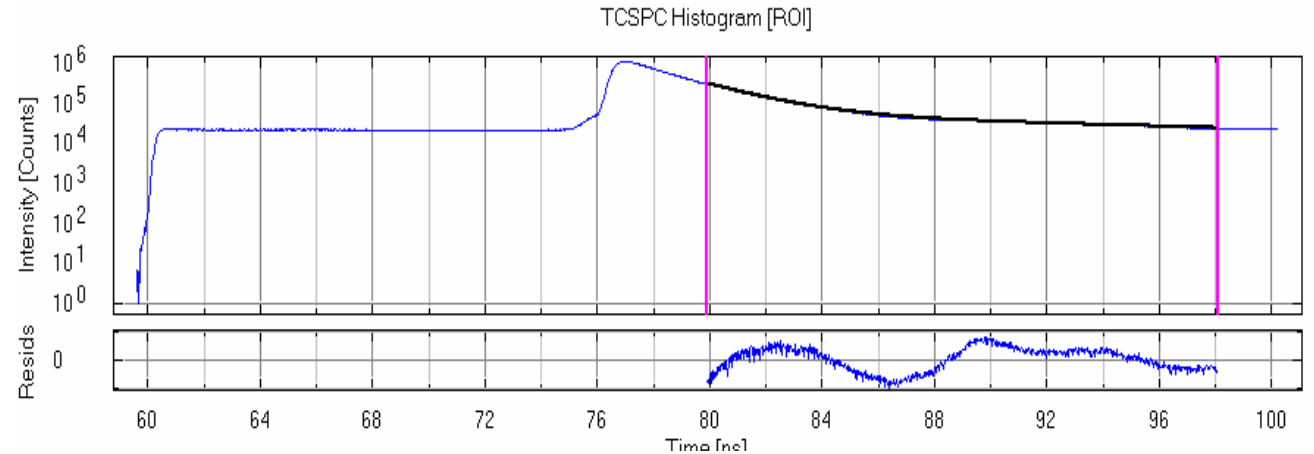

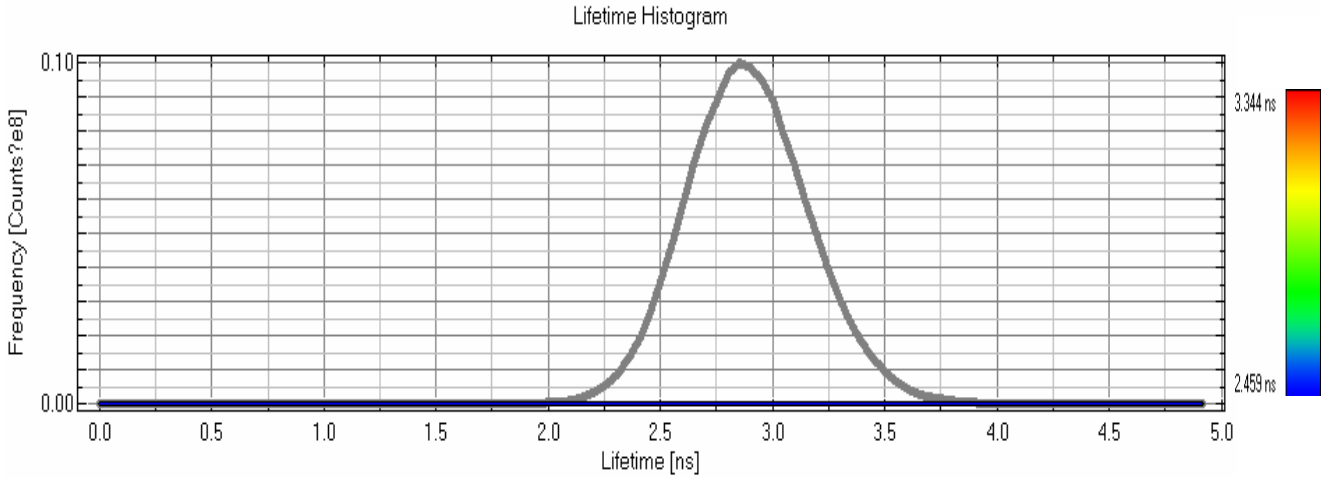

10^{-4} M R6G on 460 nm PS with 200 nm Ag film coating

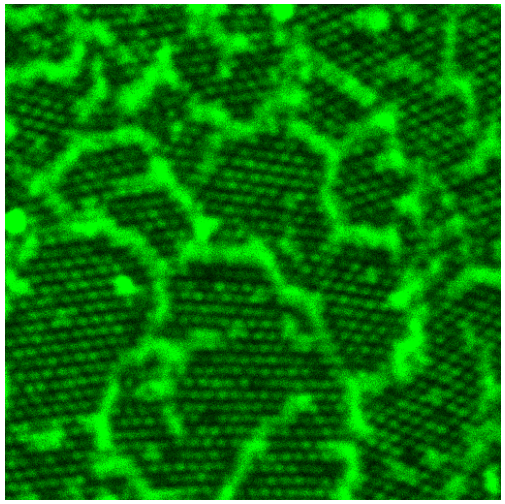

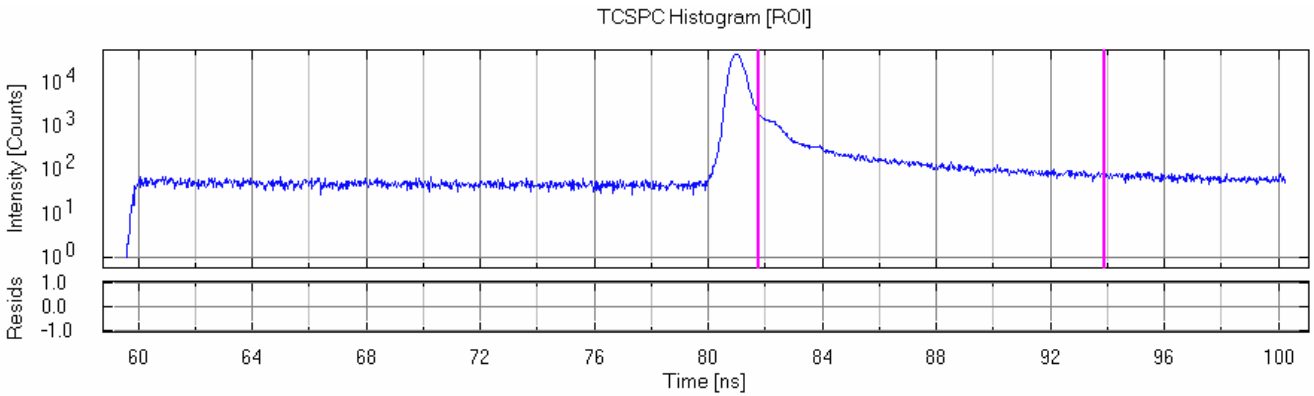

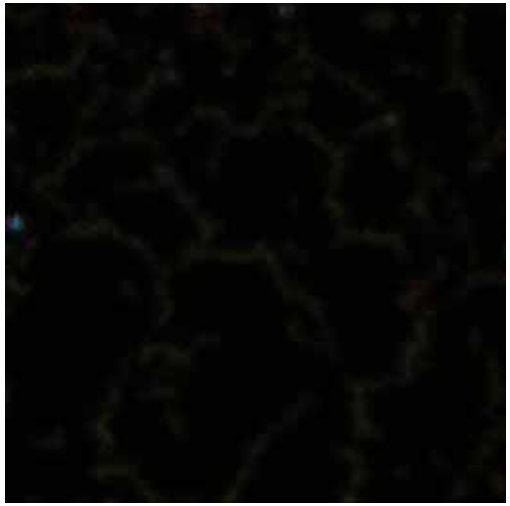

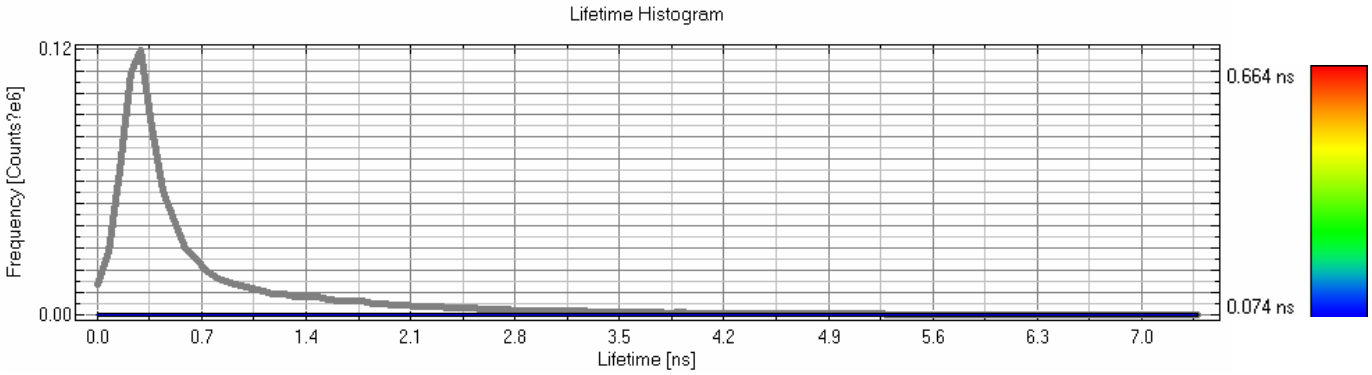

Tip Enhanced Raman

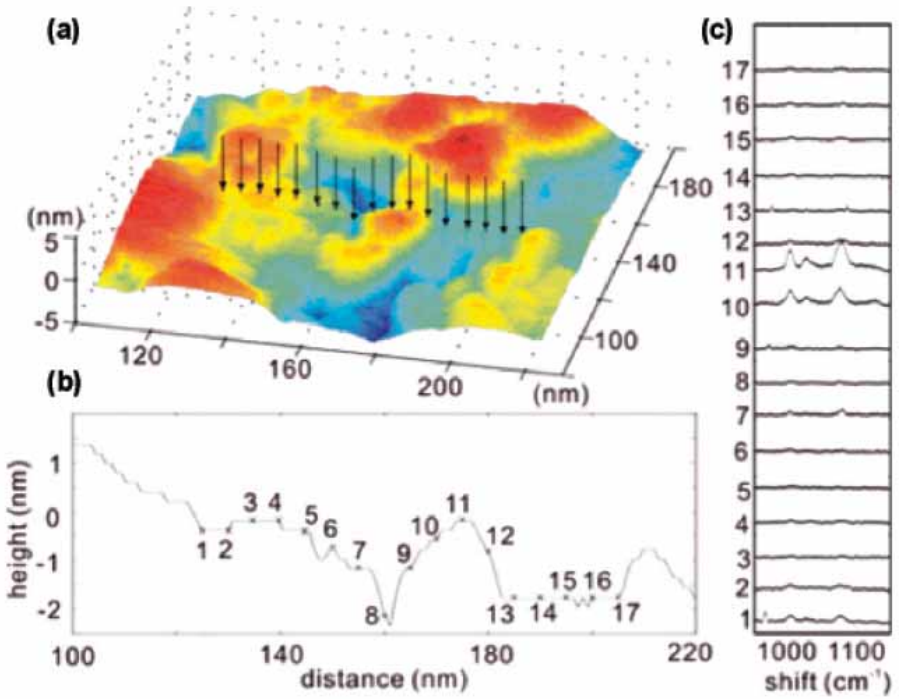

Figure 24. TERS mapping on a rough Au surface. An STM image of the sample is shown in a. TERS data was collected at the positions indicated by the arrows. The cross section of the topography image is shown in b, and the TERS collection sites are labeled with crosses. (c) Corresponding TERS sequence. The numbers denote the sites where the spectra were collected. Reprinted with permission from ref 463. Copyright 2007 American Chemical Society.

Near-Field Raman Microscopy

Droplet of AG nano particles labelled with Rodamine 6G on cover glass

Experiment Parameters:

Excitation Laser:	532 nm
Scan Range:	4 µm x 4 µm
Resolution:	100 x 100 pixel
Integration Time:	110 ms per spectrum
Feedback:	SNOM AC Mode

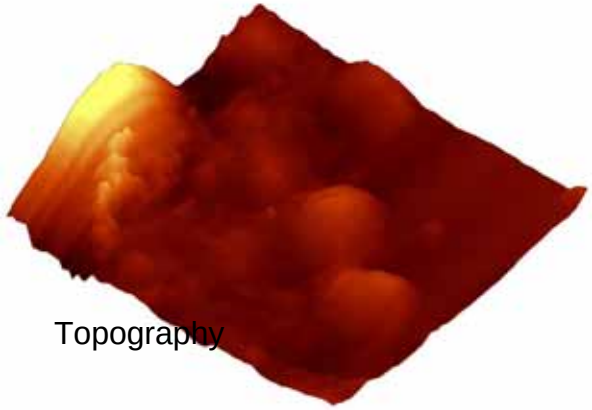

Topography

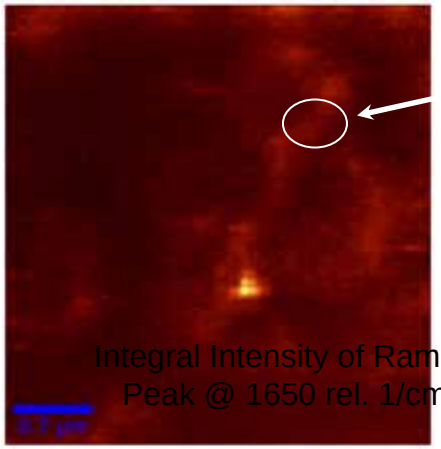

Integral Intensity of Raman Peak @ 1650 rel. 1/cm

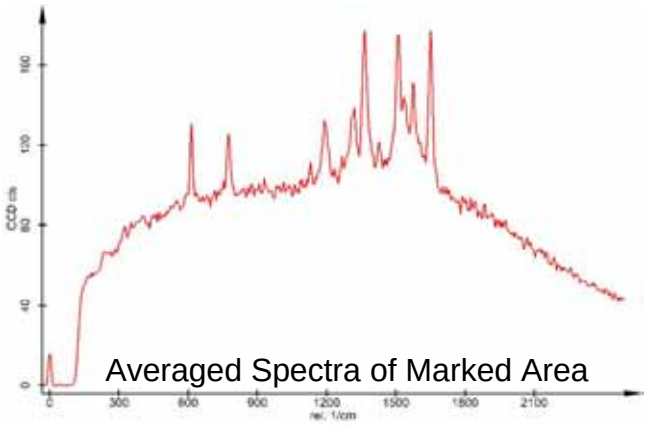

Averaged Spectra of Marked Area

Periodic Hole Array

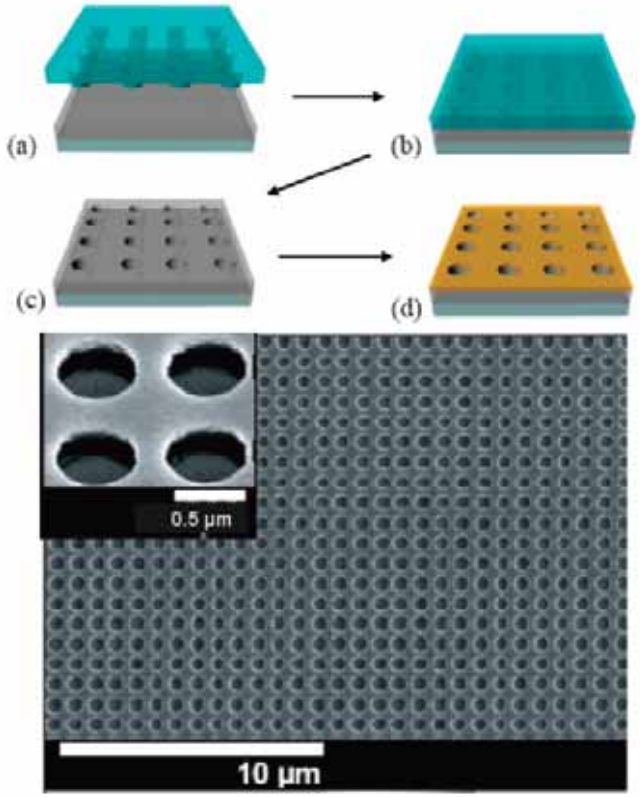

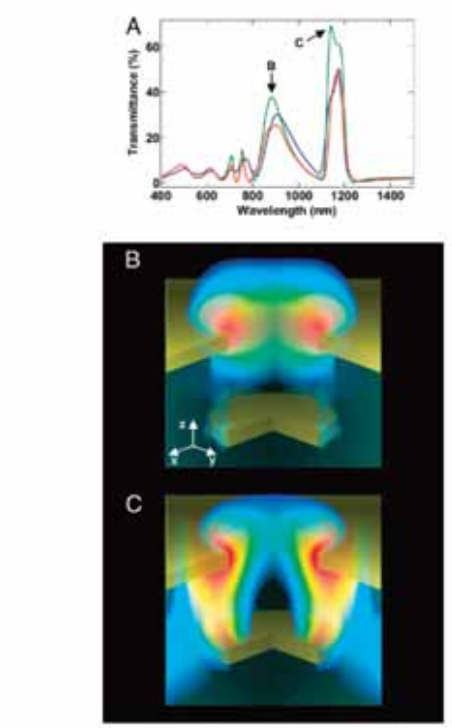

Figure 17. Correlation of transmission spectral features with hole/disk plasmonic excitations. (a) Normal incidence transmission spectrum of a quasi-3D plasmonic crystal (blue), and rigorous electrodynamics modeling of the spectrum for an ideal crystal (green) and one that includes subtle isolated nanoscale grains of Au near the edges of the Au disks (red). (b) Computed electromagnetic field distribution associated with the resonance at 883 nm (labeled B in a). The intensity is concentrated at the edges of the nanoholes in the upper level of the crystal. (c) Field distribution associated with the resonance at 1138 nm (labeled C in a), showing strong coupling between the upper and lower levels of the crystal. Reprinted with permission from ref 77. Copyright 2006 The National Academy of Sciences of the USA.

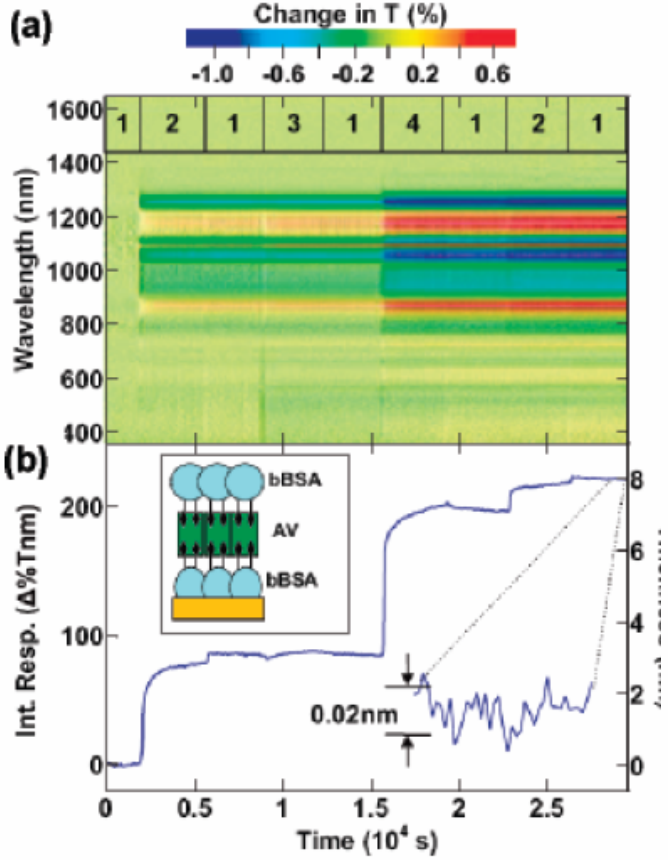
(a)
Change in T (%)
-1.0 -0.6 -0.2 0.2 0.6
1 2 1 3 1 4 1 2 1
Wavelength (nm)
(b)
bBSA
AV
bBSA
0.02nm
Int. Resp. (Δ%Tnm)
Time (10⁴ s)

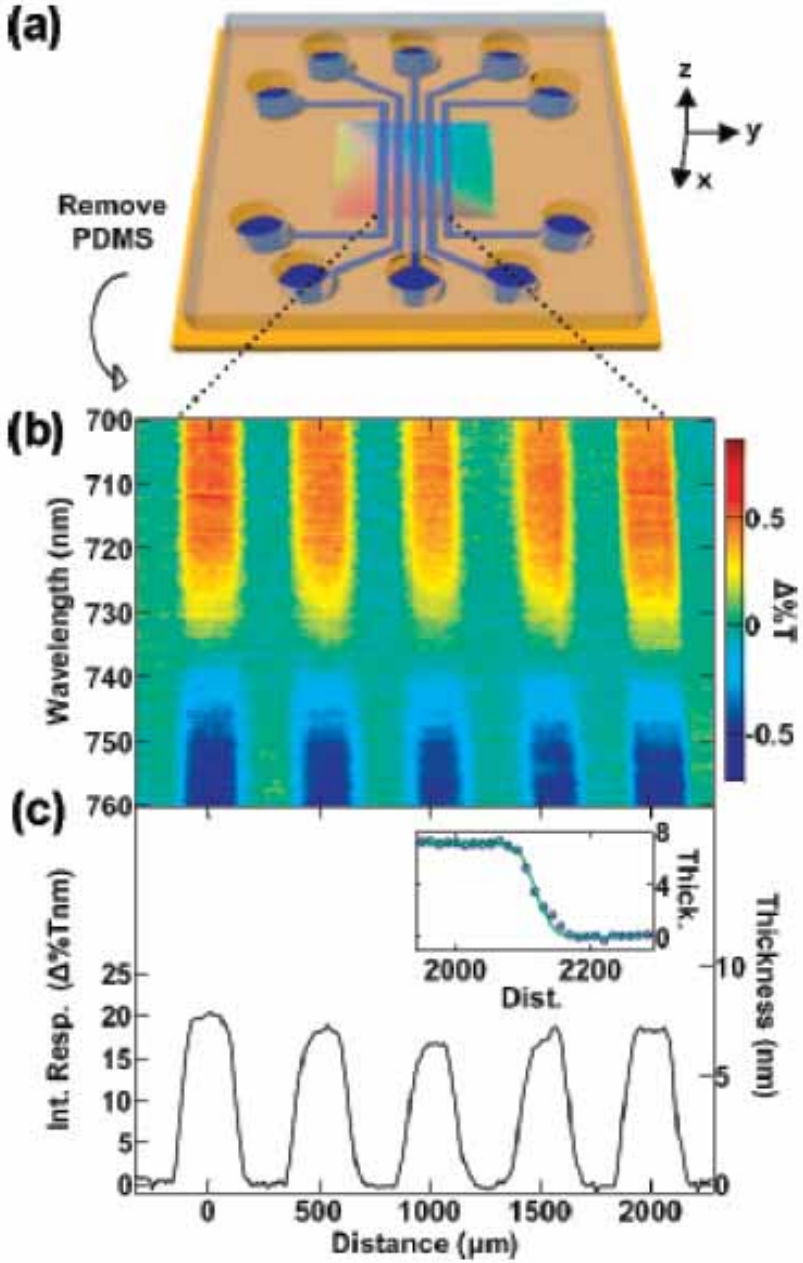
(a)
Remove PDMS
z
y
x
(b)
Wavelength (nm)
Δ%T
(c)
Int. Resp. (Δ%Tnm)
Thick.
Dist.
Thickness (nm)
Distance (μm)